JOHNSON-COOK FAILURE PARAMETERS

CALIBRATION OF THE JOHNSON-COOK FAILURE PARAMETERS AS THE CHIP SEPARATION CRITERION IN THE MODELLING OF THE ORTHOGONAL METAL CUTTING PROCESS

By KEYAN WANG, B. ENG.

A Thesis Submitted to the School of Graduate Studies in Partial Fulfilment of Requirements for the Degree Master's of Applied Science

McMaster University

MASTER'S OF APPLIED SCIENCE (2016) McMaster University

(Mechanical Engineering) Hamilton Ontario

TITLE: Calibration of the Johnson-Cook Failure Parameters as the Chip Separation Criterion in the Modelling of the Orthogonal Metal Cutting Process

AUTHOR: Keyan Wang, B. Eng. (McMaster University)

SUPERVISORS: Dr. Eu-Gene Ng

NUMBER OF PAGES: xx,103

ABSTRACT

The finite element analysis (FEA) is a numerical method widely used to predict the metal-cutting performance in both academic and industrial studies, avoiding the high expense and time consumption of experimental methods. The problem is how to calibrate reliable fracture-parameters as chip-separation criterion are implemented into FEA modelling. This thesis introduces a calibration method of the Johnson-Cook fracture parameters used in the orthogonal metal cutting modelling with a positive rake angle for AISI 1045 steel. These fracture parameters were obtained based on a set of quasi-static tensile tests, with smooth and pre-notched round bars at room temperature and elevated temperatures. The fracture parameters were validated by low- and high-strain rate simulations corresponding to tensile tests and orthogonal metal-cutting processes respectively in ABAQUS/Explicit. Compared to literature calibration methods, this method is simpler, less expensive but valid.

ACKNOWLEDGMENTS

I cannot express enough thanks to all of those who continued support and encourage me to complete this thesis.

I would like to express my sincere gratitude to my supervisor Dr. Eu-Gene Ng for his patience, motivation, and immense knowledge. Without his guidance and support, I could not have imagined a better study for the researching and writing of this thesis. Most importantly, I deeply appreciate this opportunity given to me by Dr. Eu-Gene Ng to complete this important research.

I would like to thank the Department of Mechanical Engineering, McMaster University, for financing and sponsoring this research.

I would like to thank Dr. Micheal Bruhis for his excellent help and guidance during the tensile tests.

I would like to thank Mr. Doug Culley for his help and guidance for the metal heat-treatment and the measurement of metallography.

I would like to thank the members in my research group and my friends: Youssef Ziada, Keyvan Hosseinkhani, Amy Short, Wanlin Zhang, Chenhui Niu and Si Sun for their help with research discussions and the experimental work.

Finally, I would like to thank my parents and my friends for their encouragement, patience and support during the whole of this research process.

TABLE OF CONTENTS

LIST OF FIGURES

LIST OF TABLE CAPTIONS

NOMENCLATURE AND LIST OF SYMBOLS

2D : Two dimensional
3D : Three dimensional
a : Radius of the center cross section of the tensile specimen (mm)
A_0 : Original central cross section of the tensile specimen
A_{ave} : Average Johnson-Cook material constant adjusted with λ value (MPa)
A_f : Area of the center cross section of the tensile specimen after fracture (mm^2)
AISI : American Iron and Steel Institute
ALE : Arbitrary Lagrangian Eulerian
A_{true} : Actural Johnson-Cook material constant adjusted with κ value (MPa)
b : (When described the notched tensile specimen as shown in Figure 3.1) Half of the chord length of the notch of the tensile specimen (mm)
B_{ave} : Average Johnson-Cook material constant adjusted with λ value (MPa)
B_{true} : Actural Johnson-Cook material constant adjusted with κ value (MPa)
C_1 : (When used in the function of stress triaxiality and strain to fracture) Material constant (-)
C_2 : (When used in the function of stress triaxiality and strain to fracture) Material constant (-)
CCD : Charged-coupled device
c_p : Specific heat capacity (J/kg·°C)
d : (When used in Figure 4.3) overall damage variable (-)
D : Accumulated damage (-)
d : Diameter of the minimum cross section of the tensile specimen (mm)
d_0 : Initial diameter of the center cross section of the tensile specimen (mm)
D_1 : (When used in Johnson-Cook fracture equation) Fracture parameter (-)
D_2 : (When used in Johnson-Cook fracture equation) Fracture parameter (-)
D_3 : (When used in Johnson-Cook fracture equation) Fracture parameter (-)
D_4 : (When used in Johnson-Cook fracture equation) Fracture parameter (-)
D_5 : (When used in Johnson-Cook fracture equation) Fracture parameter (-)
D_{cr} : Critical accumulated damage (-)
d_f : Diameter of the center cross section of the tensile specimen after fracture (mm)
DIC : Digital image correlation
E : Errors of the cutting force between the cutting experimental result and FEM (in Figure 5.25)
E : Young’s Modulus (MPa)
FEA : Finite element analysis
FEM : Finite element method

h : (When described the notched tensile specimen as shown in Figure 3.1) arrow height of the notch of the tensile specimen (mm)
$[I]$: (When used in the deviatoric stress tensor equation) Identity tensor (MPa)
k : Thermal Conductivity (W/(m·˚C))
K_T : Thermal softening fraction (-)
L : Characteristic length (m)
n_{ave} : Average Johnson-Cook material constant adjusted with λ value (-)
No. : Number (-)
n_{true} : Actural Johnson-Cook material constant adjusted with κ value (-)
OFHC : Oxygen-free high thermal conductivity
p : Hydrostatic pressure (MPa)
r : (When used in Equation (5.20)) chip thickness ratio (-)
R : Radius of the curvature of the profile of the notch of the tensile specimen (mm)
R_0 : Initial radius of the curvature of the profile of the notch of the tensile specimen (mm)
RA_e : Reduction areas from the tension tests (-)
RA_m : Reduction areas from the modelling (-)
R_f : Radius of the curvature of the profile of the notch of the tensile specimen after fracture (mm)
$[S]$: deviatoric stress tensor (MPa)
T^* : homologous temperature (-)
Tc : Chip thickness after separation (mm)
t_{c_m} : Measured chip thickness (mm)
t_{c_t} : Theoretical chip thickness (mm)
T_melt : Melting temperature (℃)
t_o : Thickness of the chip prior to chip formation. (mm)
T_room : Room temperature (℃)
T_tf : Transition temperature for failure (℃)
T_γ : Discrete value of the temperature (℃)
T_γ^* : Discrete value of the homologous temperature (-)
t_u : Uncut chip thickness (mm)
u : Displacement space (m)
$\bar{u}_f^{pl}$: Equivalent plastic displacement at fracture (m)
$\bar{u}^{pl}$: Equivalent plastic displacement (m)
wt% : Weight percentage (-)
α : Rake angle of the tool (°)
α : Thermal expansion (˚$\mathrm{C}^{-1}\times10^6$)
α : (When used in the function of stress triaxiality and strain to fracture)

Material constant (-)

$\Delta\varepsilon$: Increment of the equivalent plastic strain (-)

ε : (When used in the Johnson-Cook constrictive model) equivalent plastic strain (-)

ε^f : Equivalent strain to fracture (-)

$\varepsilon_{fs}^{\exp}$: True fracture strain measured from a smooth specimen test (-)

$\bar{\varepsilon}_n$: Void nucleation strain (-)

$\dot{\varepsilon}^*$: (When used in the Johnson-Cook constrictive model) dimensionless plastic strain rate (-)

$\bar{\varepsilon}_f$: (When used in the Johnson-Cook fracture model) equivalent strain to fracture (-)

$\dot{\varepsilon}_\delta$: Discrete value of the strain rate (s^{-1})

$\dot{\varepsilon}_\delta^*$: Discrete value of the dimensionless strain rate (-)

η : Stress triaxiality (-)

η_0 : Stress triaxiality of the original specimen (-)

η_f : Stress triaxiality of the specimen after fracture (-)

θ : Lode angle (^{o})

κ : Adjusted parameter depends on the strain rate (-)

λ : Adjusted variable (-)

ν : Poisson's ratio *(-)*

ξ : Normalized third stress invariant (MPa)

ρ : Density (kg/m^3)

σ : (When used in the Johnson-Cook constrictive model) von Mises flow stress (MPa)

σ^* : Ratio of the average of the three normal stresses to the von Mises equivalent stress (-)

σ_1 : Principal stress in the Cartesian coordinate system (MPa)

σ_2 : Principal stress in the Cartesian coordinate system (MPa)

σ_3 : Principal stress in the Cartesian coordinate system (MPa)

σ_a : Average axial stress at the smallest cross section of the tensile specimen (MPa)

σ_{effect} : Stress corrected with the Bridgman correction factor (MPa)

$\bar{\sigma}$: (When used in Figure 4.3) undamaged response stress (MPa)

$\bar{\sigma}$: (When used in the Johnson-Cook fracture model) von Mises equivalent stress (MPa)

σ_m : (When used in the Johnson-Cook fracture model) average of the three normal stresses (MPa)

σ_{y0} : Onset of the damage stress (MPa)

σ_β^* : Discrete value of the stress triaxiality (-)

$[\sigma]$: Stress tensor (MPa)
φ : Coordinate of the principal stress in the spherical coordinate system (MPa)
ϕ : Shear plane angle (°)

1. Introduction

1.1 Background

The finite element method (FEM) is a numerical approach that subdivides a continuum system to finite simpler elements, and analyzes the element properties mathematically, assuming the approximate behavior of the entire system. It is widely applied to predict metal cutting performance such as the wear of the tool and the plastic deformation of the machined work piece. Klamecki [1973] employed the FEM to model the 3-dimensional metal cutting process, but only in the initial stages of chip formation. Usui and Shirakashi [1982] and Iwata et al. [1984] first simulated the chip formation under steady state cutting by using two dimensional models. Strenkowski and Carroll [1985] studied the chip separation criteria based on updated Lagrangian modules. Moreover, Komvopoulos and Erpenbeck [1991] used a distance tolerance criterion to investigate the chip separation and formation. Lin and Lin [1992] studied the chip separation, using the argument of strain energy, and analyzed chip geometry, the residual stresses in the machined surface of the work piece, and the temperature distributions in the tool and chip and the cutting forces. Ceretti et al. [1996] simulated the chip separation of the cutting process by deleting elements which reach the critical value of accumulated damage. In general, four formulations in FEM metal-cutting simulations are Lagrangian, Eulerian, Arbitrary Lagrangian Eulerian (ALE) and Smooth Particle Hydrodynamics. Lagrangian has the advantage of more convenient modelling of the evolution of the chip formation from the incipient stage to the steady form, in which the mesh follows the material which is attached to the workpiece; meanwhile, the elements move with the material along the cutting process [Soo, 2007]. Hence, an appropriate chip separation criterion is necessary. Chip separation criteria include two groups: geometrical and physical. A typical geometrical separation criterion is the distance tolerance criterion, which is based on a predefined critical distance between the tool tip and the separation node of the workpiece [Komvopoulos, 1991]. On the other hand, physical separation criteria mean the separation of the node or element occurs based on a predefined-critical-physical-parameter from the material properties and cutting conditions, such as strain, stress or strain-energy-density. Strenkowski and Carroll [1985] used the effective plastic strain criterion, that is the node removed from the workpiece when its effective plastic strain reaches a predefined critical value, which was also used by Xie et al. [1998], Liu and Guo [2000] and Hortig and Svendsen [2007]. In addition, other physical criteria include the strain energy density criterion by Lin and Lin [1992] Usta [1999] and critical stress criterion by Huang and Black [1996], Shet and Deng [2000], Mamalis et al. [2001] and Li et al. [2002]. However, Zhang [1999] evaluated above chip separation criteria and concluded that a single threshold of separation cannot be used for different cutting conditions, which means a more feasible and comprehensive criterion needs to be organized for a reliable simulation of the cutting process.

Furthermore, several models based on accumulative damage mechanics were proposed as the onset of fracture criteria in the Lagrangian based simulation of metal cutting processes, such as the Cockroft-Latham model [Cockroft, 1968], the Wilkins model [Wilkins, 1978], and the Johnson-Cook fracture model [Johnson, 1985]. In this study, the Johnson-Cook fracture model is used. The problem of using the Johnson-Cook fracture model is how to acquire and calibrate the fracture constants for the proposed material, which is AISI 1045 steel in this study. The Johnson-Cook fracture model expressed the effects of the stress triaxiality, the strain rate, and the temperature on the strain to fracture respectively in three brackets. The fracture constants relative to different effective factors were usually calibrated separately. Firstly, to calibrate the stress triaxiality relative fracture constants D_1, D_2 and D_3, some researchers obtained the data based on quasi-static tests, such as tensile tests with smooth and notched round bars, torsion tests, or tests with specially designed specimens [Johnson, 1985], [Borvik, 2001], [Majzoobi, 2011] and [Dzugan, 2013]. As the strain to fracture is influenced not only by the stress state but also the stress histories, the numerical data of these tests were also required. Furthermore, the failure parameters were finally calibrated based on different optimization methods by different researchers. Secondly, the strain-rate-relative-fracture-constant D_4 is obtained based mostly on the experimental results from a dynamic test [Johnson, 1985; Borvik, 2001]. Thirdly, D_5, as the temperature-relative-fracture-constant, is calibrated from the tests with elevated temperatures [Johnson, 1985; Borvik, 2001]. Vaziri et al. [2010] calibrated all constants in one approach so that the data from the ALE finite element simulations were calculated by an optimization method to obtain several sets of fracture constants, and one of the best sets was selected based on the performance as input in an updated Lagrangian based simulation of metal cutting.

1.2 Objective

The objective of this research is to calibrate reliable fracture constants for the Johnson-Cook fracture model, which is used as chip separation criteria in the finite element method simulation of metal cutting for AISI 1045 steel. The sub-objective is as follows:

1. Design experiments to calibrate the fracture constants of the Johnson-Cook fracture model with the use of low strain-rate experimental configuration.

2. Build finite element simulations of the corresponding experiments to verify the obtained fracture constants.

3. Acquire the Johnson-Cook fracture strain-rate coefficient D_4 from the metal cutting simulation and experiment.

4. Perform a parametric metal cutting simulation to verify and identify the limitation of the approach.

2. Literature Review

2.1 Ductile Fracture

2.1.1 Definition and Features of Ductile Fracture

Ductile fracture, which differs from brittle fracture, is a failure process that the material sustains in plastic deformation before it separates into pieces due to an imposed stress at the temperature lower than its melting temperature [Callister, 2007]. Figure 2.1 shows the comparison of the tensile stress-strain curves undergoing with or without a significant amount of plastic strains loaded to fracture, respectively for ductile and brittle materials [Callister, 2007]. Ductile fracture surfaces have special features that present necking regions with rough and irregular surfaces compared to the brittle one, as shown schematically in Figure 2.2. [Callister, 2007].

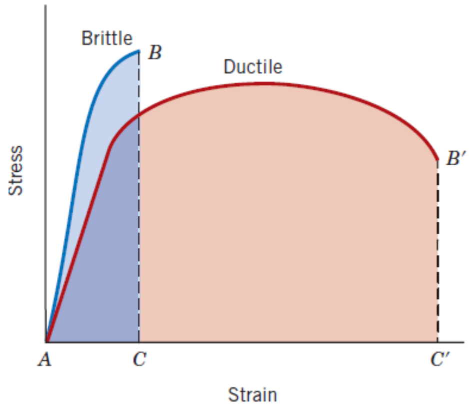

Figure 2.1: Schematic representations of the tensile stress-strain behavior of brittle and ductile materials loaded to fracture. [Callister, 2007]

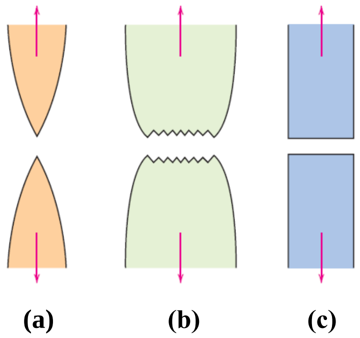

Figure 2.2: (a) Highly ductile fracture in which the specimen necks down to a point. (b) Moderately ductile fracture after some necking. (c) Brittle fracture without any plastic deformation. [Callister, 2007]

Three principal stages were observed in the ductile fracture: nucleation, growth and coalescence of voids as shown in Figure 2.3. Firstly, micro-voids nucleate at inclusions or second-phase particle when the interface stress elevates to the enough level to rupture the inter-facial bonds between the particle or inclusion and the matrix [Argon, 1975]. Secondly, the voids grow until the matrix attains to the plastic limit-load state by means of plastic strain and hydro-static stress [Thomason, 1998]. Thirdly, the inter-voids matrix happens to plastic limit-load failure across the sheet with strain localization between voids. Then it begins to neck down internally between the adjacent voids [Cottrell, 1959]. The voids further coalesce and the inter-void matrix cracks with a “knife-edge” fracture surface [Thomason, 1998].

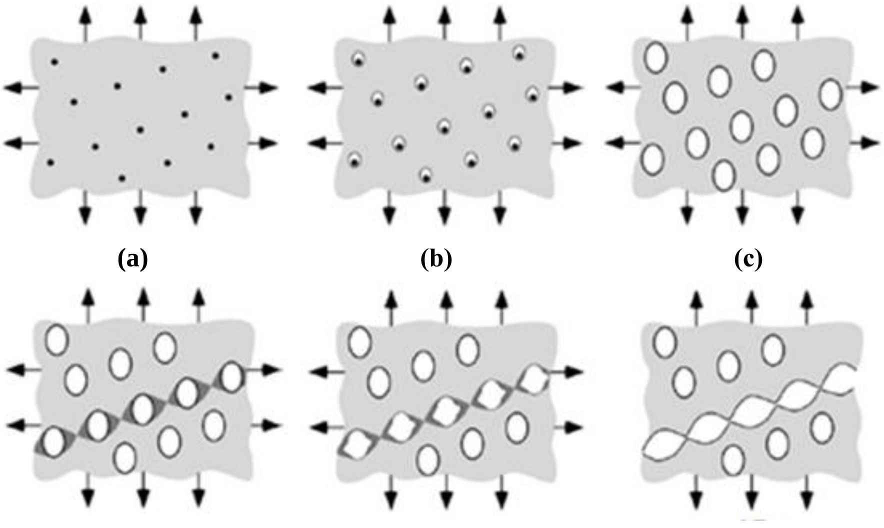

Figure 2.3: Void nucleation, growth, and coalescence in ductile metals: (a) inclusions in a ductile matrix, (b) void nucleation, (c) void growth, (d) strain localization between voids, (e) necking between voids, and (f) void coalescence and fracture. [Anderson, 2005]

A "cup and cone" shape was a typical ductile fracture feature obtained under uniaxial tensile tests. Figure 2.4 shows the "cup and cone" fracture process. After necking, some small micro-voids first form in the interior of the material as shown in Figure 2.4(b) [Callister, 2007]. The micro-voids then enlarge and coalesce to form a crack as shown in Figure 2.4(c), and the long axis of this elliptical crack perpendicular to the stress direction [Callister, 2007]. Finally, the crack propagates rapidly by the outer ring of the specimen, and shear deformation bands are formed at a 45-degree angle from the tensile stress axis as shown in Figure 2.4(d) [Anderson, 2005]. The central interior region of the fracture surface appears fibrous and irregular as shown in Figure 2.4(e) and Figure 2.4(a) [Anderson, 2005]. This characteristic surface is named "cup and cone" fracture because one of the fracture surfaces looked similar to a cup and the adjacent one looked similar to a cone as shown in Figure 2.5(a).

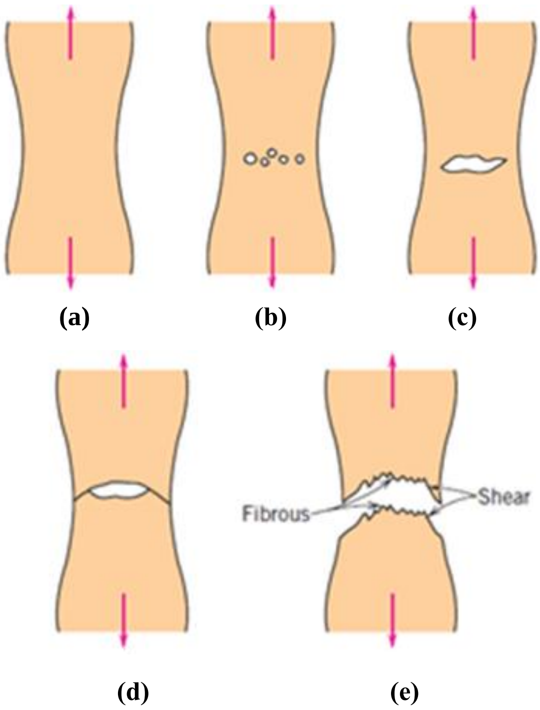

(a) (b) (c)

(d) (e)

Figure 2.4: Stages in the cup-and-cone fracture (a) Initial necking. (b) Small cavity formation. (c) Coalescence of cavities to form a crack. (d) Crack propagation. (e) Final shear fracture at a 45° angle relative to the tensile direction. [Ralls, 1976]

(a) (b)

Figure 2.5: (a) Cup-and-cone fracture in aluminum. (b) Brittle fracture in a mild steel.

Ductile fracture plays an important role in a successful finite element simulation of machining studied by Bil et al. [2004] and Liu and Guo [2000]. The criteria for fracture initiation and the evolution of fracture are necessary requirements in the finite element modelling. Two key factors on the ductile fracture behaviors are the loading conditions and the material itself. Moreover, the initiation of ductile fracture is affected by the stress state, temperature, and the strain rate, all of which will be discussed later.

2.1.2 *Effect of Stress State on Ductile Fracture*

The stress state is the most important factor to control the ductile fracture initiation. The stress state is usually defined based on three invariants of the stress tensor [σ], as shown in Equations (2.1), (2.2) and (2.3) respectively [Bai, 2009].

$$p = -\sigma_m = -\frac{1}{3}tr([\sigma]) = -\frac{1}{3}(\sigma_1 + \sigma_2 + \sigma_3) \tag{2.1}$$

$$q = \bar{\sigma} = \sqrt{\frac{3}{2}[S]:[S]} = \sqrt{\frac{1}{2}[(\sigma_1 - \sigma_2)^2 + (\sigma_2 - \sigma_3)^2 + (\sigma_3 - \sigma_1)^2]} \tag{2.2}$$

$$r = (\frac{9}{2}[S]\cdot[S]:[S])^{\frac{1}{3}} = [\frac{27}{2}\det([S])]^{\frac{1}{3}} = [\frac{27}{2}(\sigma_1 - \sigma_m)(\sigma_2 - \sigma_m)(\sigma_3 - \sigma_m)]^{\frac{1}{3}} \tag{2.3}$$

where [*S*] is the deviatoric stress tensor as detailed in Equation (2.4)

$$[S] = [\sigma] + p[I] \tag{2.4}$$

where [*I*] is the identity tensor and σ_1, σ_2 and σ_3 are the principal stresses, assuming $\sigma_1 \geq \sigma_2 \geq \sigma_3$ [Bai, 2009]. The stress triaxiality parameter η, as shown in Equation (2.5), as a dimensionless hydrostatic pressure, is defined by Bai et al. [2009].

$$\eta = \frac{-p}{q} = \frac{\sigma_m}{\bar{\sigma}} \tag{2.5}$$

where σ_m is the average of the three normal stresses, $\bar{\sigma}$ is the von Mises equivalent stress. The Lode angle θ is expressed by the relationship to the normalized third stress invariant ξ by Bai et al. [2009], as detailed in Equation (2.6)

$$\xi = (\frac{r}{q})^3 = \cos(3\theta) \tag{2.6}$$

The range of ξ is $-1 \leq \xi \leq 1$, for the range of the Lode angle is $0 \leq \theta \leq \pi/3$ [Bai, 2009]. Figure 2.6 shows that the stress state of a point consists of three coordinate systems: Cartesian coordinate system (σ_1, σ_2, σ_3), cylindrical coordinate system (σ_m, $\bar{\sigma}$, θ) and spherical coordinate system ($\bar{\varepsilon}_f$, φ, θ) [Bai, 2009]. The relationship between coordinate φ and the stress triaxiality η is shown in Equation (2.7) [Bai, 2009].

$$\eta = \frac{\sigma_m}{\bar{\sigma}} = \frac{\sqrt{2}}{3} c\tan\varphi \tag{2.7}$$

Moreover, the Lode angle can be obtained by Equation (2.8) [Bai, 2009].

$$\bar{\theta} = 1 - \frac{6\theta}{\pi} = 1 - \frac{2}{\pi} ar\cos\xi \tag{2.8}$$

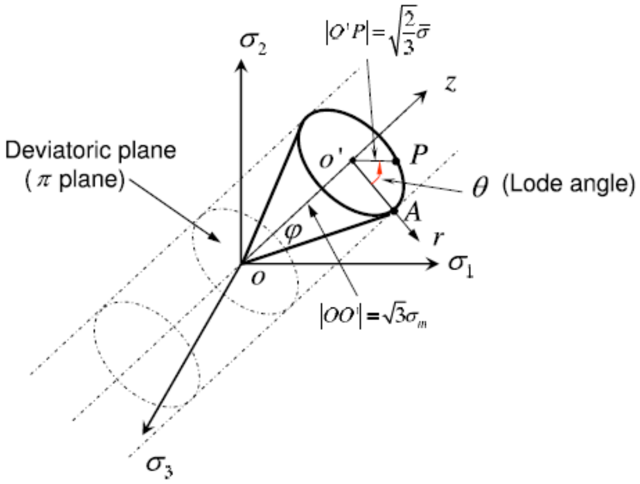

Figure 2.6: Three types of coordinate systems in the space of principal stresses. [Bai, 2009]

Bridgman [1952] observed that the ductility of material is highly sensitive to pressure [Bridgman, 1952]. Using the Bridgman piston-cylinder type hydrostatic pressure system, different steels or Fe-C materials were investigated, and the strain to fracture is examined increasing with the higher pressure by Bridgman [1952] and Davidson and Ansell [1968].

Furthermore, McClintock [1968] and Rice and Tracey [1969] inferred an expression of the relationship between the stress triaxiality and the strain to fracture by an analysis of the void growth. The function of $\hat{\varepsilon}_f(\eta)$ is shown in Equation (2.9).

$$\bar{\varepsilon}_f = \hat{\varepsilon}_f(\eta) = C_1 e^{-C_2\eta} \tag{2.9}$$

where C_1 and C_2 are material constants, and it is typically found that $C_2 = 1.5$. The studies of the void growth models like Equation (2.7) and the extensions are considered as the foundation of the modern ductile fracture mechanics [Bai, 2009]. Depending on these fracture mechanics, the criteria for fracture initiation are proved strongly by means of stress triaxiality by void growth mechanics modelling [Roy, 1981; Sun, 1991]. Similarly, the same conclusions are obtained based on other mechanics such as the continuum damage mechanics [Rosa, 2001] and are considered initiation and propagation-toughness-mechanics [Sun, 1991; Henry, 1997].

Additionally, depending on numbers of tests, more specific relationships between the stress triaxiality and the strain to fracture for different materials have been studied. Hancock and Mackenzie [1976] used tensile tests with pre-notched round specimens to explore a formula of $\hat{\varepsilon}_f(\eta)$ as listed in Equation (2.10).

$$\bar{\varepsilon}_f = \bar{\varepsilon}_n + \alpha \exp(-\frac{3}{2}\eta) \tag{2.10}$$

where $\bar{\varepsilon}_n$ is the void nucleation strain and α is material constant. This fracture model has been further extended by combining the effect of temperature and strain rate upon strain to fracture by Johnson and Cook [1985], which is the most popular fracture model used in the finite element of machining.

Specifically, the effect of stress triaxiality upon the strain to fracture for some materials, such as aluminum, is not monotonically in a wide range of stress triaxiality [Bao, 2003; Bao, 2004a]. Hence, a fracture locus describing different relationships of the stress triaxiality with a strain to fracture in a different range of the stress triaxiality is designed and studied from different tests [Bao, 2004a] as shown in Figure 2.7.

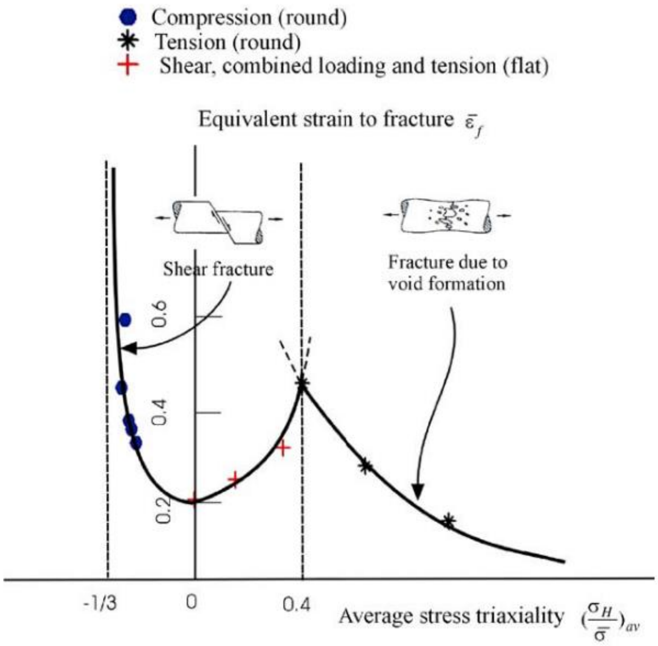

Figure 2.7: Dependence of the equivalents strain to fracture on the stress triaxiality. [Bao, 2004a]

The experimental results dominated by different fracture mechanisms are shown with three branches: $-\frac{1}{3} < \eta < 0$, $0 \le \eta < 0.4$, $\eta \ge 0.4$ [Bao, 2004a]. In the range $-\frac{1}{3} < \eta < 0$, results are obtained from the upsetting tests based on shear fracture mechanism, and the fitted curve of the experimental results is presented in Equation (2.11), which is developed based on the study by Wierzbicki and Werner [1998]. The other two fitted curves are obtained by simple parabolic fit, and they are presented in Equation (2.12) and Equation (2.13), respectively [Bao, 2004a].

$$\bar{\varepsilon}_f = 0.1225 \times (\eta + \frac{1}{3})^{-0.46} \quad \text{for} \quad -\frac{1}{3} < \eta < 0 \tag{2.11}$$

$$\bar{\varepsilon}_f = 1.9\eta^2 - 0.18\eta + 0.21 \quad \text{for} \quad 0 \le \eta < 0.4 \tag{2.12}$$

$$\bar{\varepsilon}_f = 0.15\eta^{-1} \quad \text{for} \quad 0.4 \le \eta \le 0.95 \tag{2.13}$$

It has been mentioned that the stress triaxiality related to the ductile fracture must be bigger than -0.33, which is so called cut-off value, for no material failure was observed when the stress triaxiality was smaller than -0.33 from the results of the upsetting tests [Bao, 2004a] and the tension tests [Bridgman, 1952].

However, this kind of fracture locus only contributes to a given material. The other materials have different fracture loci. For example, the fracture locus of AISI 1045 steel is monotonical as shown in Figure 2.8 [Bao, 2005]. The function of strain to fracture relates to the pressure for AISI 1045 steel based on the experimental results from Kao et al. [1990] as shown in Equation (2.14).

$$\bar{\varepsilon}_f = 1.25\exp(\frac{p}{1000}) \tag{2.14}$$

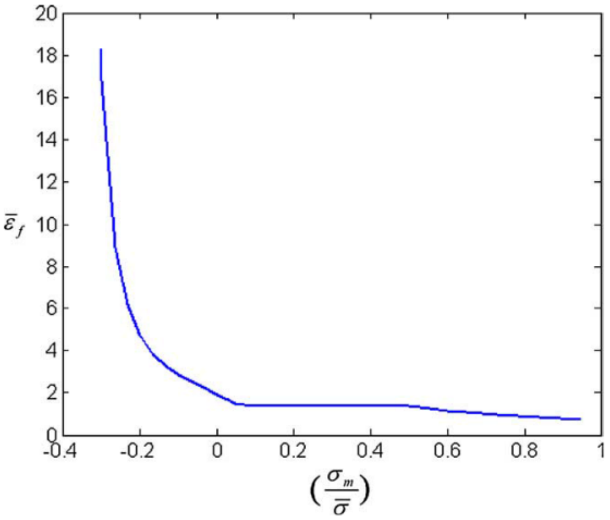

Figure 2.8: Assumed dependence of the equivalent strain to crack formation on the stress triaxiality of 1045 steel [Bao, 2005].

In addition, the effect of the stress state, consisting of both the pressure and the Lode angle, upon the ductile fracture is studied and described by a 3D (three-dimensional) fracture locus as shown in Figure 2.9 [Bai, 2008].

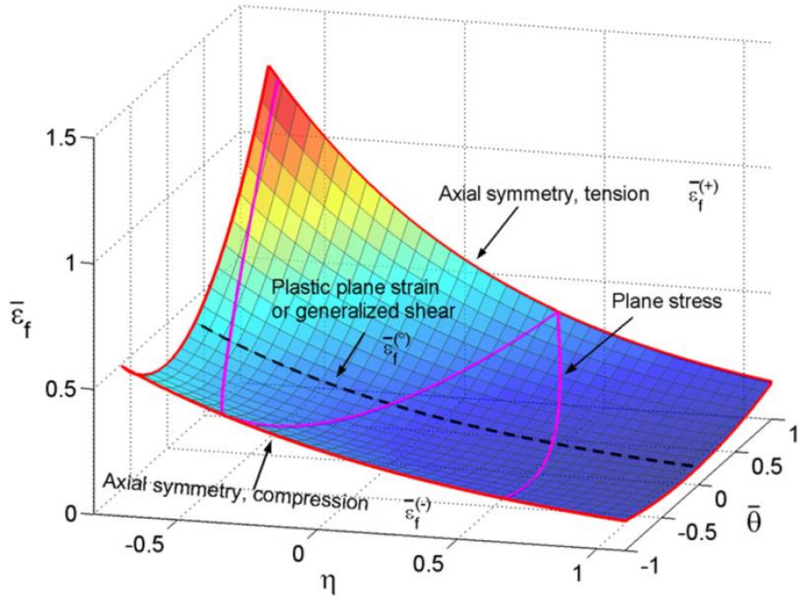

Figure 2.9: A newly postulated 3D asymmetric fracture locus. [Bai, 2008]

Equation (2.15) presents the 3D fracture locus of the strain to fracture affected by both stress triaxiality and Lode parameter [Bai, 2008].

$$\bar{\varepsilon}_f(\eta,\bar{\theta}) = [\frac{1}{2}(D_1e^{-D_2\eta}+D_5e^{-D_6\eta}) - D_3e^{-D_4\eta}]\bar{\theta}^2 + \frac{1}{2}(D_1e^{-D_2\eta}-D_5e^{-D_6\eta})\bar{\theta}+D_3e^{-D_4\eta} \quad (2.15)$$

2.1.3 Effects of Temperature and Strain Rate on Ductile Fracture

In metal cutting, the materials will deform under high strains, high strain rates, and high temperatures conditions. Hence, the effects of temperature and strain rate on ductile fracture are studied by Johnson and Cook [1985]. Figure 2.10 shows the experimental stress-strain curves for three different kinds of materials from the Split-Hopkinson tension-bar tests at elevated temperatures [Johnson, 1985]. The Split-Hopkinson tension-bar test is a dynamic test with an imposed stress wave on the specimens, and the device structure is shown in Figure 2.11.

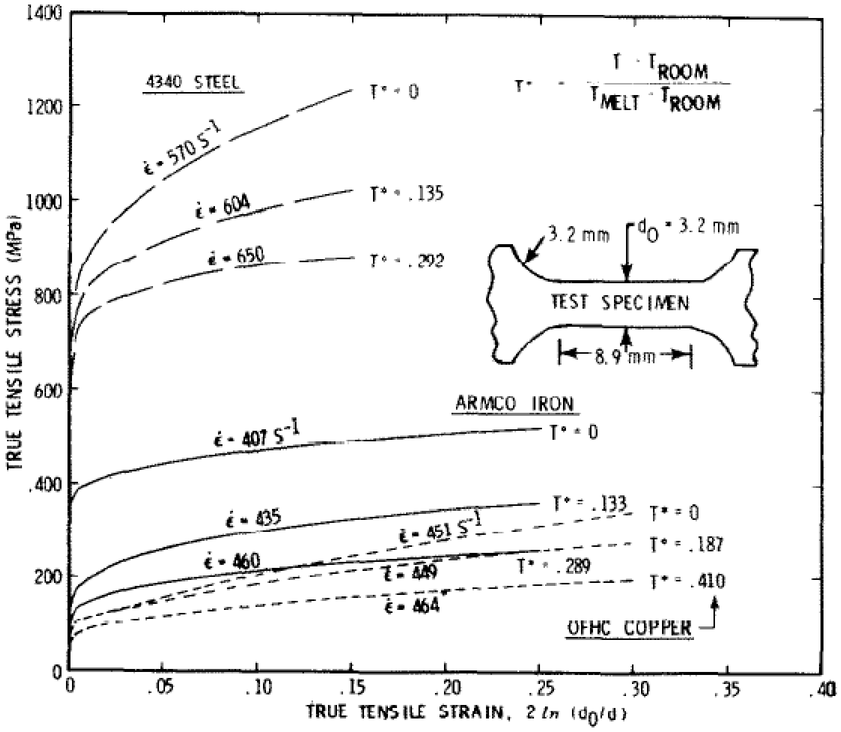

Figure 2.10: Average shear strains at fracture for the torsion tests. [Johnson, 1985]

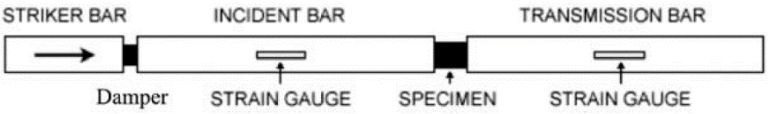

Figure 2.11: Split Hopkinson device. [Autenrieth, 2009]

Figure 2.12 shows the analysis effects of the strain and temperature on the fracture strain. The fitted straight lines were calculated by the “least squares” method to cover the average of temperatures for each test from the beginning to where the fracture occurs [Johnson, 1985]. Hence, it is shown that the ductility of material increases with higher temperatures. The effect of the strain rate on ductile fracture is also detailed in Figure 2.12 when at $T^*=0$, where T^* is the non-dimensional temperature. The ratio of the strain to fracture at high-strain-rate to low-strain-rate is greater than 1. In other words, a higher stain rate will increase the strain to fracture of material.

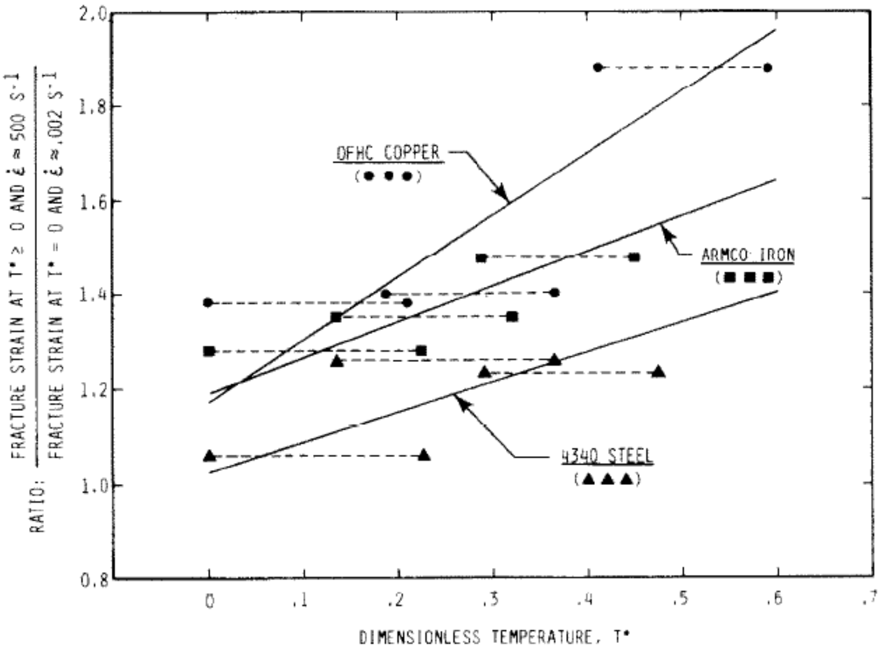

Figure 2.12: Effects of strain rate and temperature on the strain to fracture. [Johnson, 1985]

However, the effects of the temperature and strain rate on ductile fracture are not uniform for different materials. In other words, the influence of these two factors on ductility strongly depends on the material itself. Figure 2.13 shows totally different relationships between the strain-rate or the temperature to the strain to fracture for Weldox 460 E steel compared to the results from Johnson and Cook [1985]. As shown in Figure 2.13, the strain to fracture decreases with the strain rate increasing, and the temperature sensitivity of the fracture strain is not monotonous and is neglected. Especially, the effect of the temperature upon the strain to fracture only starts from 300ºC up to higher temperatures [Borvik, 2001].

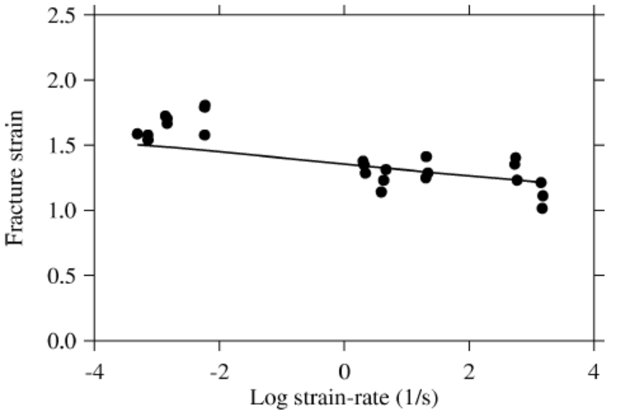

(a)

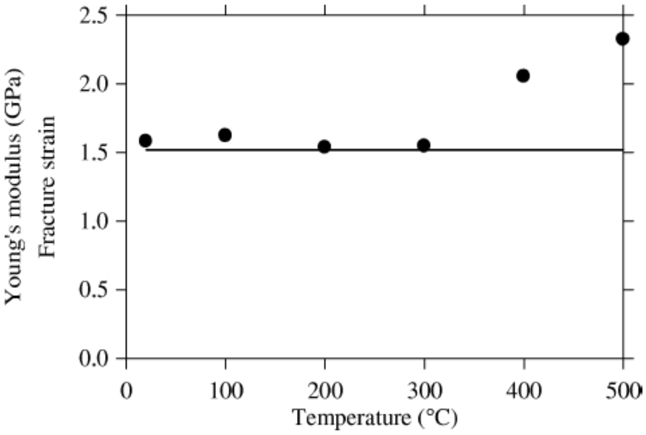

(b)

Figure 2.13: Comparison between experimental data (dotted lines) and model results (solid lines) for the target material of Weldox 460 E steel: (a) Fracture strain vs. Log strain rate, (b) Fracture strain vs. Temperature. [Borvik, 2001]

Besides, a similar phenomenon appears in the study for AISI 1045 steel as shown in Figure 2.14, so that the temperature has almost no effect on the strain to fracture up to a so called transition temperature for failure T_{tf}=176ºC [Autenrieth, 2009]. Moreover, the expression of this phenomenon in a failure model is created as shown in Equation (2.16) [Autenrith, 2009]. Furthermore, the effect of strain rate on failure strain for AISI 1045 steel is also studied by Autenrith et al. [2009]. As shown in Figure 2.15, the change of the strain to fracture for different strain rates is too small and it is neglected by Autenrith et al. [2009].

$$f_3(T) = \begin{cases} 1 & for T \le T_{tf} \\ H_3 - (H_3 - 1) \cdot (1 - (\frac{T - T_{tf}}{T_{melt} - T_{tf}})^{H_4})^{H_5} & for T > T_{tf} \end{cases} \tag{2.16}$$

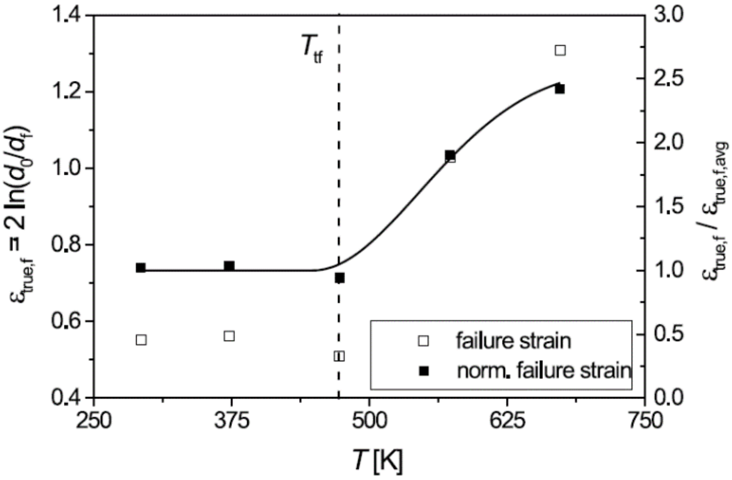

Figure 2.14: Dependences of averaged failure strain $\varepsilon_{true,f} = 2 \cdot ln(\frac{d_0}{d_f})$ and normalized failure strain for the tensile specimens at different temperatures. [Autenrieth, 2009]

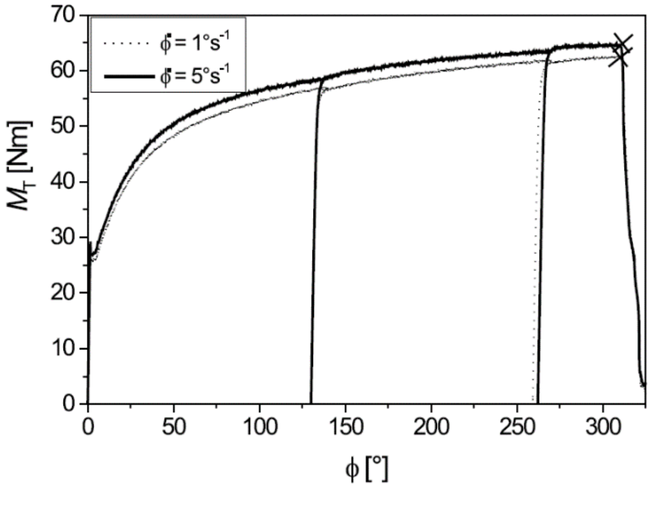

Figure 2.15: Torsion moment Mt in dependence on title angle ϕ for stress triaxiality p/σ_v=0 and different loading rates $\dot{\phi}$. [Autenrieth, 2009]

2.2 Ductile fracture models

Depending on the above studies of the fracture mechanisms, the fracture models are formulated to predict initial crack or failure, in particular, are implemented into the commercial codes in the finite element simulations. Some researchers evaluated different fracture models as guides for choosing a suitable fracture model for different loading conditions and different materials [Bao, 2004b; Wierzbicki, 2005; Teng, 2006; Liu, 2014; Duan, 2009].

2.2.1 Evaluation Studies of Fracture Models

Bao and Wierzibcki [2004b] compared and evaluated nine fracture models as the ductile-crack-formation-criteria for 2024-T351 aluminum alloy. The upsetting tests and round smooth and pre-notched tension tests and their corresponding finite element simulations were studied with these nine fracture models [Bao, 2004b]. The material fracture was in a range of negative and low to high stress triaxiality respectively as shown in Table 2.1 [Bao, 2004b]. They concluded that none of the fracture models produce a compatible result for the whole range of the considered stress triaxiality [Bao, 2004b]. The reason is the crack forms based on two totally different mechanisms imposed by the different range of stress triaxiality: void growth and shear decohesion [Bao, 2004b]. But some fracture models are suitable for narrowing the range of stress triaxiality. Concretely, the hydrostatic stress criterion and general Rice-Tracey model are good for a range of low to high stress triaxiality from the smooth and pre-notched tension tests, while the Cockcroft-Latham-Oh criterion works well for a range of a negative stress triaxiality from the upsetting tests [Bao, 2004b].

Furthermore, seven fracture models were evaluated for optimal fracture criteria in the finite element simulations (also for 2024-T351 aluminum alloy) based on a set of plane-stress tests and their corresponding finite element simulations [Wierzbicki, 2005].

Table 2.1: Formulas of fracture criteria, where $\bar{\varepsilon}$ and $\bar{\sigma}$ are the equivalent strain and stress respectively; $\bar{\varepsilon}_f$ is the equivalent strain to fracture; σ_1 and σ_2 are the maximum and intermediate principal tensile stress; σ_m is the hydrostatic stress, n is the hardening coefficient, $\upsilon = -\frac{2\dot{\varepsilon}_2}{\dot{\varepsilon}_1} - \dot{\varepsilon}_3$, $\dot{\varepsilon}_1 \geq \dot{\varepsilon}_2 \geq \dot{\varepsilon}_3$ are the rate of principle strains. [Bao, 2004b]

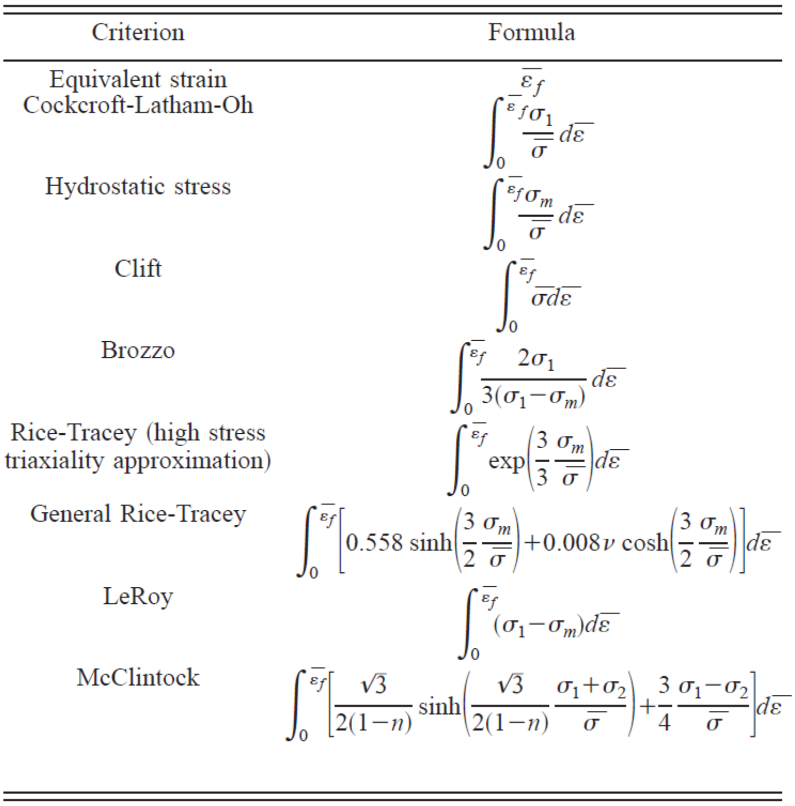

Criterion	Formula
Equivalent strain Cockcroft-Latham-Oh	$\bar{\varepsilon}_f$ $\int_0^{\bar{\varepsilon}_f} \frac{\sigma_1}{\bar{\sigma}} d\bar{\varepsilon}$
Hydrostatic stress	$\int_0^{\bar{\varepsilon}_f} \frac{\sigma_m}{\bar{\sigma}} d\bar{\varepsilon}$
Clift	$\int_0^{\bar{\varepsilon}_f} \bar{\sigma} d\bar{\varepsilon}$
Brozzo	$\int_0^{\bar{\varepsilon}_f} \frac{2\sigma_1}{3(\sigma_1 - \sigma_m)} d\bar{\varepsilon}$
Rice-Tracey (high stress triaxiality approximation)	$\int_0^{\bar{\varepsilon}_f} \exp\left(\frac{3}{3}\frac{\sigma_m}{\bar{\sigma}}\right) d\bar{\varepsilon}$
General Rice-Tracey	$\int_0^{\bar{\varepsilon}_f} \left[0.558 \sinh\left(\frac{3}{2}\frac{\sigma_m}{\bar{\sigma}}\right) + 0.008\nu \cosh\left(\frac{3}{2}\frac{\sigma_m}{\bar{\sigma}}\right)\right] d\bar{\varepsilon}$
LeRoy	$\int_0^{\bar{\varepsilon}_f} (\sigma_1 - \sigma_m) d\bar{\varepsilon}$
McClintock	$\int_0^{\bar{\varepsilon}_f} \left[\frac{\sqrt{3}}{2(1-n)} \sinh\left(\frac{\sqrt{3}}{2(1-n)} \frac{\sigma_1 + \sigma_2}{\bar{\sigma}}\right) + \frac{3}{4}\frac{\sigma_1 - \sigma_2}{\bar{\sigma}}\right] d\bar{\varepsilon}$

Figure 2.16 shows the comparison results of seven fracture models, which showed the Xue-Wierzbicki and CrachFEM models are good according to all tests [Wierzbicki, 2005]. The maximum stress fracture model fits well for all tests except the round bar tension test [Wierzbicki, 2005]. The Wierzbicki criterion only predicts well either in the range of stress triaxiality of $1/3 < \eta < 2/3$ or $-1/3 < \eta < 1/3$, but not in both [Wierzbicki, 2005]. And the other three fracture criteria are only useful in narrow ranges of the stress triaxiality [Wierzbicki, 2005]. In addition, it emphasized that all the evaluations of the fracture models are only made for the material used. In other words, the choice of the fracture model is strongly dependent on the material itself [Wierzbicki,

2005].

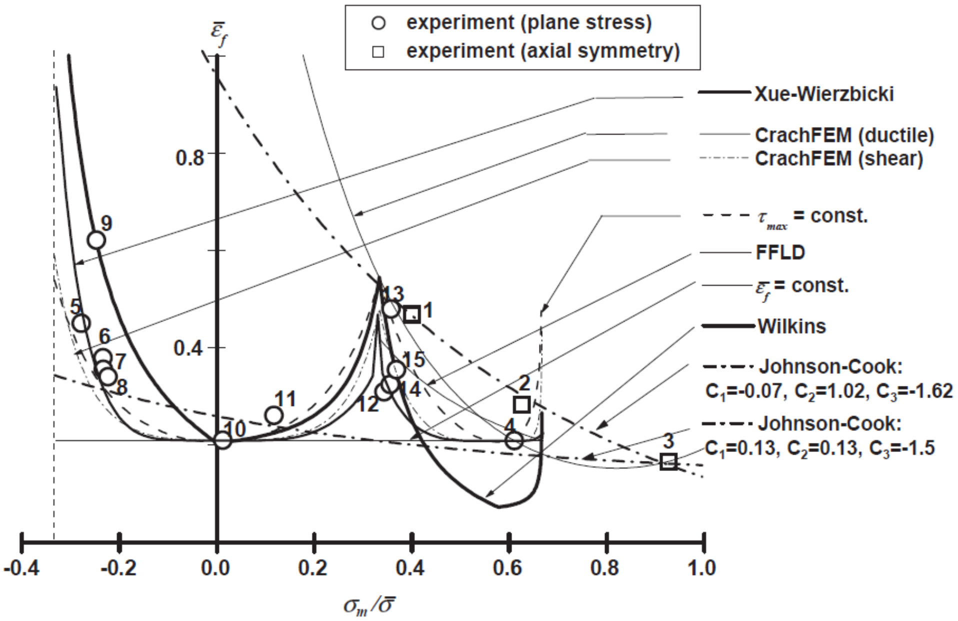

Figure 2.16: Comparison of prediction of all seven fracture criteria relatively to the set of 12 test points (plane stress) on 2014-T351 aluminum specimens. [Wierzbicki, 2005]

Moreover, as a continuation of the project, the applicability of six fracture models used in the dynamic loading condition, a high velocity perforation, were evaluated for Weldox 460 E steel and 2024-T351 aluminum alloy by applying a finite element simulation of a high-velocity perforation test [Teng, 2006]. It concluded that the Bao-Weizbicki fracture model was good at predicting the fracture phenomenon in perforation and that the Johnson-Cook fracture model was described as able to predict though not for the shear/compression test while the other four models were not able to predict this high velocity perforation test [Teng, 2006]. Additionally, a similar conclusion is obtained from another evaluation of six fracture models in the finite element simulation of metal cutting processes for 2024-T351 aluminum [Liu, 2014]. However, for AISI 1045 steel, the Johnson-Cook fracture model was proven able to predict chip separation in the finite element simulation of high speed cutting [Duan, 2009]. As the expected study is used in the finite element simulation of metal cutting, two optimum fracture models, the Johnson-Cook fracture model and the Bao-Wierzibcki fracture model, evaluated by [Liu, 2014] and [Duan, 2009] will be further discussed later.

2.2.2 Johnson-Cook Fracture Model

The Johnson-Cook fracture model is performed including effects of stress triaxiality, strain rate, and temperature on the strain to fracture respectively, as shown in Equation (2.17) [Johnson, 1985].

$$\varepsilon^f = [D_1 + D_2 \exp D_3 \sigma^*][1 + D_4 \ln \dot{\varepsilon}^*][1 + D_5 T^*] \tag{2.17}$$

where D_1, D_2, D_3, D_4, and D_5 are material parameters, σ^* is the ratio of the average of the three normal stresses to the von Mises equivalent stress assumed $\sigma^* \leq 1.5$, $\dot{\varepsilon}^*$ is the dimensionless strain rate, and T^* is the homologous temperature that $T^* = \frac{T - T_{room}}{T_{melt} - T_{room}}$ where T_{melt} and T_{room} are melting and room temperatures respectively. The first set of brackets of the formula expresses the effect of stress triaxiality on strain fracture monotonously, which follows the expression by [Hancock, 1976], and is traced back to the study of the void growth by McClintock [1968], Rice and Tracy [1969].

This model is based on damage-accumulated criteria assumed in a linear way as shown in Equation (2.18) [Johnson, 1985].

$$D = \sum \frac{\Delta\varepsilon}{\varepsilon^f} \tag{2.18}$$

where $\Delta\varepsilon$ is the increment of the equivalent plastic strain, and ε^f is the equivalent strain to fracture. The fracture occurs when $D = 1.0$.

The Johnson-Cook fracture model is applied widely because of the simplicity of formulation, the ease of calibration and a number of the material parameters provided by Johnson and Holmquist [1989]. However, Johnson and Cook [1985] only determined the positive range of the stress triaxiality based on some tensile tests and shear tests, and no small or negative value of stress triaxiality is expressed. For steel, Johnson and Cook [1985] even neglected the data of torsion testing in the fitting curve. Perhaps one function is not able to express two different fracture mechanisms over the range of stress triaxiality from negative to positive: shear decohesion and void growth. It is proved that ductility of aluminum is not a monotonic function of stress triaxiality [Wierzbicki, 2005]. To effectively apply the Johnson-Cook fracture model, researchers extended the model in different ways. Liu et al. [2014] proved that Johnson-Cook fracture model can be used as damage initiation coupled with damage evolution in metal cutting simulations. Moreover, the damage evolution combines the two different fracture modes effects. Bao and Wierzbicki [2004b] extended the Johnson-Cook fracture model in their fracture locus so that the part with high stress triaxiality is similar to Johnson-Cook fracture model while the other parts are expressed in different ways.

2.2.3 Bao-Wierzbicki Fracture Model

Bao and Wierzbicki [2004b] performed an empirical fracture model as the ductility of material based on the stress triaxiality. They found a “cut-off value” where the stress triaxiality equals -1/3, which means that no fail occurs if the stress triaxiality is less than this “cut-off value”. They also expressed the fracture locus in three branches for two different fracture mechanisms: void growth and shear decohesion as shown in the

Equation (2.19).

$$\overline{\varepsilon_{fh}} = \begin{cases} 0.1225\left(\dfrac{\sigma_H}{\bar{\sigma}} + \dfrac{1}{3}\right)^{-0.46} & -\dfrac{1}{3} < \left(\dfrac{\sigma_H}{\bar{\sigma}}\right) \le 0 \\ 1.9(\dfrac{\sigma_H}{\bar{\sigma}})^2 - 0.18\left(\dfrac{\sigma_H}{\bar{\sigma}}\right) + 0.21 & 0 < \left(\dfrac{\sigma_H}{\bar{\sigma}}\right) \le 0.4 \\ 0.15\left(\dfrac{\sigma_H}{\bar{\sigma}}\right)^{-1} & 0.4 < \left(\dfrac{\sigma_H}{\bar{\sigma}}\right) \le 0.95 \end{cases} \tag{2.19}$$

This model performed more comprehensive fracture behavior over a wide range of stress triaxiality that almost cover all kinds of fracture process. However, it is still required to extend with the strain rate and temperature effects on the ductile fracture. Hence, Liu et al. [2014] extended the Bao-Wierzibcki fracture model with the parts expressed strain rate and temperature effects in Johnson-Cook fracture model in Equation (2.20)

$$\bar{\varepsilon}_f = \bar{\varepsilon}_{fh}\left[1 + D_4 \ln\left(\frac{\dot{\bar{\varepsilon}}^{pl}}{\dot{\varepsilon}_0}\right)\right]\left[1 + D_5\left(\frac{T - T_{room}}{T_{melt} - T_{room}}\right)\right] \tag{2.20}$$

2.3 Calibration of the Johnson-Cook Fracture Model

The most important problem for implementing the Johnson-Cook fracture model into metal cutting simulation or other finite element analysis is to calibrate fracture constants for any proposed material.

Johnson and Cook [1985] calibrated the material constants for three kinds of materials: OFHC copper, Armco iron, and 4340 steel. Firstly, the fracture constants D_1, D_2, D_3 are calibrated based on quasi-static tensile tests with smooth and notched round bars and torsion tests as shown in Figure 2.17, and then adjusted the results to $\dot{\varepsilon}^* = 1.0$ using following obtained D_4. The strains to fracture were calculated by

$\bar{\varepsilon}_f = 2\ln(d_0 / d_f)$, where d_0 and d_f are the diameters of the initial and fractured cross section of the necking surface, which were measured by using a photograph of the specimens. The stress triaxiality used for fitting the curve is the average value of the stress triaxiality along the loading process. This stress triaxiality is obtained based on the stress history data of the point in the center of the necking zone from the numerical simulation of these quasi-static tensile tests. Specifically, the torsion data of 4340 steel was ignored, for it is so far from the proposed curve. *D_4 and D_5* were calibrated based on the ratio of the tensile Hopkinson bar test to quasi-static tensile tests as shown in Figure 2.17. The tensile Hopkinson bar test is a dynamic test with high strain rates and with elevated temperatures. However, the temperature effects were expressed with a low degree of accuracy here by Johnson and Cook [1985].

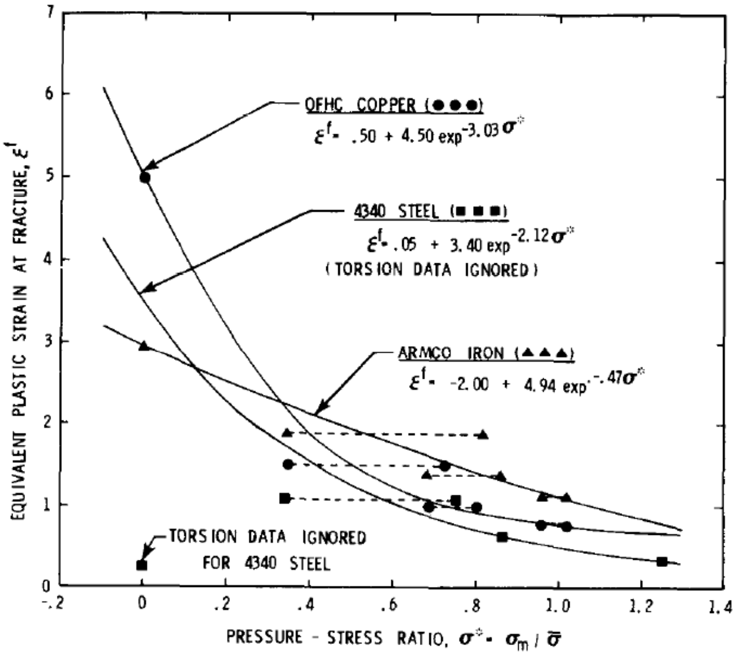

Figure 2.17: Fracture strain vs. Pressure-stress ratio for isothermal quasi-static conditions. [Johnson, 1985]

Borvik et al. [2001] determined the fracture parameters D_1, D_2, D_3 for Weldox 460

E steel based on quasi-static tensile tests with smooth and notched round bars without the use of numerical simulations, and using the method of least squares to minimize the residual of the fracture strain model, which is expressed in Equation (2.21).

$$\Re(\varepsilon_f) = \sum_{\beta=1}^{N_\beta} \sum_{\delta=1}^{N_\delta} \sum_{\gamma=1}^{N_\gamma} \left\{ \varepsilon_f^{\exp}(\sigma_\beta^*, \dot{\varepsilon}_\delta, T_\gamma) - (D_1 + D_2 \exp(D_3 \sigma_\beta^*))(1 + \dot{\varepsilon}_\delta^*)^{D_4} (1 + D_5 T_\gamma^*) \right\}^2 \quad (2.21)$$

where $\sigma_\beta^*, \dot{\varepsilon}_\delta, \dot{\varepsilon}_\delta^*, T_\gamma, T_\gamma^*$ are the discrete value of the stress triaxiality, the strain rate, the dimensionless strain rate, the temperature and the homologous temperature respectively. The material data at $\sigma^* = 0$ is estimated based on Equation (2.22) [Lemaitre, 1992].

$$\varepsilon_f = \varepsilon_{fs}^{\exp} [\frac{2}{3}(1+\nu) + 3(1-2\nu)(\sigma_{\max}^*)^2]^{-1} \quad (2.22)$$

where $\varepsilon_{fs}^{\exp}$ is the true fracture strain measured from a smooth specimen test. However, the extent of the curve with the results of D_1, D_2, D_3 to the range $\sigma^* < 0$ only depended on the hydrostatic tests. D_4 was calibrated based on data from dynamic tensile tests at room temperature and minimized the residual of Equation (2.21). D_5 was calibrated based on data from the quasi-static tensile tests at elevated temperatures with smooth specimens, and $D_5 = 0$ at range from 0ºC to 300ºC as shown in Figure 2.13(b). Figure 2.13(a), 2.13(b), and Figure 2.18 show the comparison between the experimental data and the model results based on the calculated material parameters, respectively.

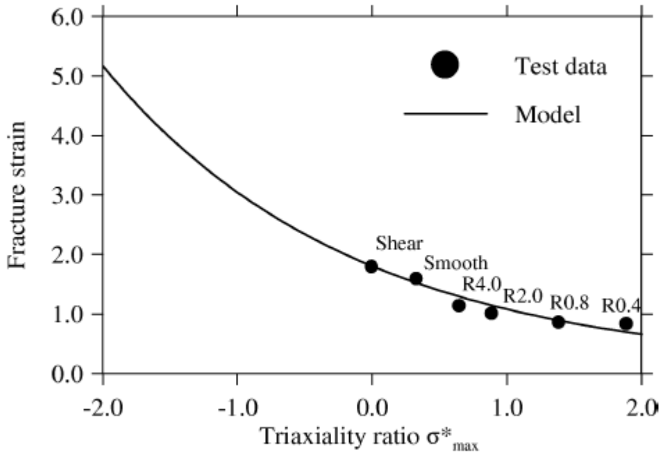

Figure 2.18: Comparison between experimental data to model results for Weldox 460 E steel. [Borvik, 2001]

Tomasz Wierzbicki et al. [2005] only calibrated the D_1, D_2, D_3 for 2024-T351 aluminum alloy based on the quasi-static round smooth and notched tensile tests as shown in Figure 2.19. However, the calibrated curve only provides an upper bound curve for material ductility, and the fracture curve of the same material from Johnson and Holmquist [1989] provides a low bound curve for material ductility as shown in Figure 2.19. That means different results were obtained dependent on different experiments. The Johnson-Cook fracture model is only reliable in a certain range of stress triaxiality, and the material parameters are calibrated by using the experiments covering this range of stress triaxiality.

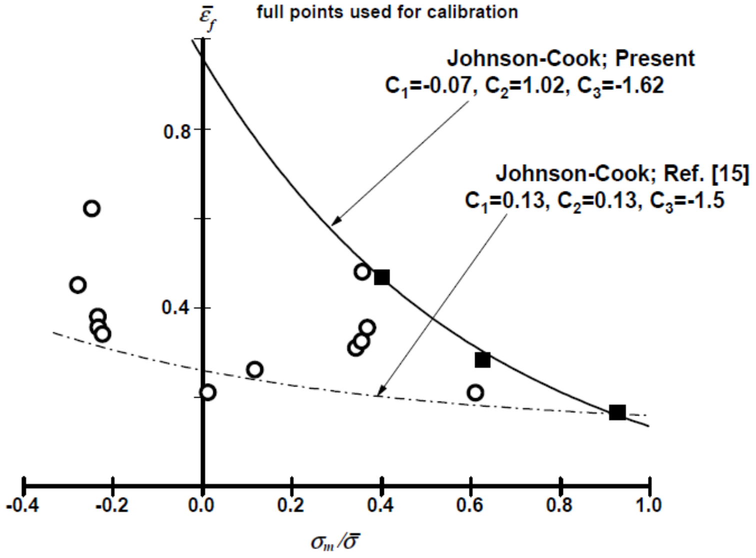

Figure 2.19: Comparison of ductility curves of aluminum. [Wierzbicki, 2005]

All above calibrations are dependent on experimental data, and some combined with the finite element simulated data. However, Vaziri et al. [2010] provided a new calibration for AISI 1045 steel that used the data from ALE based finite element simulation of metal cutting. The best set of material parameters were obtained by a nonlinear least-squares optimization procedure that the objective function is detailed in Equation (2.23) [Vaziri, 2010].

$$LSE = \min_{x} \sum_{i=1}^{4} f_i^2(x) \tag{2.23}$$

where x= [D_1, D_2, D_3, D_4, D_5] as a vector, and i expresses the different cutting conditions tests 1, 2, 3 and 4 respectively. The Johnson-Cook fracture model is based on the assumption that the elements fail when the accumulate damage value is $D = D_{c\,r}$= 1.0, as shown in Equation (2.24).

$$f_i(x) = 1.0 - \int_0^{\overline{\varepsilon f,i}} \frac{1}{[D_1 + D_2 \exp(D_3\sigma_i^*)][1 + D_4 \ln \dot{\varepsilon}_i^*][1 + D_5 T_i^*]} d\,\overline{\varepsilon_{p,i}} \tag{2.24}$$

where f_i is numerically integrated based on the trapezoidal method. Then the optimized sets of fracture parameters were obtained by using a MAPLE code to the program. The best set of fracture parameters is identified based on an updated Lagrangian simulation of metal cutting by comparing the predicted cutting forces and thrust forces to experimental results.

Majzoobi and Dehgolan [2011] calibrated the material parameters of the Johnson-Cook constitutive model and fracture model together. A method combining the experimental, numerical, and optimization technique is used. D_1, D_2, and D_3 were obtained based on a quasi-static tensile test with a notched bar. D_4 was obtained based on a dynamic test with a notched bar by using a high rate testing device "Flying wedge". However, no test of temperature effects on the fracture is studied here.

Dzugan et al. [2013] calibrated the fracture parameters based on the fracture locus $\bar{\varepsilon}_f(\eta, \xi)$ for the typical steel used in the nuclear power plant industry. They used three kinds of tests including tensile tests with notched round bars, punch tests, and a specially designed test with a specimen with a double curvature. All the tests are quasi-static tests at room temperature. Hence, only D_1, D_2, and D_3 were calibrated.

3. Experimental Procedures

3.1 Materials

The workpiece material investigated was AISI 1045 steel with chemical composition detailed in Table 3.1.The materials were cold rolled and annealed with a tensile strength of 758 MPa. The annealing process carried out was 923 K held at two hours followed by cooling down to room temperature within two hours in the oven. After the annealing process, the tensile strength was reduced to about 586 MPa.

Table 3.1: Chemical Composition of AISI 1045 steel (wt%).

Materials	C	Si	Mn	Ni	Cu	Cr
AISI 1045 steel	0.42~0.50	0.17~0.37	0.50~0.80	≤0.30	≤0.25	≤0.25

3.2 Tensile Specimens

The tensile specimens were un-notched and four unique geometries were pre-notched round bars. These specimens with five kinds of geometries will induce different stress triaxiality states according to Bridgman's [1952] analysis as shown in Equation (3.1).

$$\sigma^* = \frac{1}{3} + \ln(1 + \frac{a}{2R}) \tag{3.1}$$

where σ^* is the stress triaxiality state, R is the radius of curvature of the profile of the neck, and a is the radius of its minimum cross section [Bridgman, 1952]. The description of the specimen after necking or with pre-notched is shown in Figure 3.1.

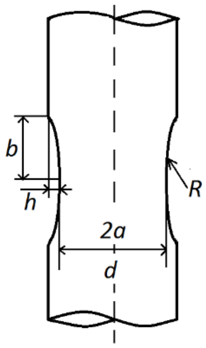

Figure 3.1: Description of the specimen at the necking region or pre-notched area.

The four different pre-notched specimens were designed with the same *a* and different *R* to get four different ratios, a/2R, and the corresponding stress triaxiality states as shown in Table 3.2: Dimensions and the stress triaxialities of all five kinds of tensile specimens. The ends of the specimen's shoulders were the threaded shoulders which eliminate slippage of the specimen during the test comparing to smooth shoulders with wedge grips.

Table 3.2: Dimensions and the stress triaxialities of all five kinds of tensile specimens.

Type of specimen	Radius of the center crosses section a (mm)	Local radius of a notch R (mm)	Ratio a/2R	Stress triaxiality η
Un-notched	6.35	0	-	0.33
Notched 1	3.81	9.525	0.2	0.52
Notched 2	3.81	6.35	0.3	0.60
Notched 3	3.81	3.175	0.6	0.80
Notched 4	3.81	1.5875	1.2	1.12

The dimensions and the geometries of all five un-notched and pre-notched round bars are shown in Figure 3.2.

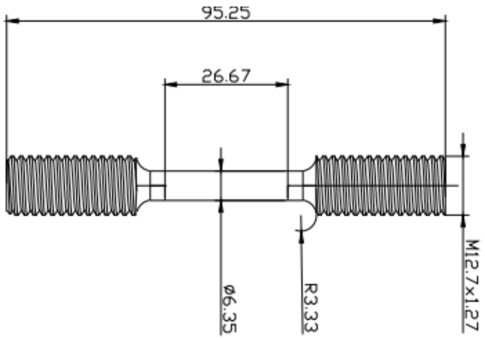

Un-notched

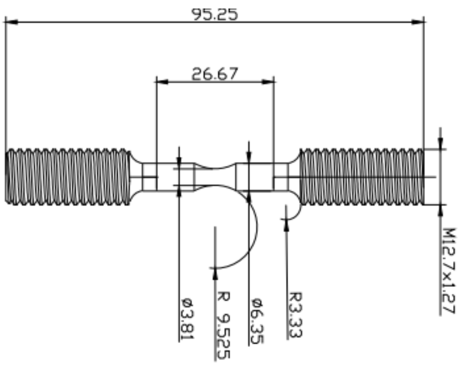

Notched No.1

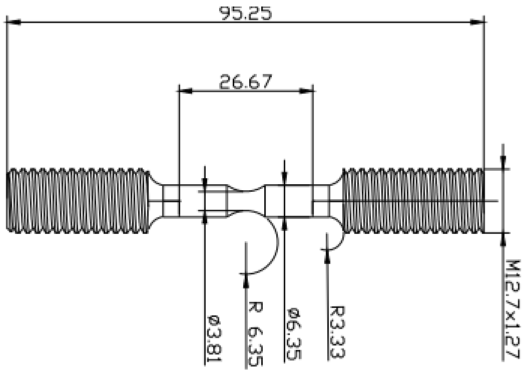

Notched No.2

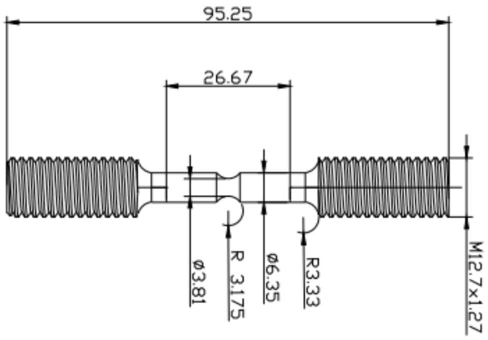

Notched No.3

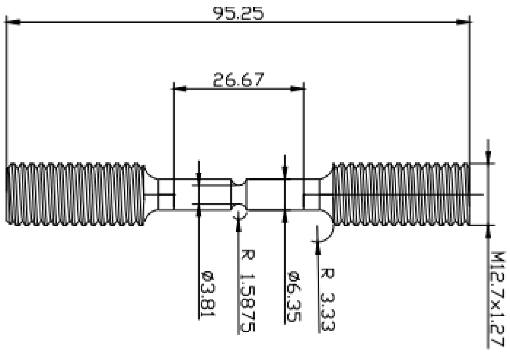

Notched No.4

Figure 3.2: Un-notched and pre-notched specimens (dimensions in mm).

3.3 Tensile test method

The tensile tests were performed at room and elevated temperatures (150˚C and 285˚C). An Instron SFL2702 Environmental Chamber was used on the MTS Series 810 hydraulic testing machine. The load cell system of the MTS testing machine was chosen at 250 kN. All the tests were performed with the same crosshead velocity of 0.016 mm/sec to ensure quasi-static conditions. Deformation behavior was viewed through the window of the environmental chamber by the CCD (Charge-coupled device) cameras. The digital image correlation (DIC) method was used to analyze the deformation patterns within gauge section with ARAMIS 6.1 software.

The tensile tests were performed at 25˚C, 150 ˚C, and 285 ˚C. The high temperature tests were warmed up to the set value 10 minutes prior to testing.

The tensile specimen is a threaded round bar fixed with two grips. The positions of the tensile specimen, upper grip, and bottom grip, are shown in Figure 3.3. The design of the grips is explained in APPENDIX A.

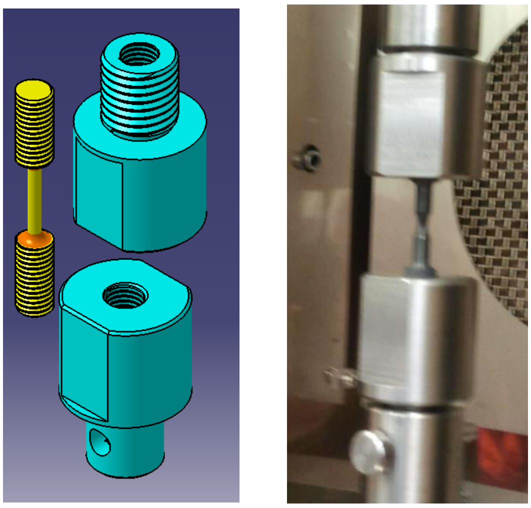

Figure 3.3: Positions of the specimens, upper grip, and bottom grip.

3.4 ARAMIS System

The deformation histories of the specimen throughout the tests were recorded with the ARAMIS system. This system performed the in-situation strain maps and analyzed the deformation of the specimens from beginning to fracture.

3.4.1 Specimen Preparation

The specimens were printed prior to testing as the preparation for ARAMIS based testing. The surface of the specimen was sprayed with a fine mist of black and white ink with a 0.5 mm nozzle, which deforms along with the specimen. The ink was chosen to withstand temperatures up to 650˚C, to prevent peeling off during the high temperature tests. The ink pattern was a high-contrast-random-marking, as shown in Figure 3.4, to determine the 2D or 3D coordinates of the surface of the specimen during the testing, and to get the fine accuracy of the deformation measurements.

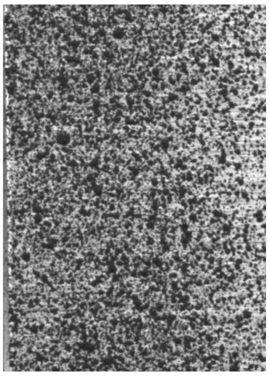

Figure 3.4: Random-mist-ink-pattern used to tensile specimens for ARAMIS testing.

3.4.2 Test Conditions

In the ARAMIS 2D system, one CCD camera with a resolution of 1280 x 1024 pixels was used. The position of the camera is shown in Figure 3.5: The camera was focused on the vertical center line of the specimen (Figure 3.5 (a)), and the focus distance was around 217 mm (Figure 3.5(b)). Optimal illumination of the cylinder surface was reached using two lamps, to avoid constant brightness on the center line of the specimen's surface. The fast-image recording was used with the upper limit of the ARAMIS system, defined as 1000 images for each test. The first image processing steps defined the macro-image facets. These facets were tracked in each successive image with a sub-pixel accuracy of 0.02 pixels (0.04 mm per pixel). The facet size was 13×13 pixels (with a spatial resolution of 0.04 mm per pixel) with a step size of 11 pixels. In some cases, the facet size was 9×11 or 11×13 pixels with a step size of 9 pixels to reach the optimal calculation. The images were calibrated with the diameter of the specimens 6.35 mm before the calculation of the strain map.

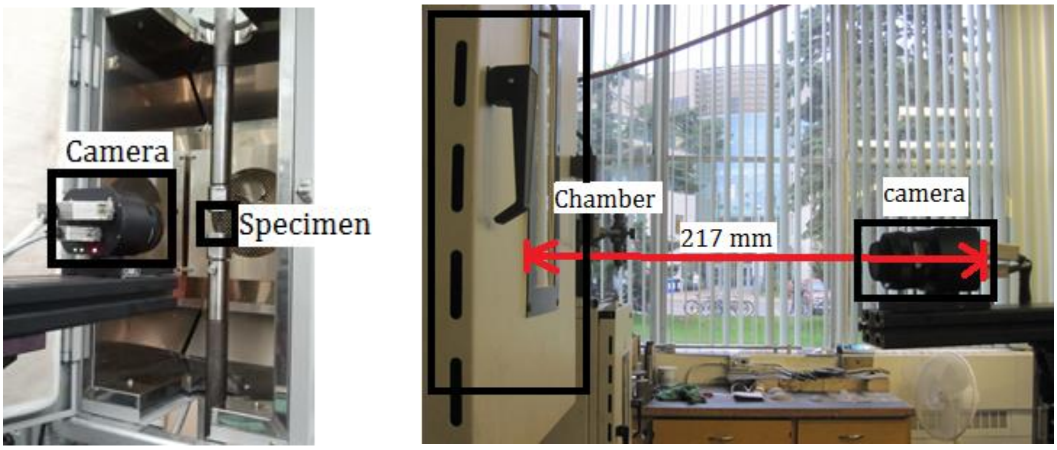

(a) **(b)**

Figure 3.5: The position of the camera in the Aramis 2D system.

3.4.3 Data Analysis

The projects were computed following the guidelines in the ARAMIS user manual. To obtain the true stress-strain curve, a point with a localized strain in the center of the specimen was selected. First, a section was taken along the center line of the specimen on the 2D strain map as shown in Figure 3.6(a). The true strain plot of the section at all stages before the fracture was shown in Figure 3.6(b). Figure 3.6 shows the localization of the specimen leading to the necking under the tensile tests. The point in the center with this strain localization was selected.

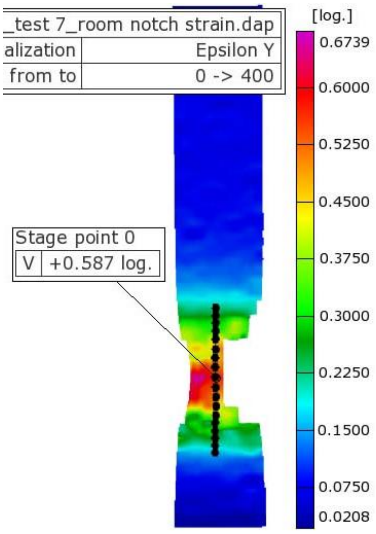

(a) 2D strain map with a section line to obtain data at different tensile displacements.

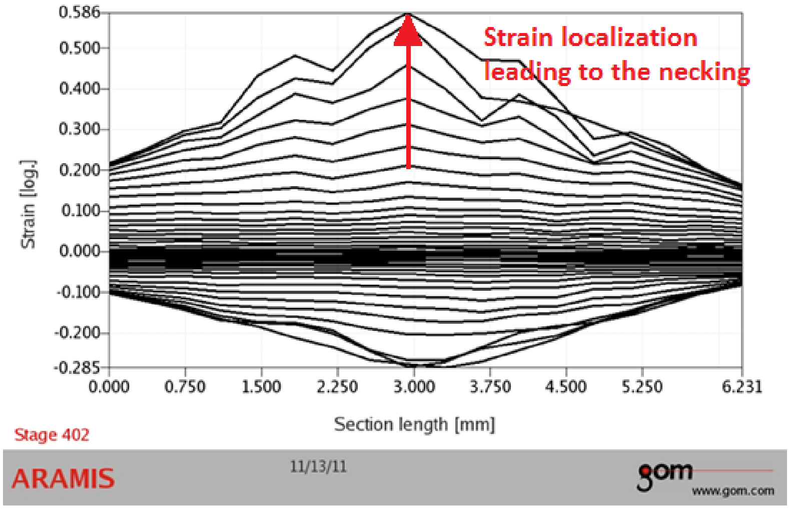

(b) True strain plot of the section line with all stages before fracture.

Figure 3.6: Example of results from Aramis system for plotting true stress-strain curve.

Figure 3.7(a) shows the true strain of the selected point through all stages from ARAMIS system. The data between stages 360 to 402 were unstable because of the error in the calculation of the grey values of the facet in the center area, which came from the large deformation after necking. The data were adjusted to be a smoother curve as shown in Figure 3.7(b). This adjusted strain epsilon Y (solid line) was used to plot the true stress-strain curve. Also, this strain was used to calculate the processing diameter of the center cross section area, *d*.

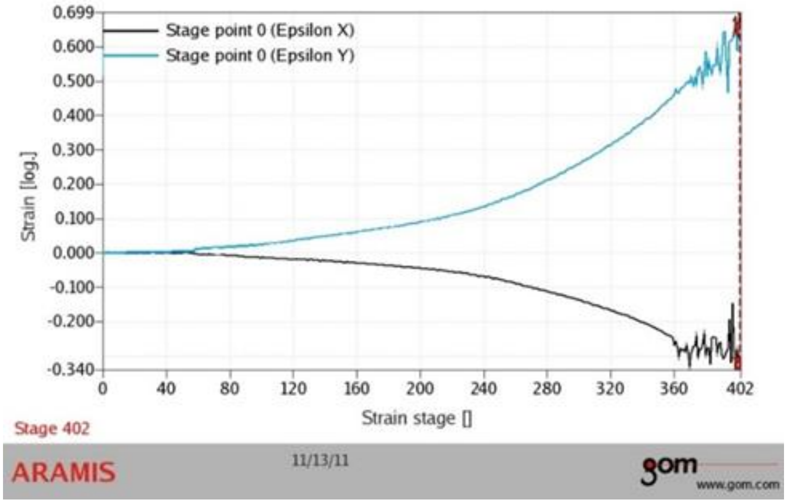

(a)Strain of the selected center point from the Aramis system

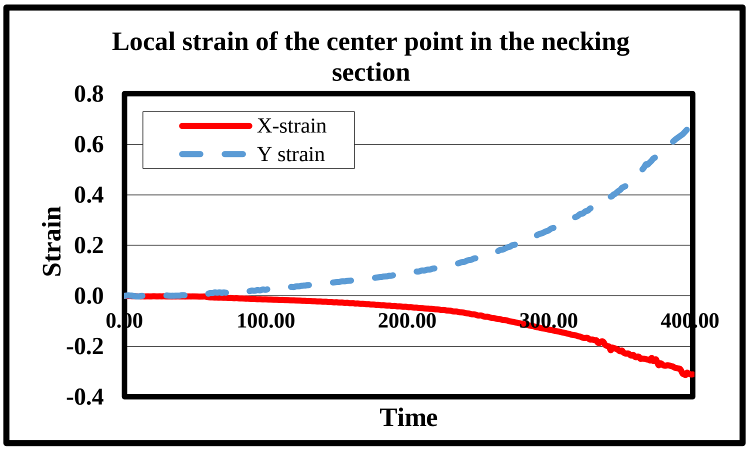

(b)Strain of the selected center point adjusted to smooth curve depending on the results from Aramis system

Figure 3.7: Example of the true strain of the center point with localized strain leading to necking.

To obtain the elongation of the tensile specimens, a line (Line 1) was taken along the vertical center line at the height of the notch, *2b*, as shown in Figure 3.8. Also, this length, *2b*, was used to calculate the radius of the notch, *R*.

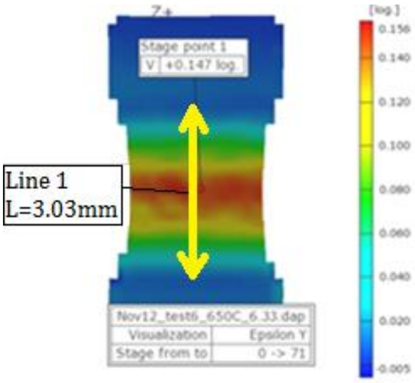

(a) Line 1 defined as the height of the notch at the 2D strain map.

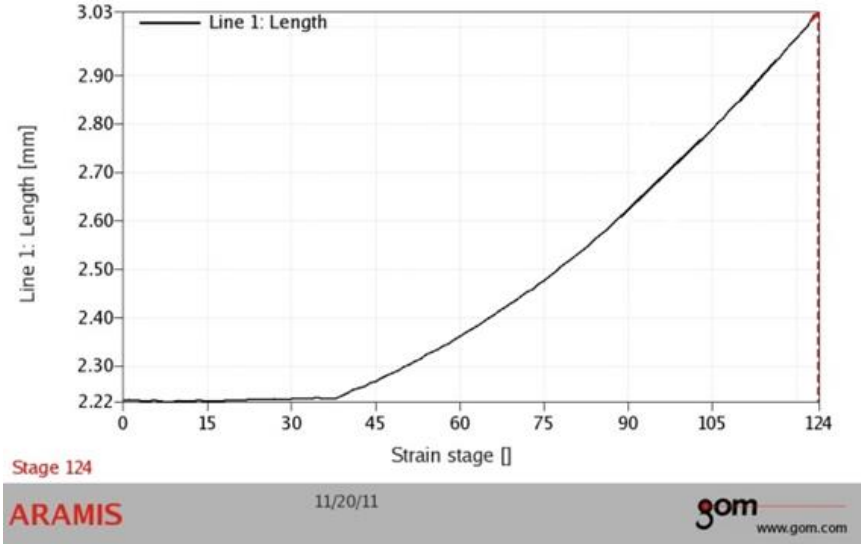

(b) The length of Line 1(yellow) through all strain stages.

Figure 3.8: Example of the gage line of the height of the notch, *2b*, in 2D strain map from ARAMIS system.

3.5 Annealing and Metallography

To soften the materials, annealing was used at different temperatures from 450˚C to 650˚C. Comparison of the yield stresses with different anneal conditions is shown in Figure 3.9. These plots show the true stress-strain curve adjusted with the power law, where the small circle shows the initiation of necking. The optimal anneal condition was selected as heating the specimen for two hours at 650˚C and after a cooling down to room temperature within two hours in the oven.

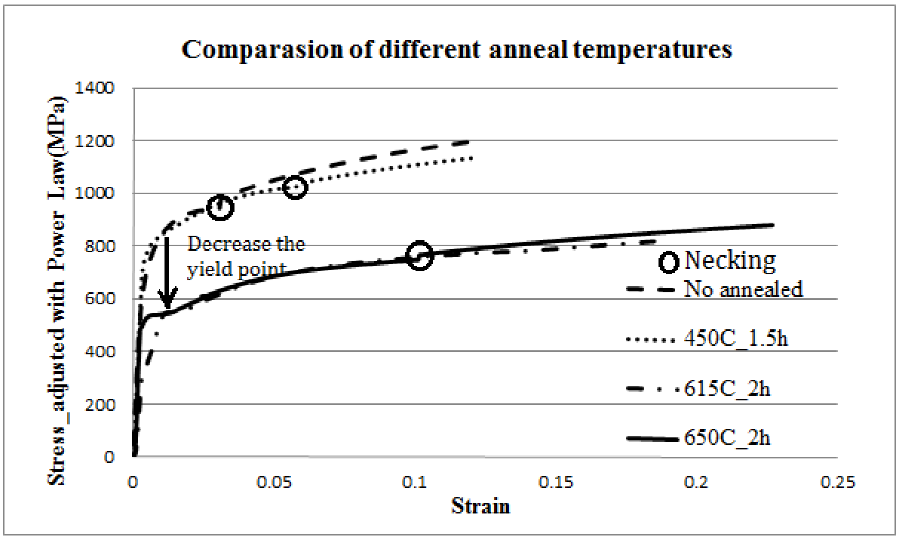

Figure 3.9: Comparison of the stress-strain curve under different anneal temperatures.

3.6 Geometry Measurements

The fracture properties of the materials were characterized by the strain to fracture and stress triaxialities, and both of these values could be obtained from the dimensions of the geometries of the specimens. The measurements of the geometries of the specimens used the results from the ARAMIS system and the microscope before testing, as shown in Figure 3.10 and Figure 3.11, respectively. The diameter d_0 and the area A_f of the center cross section of the specimen before testing and after fracture were measured to compute the strain to fracture. The diameter d_f of the center cross-section of the specimen and the radius R_f of the notch after fracture were measured to compute the stress triaxialities, and also the reductions of areas were obtained depending on these measurements.

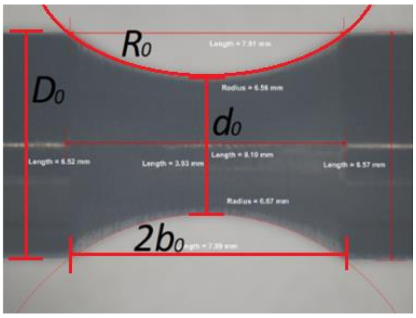

Figure 3.10: Example of the measurement of the geometry of specimen before testing.

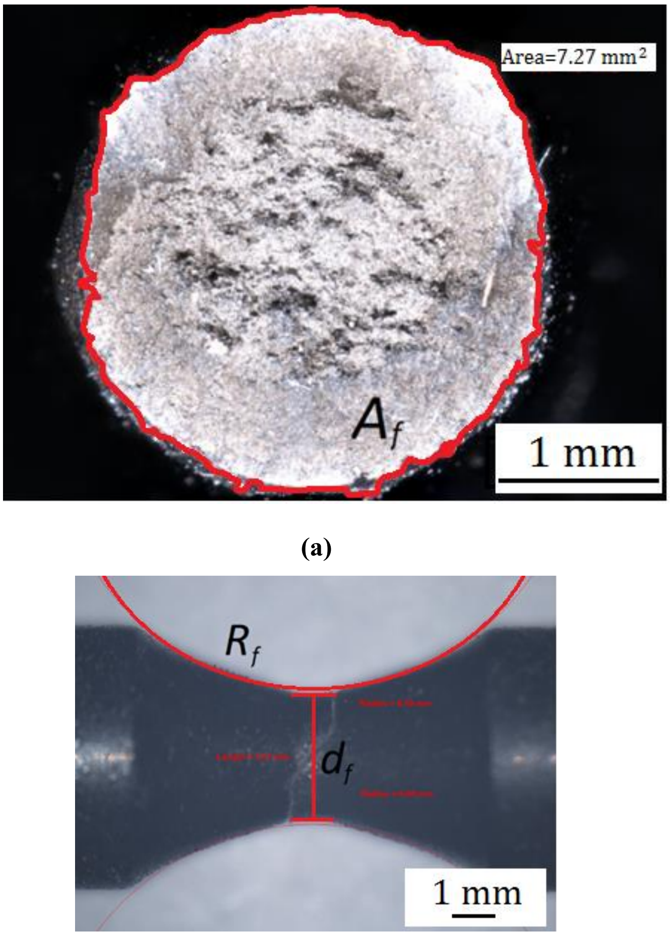

(a)

(b)

Figure 3.11: (a) The area of the central cross section of the fracture surface after testing; (b) The geometry measurements of the specimen after fracture.

4. Modelling Procedures

4.1 Modelling Procedures of Tensile Tests

To verify the method and the calibration of the obtained constants of the Johnson-Cook constitutive and fracture models, the tension tests were simulated by using ABAQUS/Explicit version 6.10. A dynamic coupled temperature-displacement analysis was used.

4.1.1 Mesh Conditions

Due to the symmetric nature of the specimens, the models are built as axisymmetric models as a quarter of the specimens under tension configuration. The element module CAX4RT is used, which is a coupled temperature-displacement element with four bilinear nodes and the ability to reduce integration with hourglass control. The mesh conditions for all the tension tests with different notched type are shown in Figure 4.1. Un-notched, R_0=9.525 mm, R_0=6.35 mm, R_0=3.175 mm, and R_0=1.5875 mm specimen meshes were generated and comprised of 1640, 490, 490, 460, 412 elements, respectively. The bottom elements of all models are meshed finer, for considering the fracture performance. The characteristic lengths of these elements were 0.2245 mm, 0.172 mm, 0.172 mm, 0.176 mm, 0.176 mm, respectively.

In a model with un-notched specimens, an initial imperfection is needed to get the necking performance. The initial imperfection used as 0.1% of the initial radius of the cross-section area is shown in Figure 4.2. The mesh conditions and element types are converged by using the force-displacement data and the reductions of area compared to the experimental data.

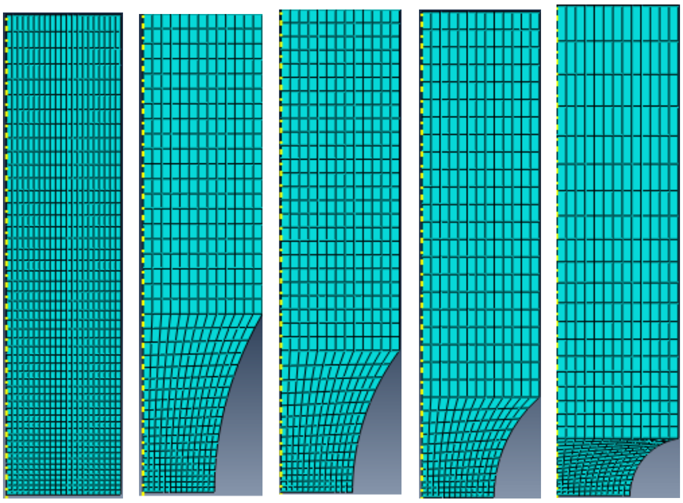

R0=9.525 R0=6.35 R0=3.175 R0=1.5875

Figure 4.1: Meshed models of the tensile tests of un-notched and pre-notched specimens. (mm)

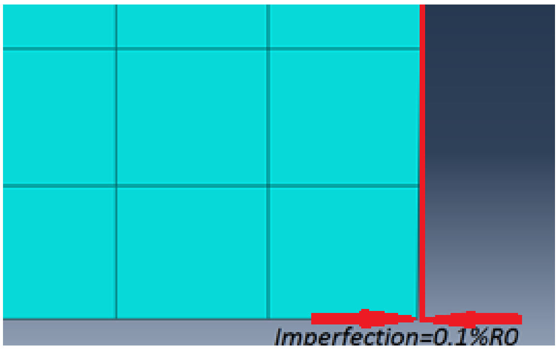

Figure 4.2: The initial imperfection in the un-notched model.

4.1.2 Material Properties

All the tension models are built using the uniformed units with m-kg-s. Some of the material properties of the AISI 1045 steel with annealing at 650˚C are shown in Table 4.1. Some other properties are temperature dependent data as shown in Table 4.2.

Table 4.1: Physical and mechanical properties of the material used in tension models.

Density (kg/m^3)	7850
Young's modulus (Pa)	2.05e11
Poisson's Ratio	0.29
Specific Heat (J/kg · C°)	486
Inelastic Heat Fraction	0.9

Table 4.2: Some temperature-dependent properties of the material use in tension models.

Temperature (C°)	Thermal conductivity (W/m · C°)	Expansion coefficient α (m/m · C°)
0	52	
20		1.01e-5
100	51	
200		1.2e-5
300	46	
400		1.3e-5
500	38	
600		1.53e-5
700	30	
1000	27	

The criterion of plastic property used is Johnson-Cook constrictive model as shown in Equation (4.1) [Johnson, 1983].

$$\sigma = [\mathrm{A} + \mathrm{B}\varepsilon^{n}][1 + Cln\dot{\varepsilon}^{*}][1 - T^{*m}] \tag{4.1}$$

where σ is the von Mises flow stress, ε is the equivalent plastic strain, $\dot{\varepsilon}^{*} = \dot{\varepsilon}/\dot{\varepsilon}_0$ is the dimensionless plastic strain rate, and $\dot{\varepsilon}_0 = 1.0\ s^{-1}$, T* is the dimensionless temperature, and $T^{*} = (T - T_{room})/(T_{melt} - T_{room})$ and T_{melt} is the melting temperature of the material, T_{room} is the room temperature [Johnson, 1983].

The material constants needed for this model are obtained by fitting the experimental data as shown in Table 4.3.

Table 4.3: The material constants of the Johnson-Cook constrictive model of tension material used in the simulation.

A (Pa)	B (Pa)	n (-)	m (-)	Melting temperature T_{melt} (˚C)	Transition temperature T_{room} (˚C)	C (-)	Epsilon dot zero $\dot{\varepsilon}_{ref}$ (-)
615.8e6	667.7e6	0.255	1.078	1350	25	0.0134	1

The criterion of the damage property is built as the damage initiation and evolution criteria in ABAQUS. The damage initiation criterion used was the Johnson-Cook fracture model as shown in Equation (4.2) [Johnson, 1985].

$$\bar{\varepsilon}_f = [D_1 + D_2 \exp(D_3\eta)][1 + D_4 \ln\dot{\varepsilon}^*][1 + D_5 T^*] \qquad (4.2)$$

where $\bar{\varepsilon}_f$ is the equivalent strain to fracture, and the dimensionless pressure-stress ratio (stress triaxiality) is defined as $\eta = \sigma_m/\bar{\sigma}$, where σ_m is the average of the three normal stresses, and $\bar{\sigma}$ is the von Mises equivalent stress. The dimensionless strain rate, $\dot{\varepsilon}^*$, and homologous temperature, T^*, are identical to those used in the Johnson-Cook constitutive model of Equation 4.1. D_1, D_2, D_3, D_4, and D_5 are material dependent fracture constants, which were acquired by fitting the experimental results as detailed in Table 4.4. Note that the sign of the constant D_3 should be changed from negative to positive, for the definition of the stress triaxiality in ABAQUS is opposite to the definition in the Johnson-Cook fracture model. The data in Table 4.4 were those used in the modelling using ABAQUS software.

Table 4.4: Fracture constants of the Johnson-Cook fracture model used in the modelling.

D_1	D_2	D_3	D_4	D_5	Melting temperature (C˚)	Transition temperature (C˚)	Reference Strain rate
0.04	1.03	1.39	0.002	0.46	1350	25	1

The damage evolution criterion used is the onset of the displacement of fracture.

The softening of the yield stress was assumed to be linear. The maximum displacement is calculated with the following steps.

Step 1: Determine the characteristic length L.

The definition of the characteristic length as shown in Equation (4.3) depends on the element geometry and formulation; it is a typical length of a line across an element for a first-order element [ABAQUS, 2003]. The size of the smallest element is 1.33e^{-4} by 1.51e^{-4}, so L is obtained as shown in Equation (4.3).

$$\mathrm{L} = \sqrt{(1.33e^{-4})^2 + (1.51e^{-4})^2} = 2.01e^{-4}(m) \tag{4.3}$$

Step 2: Acquire the true stress vs. displacement space as shown in Figure 4.3(b).

Using Equation (4.4), the undamaged part of this curve is transferred from the experimental true stress-true strain curve. The damaged part of this curve will be discussed in step 4.

$$\mathrm{u} = \mathrm{L} \times \varepsilon_t \tag{4.4}$$

Figure 4.3(a) shows the representation of the stress-displacement space curve, where u is the displacement space, d is the overall damage variable, and σ_{y0} is the onset of the damage stress, and E is the Young's modulus, and $\overline{\sigma}$ is the undamaged response stress, and $\bar{u}^{pl}$ is the equivalent plastic displacement, and $\bar{u}_f^{pl}$ is the equivalent plastic displacement at fracture, and line 1 is the elastic property along the onset of the damage.

Step 3: Determine the equivalent plastic displacement of fracture, $\bar{u}_f^{pl}$ as shown in Equation (4.5),

$$\bar{u}_f^{pl} = u_f - \bar{u}_0^{pl} \tag{4.5}$$

where $u_f = L \times \varepsilon_f = (2.01e-4) \times 0.6 = 1.2e-4(m)$, $\bar{u}_0^{pl}$ is the onset of the damage on the line 1 shown in Figure 4.3 (a). Assume the expression of line 1 using Equation (4.6).

$$\sigma(\mathrm{u}) = \frac{E}{L}u + C \tag{4.6}$$

where $\frac{E}{L} = \frac{2.05e11Pa}{2.01e-4m} = 1.02e15\frac{Pa}{m}$, C is a constant.

The point when it starts necking is in line 1, as shown in Figure 4.3(a). Take the coordinate value of this point, ($0.098 \times 2.01e^{-4}$, $646.8e^{6}$), into the expression of the line, to get the value of *C*. Table 4.5 shows a sample calculation.

Table 4.5: Sample calculation results.

C	$\bar{u}_0^{pl}$ (m)	$\bar{u}_f^{pl}$ (m)
$-1.945e10$	$1.907e-5$	1.009e-4

Step 4: Acquire the damaged stress-displacement curve.

The damaged stress-displacement space curve is calculated with Equation (4.7):

$$\sigma = (1 - \mathrm{d})\bar{\sigma} \tag{4.7}$$

where $\bar{\sigma}$ is the experimental results, as shown in Figure 4.3(b), *d* is obtained from the linear relationship with the equivalent plastic displacement, $\bar{u}^{pl}$, as shown in Figure 4.4.

Hence, Equation (4.8) and (4.9) detailed the function for *d* and σ, respectively.

$$\mathrm{d} = \frac{1}{\bar{u}_f^{pl}} \times \bar{u}^{pl} \tag{4.8}$$

$$d = \frac{1}{1.009\mathrm{e}-4} \times \bar{u}^{pl} = 9.911e3\bar{u}^{pl}$$

$$\sigma = (1 - \frac{1}{\bar{u}_f^{pl}} \times \bar{u}^{pl})\bar{\sigma} \tag{4.9}$$

$$\sigma = (1 - 9.911e3\bar{u}^{pl})\bar{\sigma} = \left[1 - 9.911e3 \times \left(u - \bar{u}_0^{pl}\right)\right] \times \bar{\sigma}$$

$$= \left[1 - 9.911e3 \times \left(L \times \varepsilon_t - \bar{u}_0^{pl}\right)\right] \times \bar{\sigma}$$

$$= [1 - 9.911e3 \times (2.01e - 4\varepsilon_t - 1.907e - 5)]\bar{\sigma}$$

$$= (1.189 - 1.992\varepsilon_t)\bar{\sigma}$$

where ε_t and $\bar{\sigma}$ are from the experimental result, then the damaged curve is obtained as shown in Figure 4.3(b).

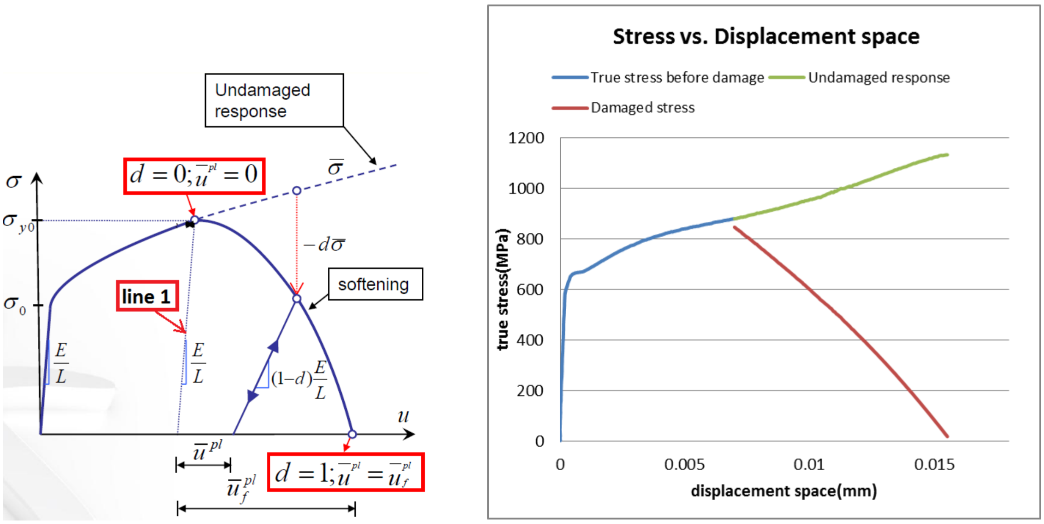

(a) **(b)**

Figure 4.3: (a) Schematic representation of tensile test data in stress-displacement space for elastic-plastic materials [ABAQUS lecture]; (b) The experimental stress vs. displacement space result.

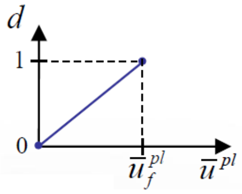

Figure 4.4: Linear relationship between d and $\bar{u}^{pl}$.

4.1.3 Boundary Conditions

As shown in Figure 4.5, the left side and the bottom of the model are fixed, as these regions were constrained by the other parts of the specimen as a quarter of the specimen was modeled. The tensile load was set at 4 m/s on the top edge of the model. The initial temperatures modeled were 25 C˚, 150 C˚, and 285 C˚.

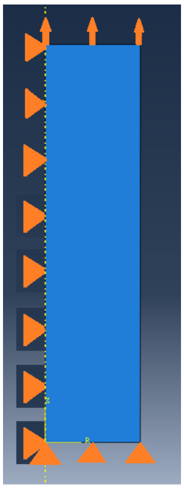

Figure 4.5: The boundary conditions of the tension model.

4.2 Lagrangian Orthogonal Cutting Modelling Procedures

To validate the constants for Johnson-Cook constitutive and failure models, an orthogonal cutting is simulated by using ABAQUS/Explicit version 6.10. A dynamic coupled temperature-displacement analysis was used. To study the material properties of cutting a work piece, the Lagrangian method was used. In addition, the conditional link element is built as shown in Figure 4.6, and the cutting tool was assumed to be elastic.

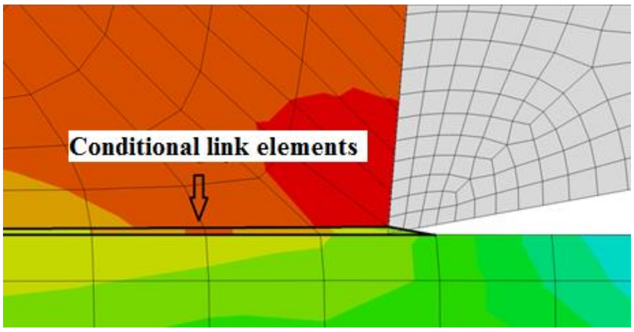

Figure 4.6: The conditional link element of the cutting work piece in models.

4.2.1 Geometry and Mesh Conditions

Due to plane strain assumption, the modelling is built as a 2D simulation. Figure 4.7 shows the geometry and mesh conditions of the models of the cutting work piece with three different feed rates. All the models had a cutting length of 10 mm, where the width of cut is 3 mm and the height of the conditional link element is 2 µm. The feed rates as shown are 0.1 mm, 0.2 mm and 0.3 mm.

The element type used in all models of the cutting work piece is CPE4RT, which is the element including four bilinear nodes with the ability to reduce integration and hourglass control using coupled temperature displacement module. The characteristic length of the element in the cutting layer is 40.05 µm, and the one in the uncut chip is 40.557 µm.

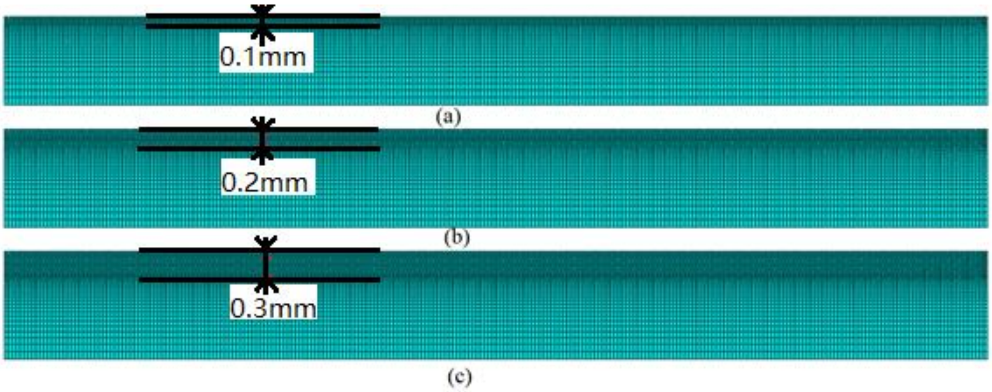

Figure 4.7: Geometry and mesh conditions for the work piece with three feed rates.

Figure 4.8 shows the geometry of the model of the cutting tool. The rake angle is 5 deg and the clearance angel is 10 deg, assuming that the tool cutting edge is sharp without the nose radius. The number of elements and nodes in the tool are 689 and 742 respectively. The cutting tool is set up as an elastic body, for the studied object is the material property of the cutting work piece. Additionally, the wear of tool assumed is not considered.

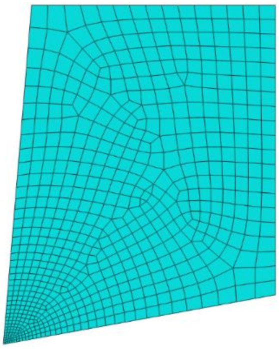

Figure 4.8: Geometry and mesh condition of the cutting tool.

4.2.2 Material Properties

The material properties used in the cutting work piece are built separately into two kinds, one where damage property is used with the cutting layer as the main studied object, whereas the other one is not. The material used for the work piece is the same as the one used for tensile models, which are shown in Table 4.3 and Table 4.4.

The material used for the cutting tool is a carbide tool [Kalhori, 2001], and its properties are shown in Table 4.6.

Table 4.6: Material properties of the carbide tool [Kalhori, 2001].

Young's Modulus, E (GPa)	560
Poisson's ratio, v *(-)*	0.22
Density, ρ (kg/m^3)	14500
Specific heat capacity, c_p (J/kg·˚C)	220
Thermal expansion, α (˚C^{-1} ×10^6)	5.4(20 ˚C) 5.3(200 ˚C) 5.4(400 ˚C) 5.6(600 ˚C)
Thermal Conductivity, k (W/(m·˚C))	34(20 ˚C) 38(250 ˚C) 42(500 ˚C) 45(750 ˚C) 47(1000 ˚C) 49(1250 ˚C)

4.2.3 Boundary Conditions and Temperature Conditions

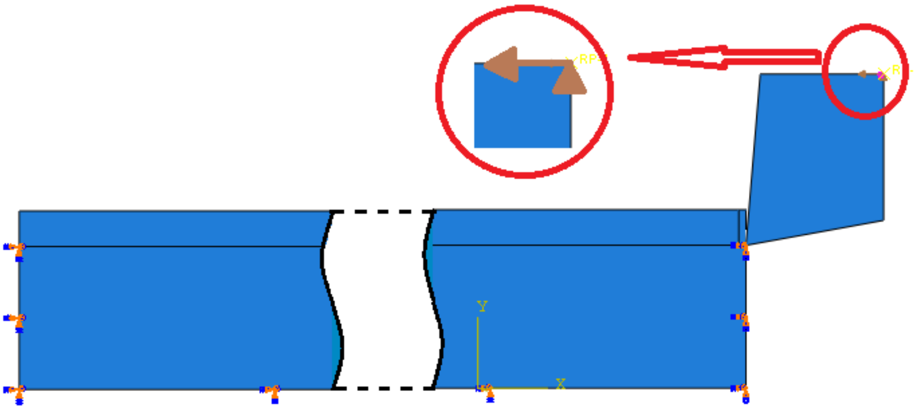

Figure 4.9: The boundary conditions of the cutting model.

Figure 4.9 shows the boundary conditions of the work piece and the cutting tool in the cutting models. The part under the cutting layer of the work piece is fixed. The cutting tool is fixed in a vertical direction and given a velocity to push left in a horizontal direction that is parallel to the original upper surface of the work piece. The velocities used in the cutting models are 150 m/min, 250 m/min, and 350 m/min. The initial temperature for both the work piece and the cutting tool is 25˚C.

4.2.4 Friction Conditions

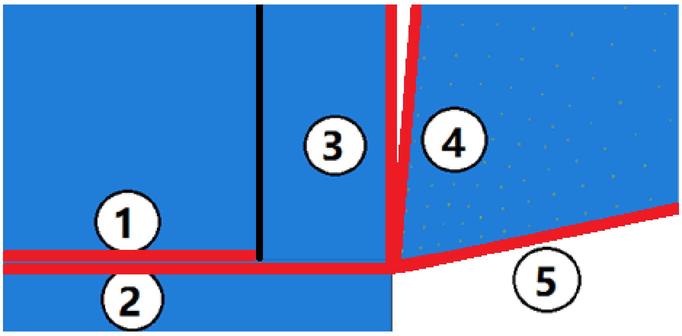

Figure 4.10: The contact surfaces as interacted pairs in the cutting models.

Figure 4.10 shows the contact surfaces used in the cutting models. Heat is generated from the sliding friction in the tool and chip interface. The Coulomb friction law is applied, and the friction coefficient is 0.22. All the other contact pairs are assumed with a friction coefficient equaling 0.

4.2.5 *Simulation Matrix*

The simulation matrix allows the verification of the Johnson-Cook failure criteria and the performance of the chip formation, cutting forces, temperatures, stresses, and strains as shown in Table 4.7.

Table 4.7: Simulation matrix of cutting models.

Cutting Speed (m/s) / Feed rate (mm)	150	250	350
0.1	Simulation 1	Simulation 2	Simulation 3
0.2	Simulation 4	Simulation 5	Simulation 6
0.3	Simulation 7	Simulation 8	Simulation 9

5. Results and Discussion

5.1 Verification of the Published Johnson-Cook Constitutive and Fracture Constants

The objective of this phase of the research was to employ published constants of the Johnson-Cook constitutive and fracture models to simulate the orthogonal cutting process. Tables 5.1 (a) and 5.1(b) show the published constants for Johnson-Cook constitutive and fracture models respectively by Borkovec [2008], Jaspers and Dautzenberg [2002], and Varizi et al. [2010].

Table 5.1: Published Johnson-Cook constants for AISI 1045 steel.
(a) Published Johnson-Cook constitutive constants.

Published Constitutive Constants	A (MPa)	B (MPa)	n (-)	C (-)	M (-)
[Borkovec, 2008]	375.0	552.0	0.457	0.020	1.400
[Jaspers, 2002]	553.1	600.8	0.234	0.0134	1.000

(b) Published Johnson-Cook fracture constants.

Published Fracture Constants	D_1	D_2	D_3	D_4	D_5
[Borkovec, 2008]	0.25	4.38	-2.68	0.002	0.61
[Varizi, 2010]	0.05	4.22	-2.73	0.0018	0.55

The orthogonal-cutting finite-element-model is based on the Lagrangian formulation method. The fixed cutting parameters used were 250 m/min cutting speed, 0.2 mm un-deformed thickness, +5 deg rake angle, and 3 mm width of cut. The coefficient of friction was assumed to be 0.22, and the tool was assumed to be infinitely sharp and have no cutting-edge-radius. Two simulations were carried out: one based on Borkovec's [2008] constitutive and fracture constants, and the other with Jaspers and Dautzenberg's [2002] constitutive together with Varizi et al. [2010] fracture constants.

Figures 5.1(a) and 5.1(b) show the Von Mises and temperature contour plots respectively when using fracture constants published by Borkovec [2008]. The simulation with the Borkovec's [2008] fracture constants terminated at 4% of the total simulation time. The termination was due to the entanglement of the workpiece elements with the cutting edge. This phenomenon was very likely because the fracture strain determined by Borkovec [2008] was too high. Therefore, the chip could not separate from the workpiece. A similar trend was observed when using the fracture constant determined by Varizi et al. [2010], as shown in Figure 5.1(c) and 5.1(d). However, the simulation with Varizi et al. [2010] fracture constants was terminated at 41% of the total simulation time. Element entanglement was also observed from Figure 5.1(c) and 5.1(d). That Varizi et al. [2010] fracture constants could simulate longer cutting time was likely due to a substantially lower D_1 value when compared to those published by Borkovec [2008]. The preliminary results detailed in Figure 5.1(a) to 5.1(d) concluded that the fracture constants published by Borkovec [2008] and Varizi et al. [2010] cannot be used to simulate orthogonal cutting. From the cutting model with Varizi's [2010] fracture constants, the predicted hydrostatic pressure and Von Mises stress were -342 MPa and 1110 MPa, respectively. Therefore, the triaxiality ratio was equal to 0.31. The fracture strain computed with Varizi et al. [2010] fracture constants required a strain of 1.9 to induce fracture.

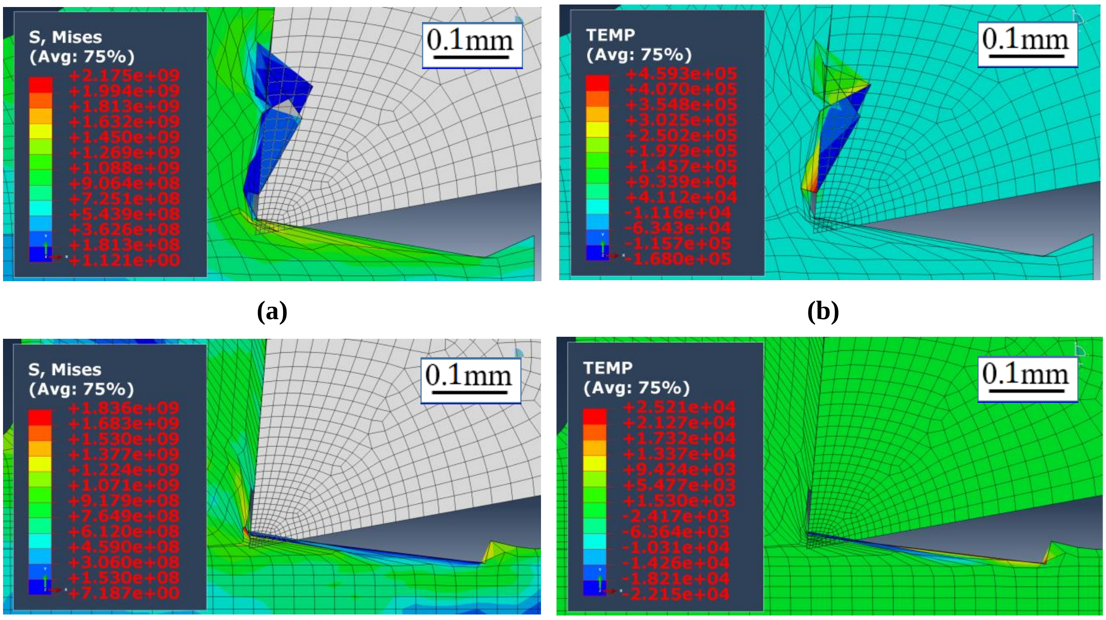

(a) **(b)**

(c) **(d)**

Figure 5.1: The modelling performance with historical constants of the Johnson-Cook models: (a) Von Misses stress contours with constants from [Borkovec, 2008]; (b) Temperature contours with constants from [Borkovec, 2008]; (c) Von Misses stress contours with constants from [Varizi, 2010]; (d) Temperature contours with constants from [Varizi, 2010].

However, experimental work published by Bai et al. [2009] showed in Figure 5.2 that the fracture strain measured was between 0 and 0.5. Therefore, the values determined by Borkovec [2008] and Varizi et al. [2010] were too large.

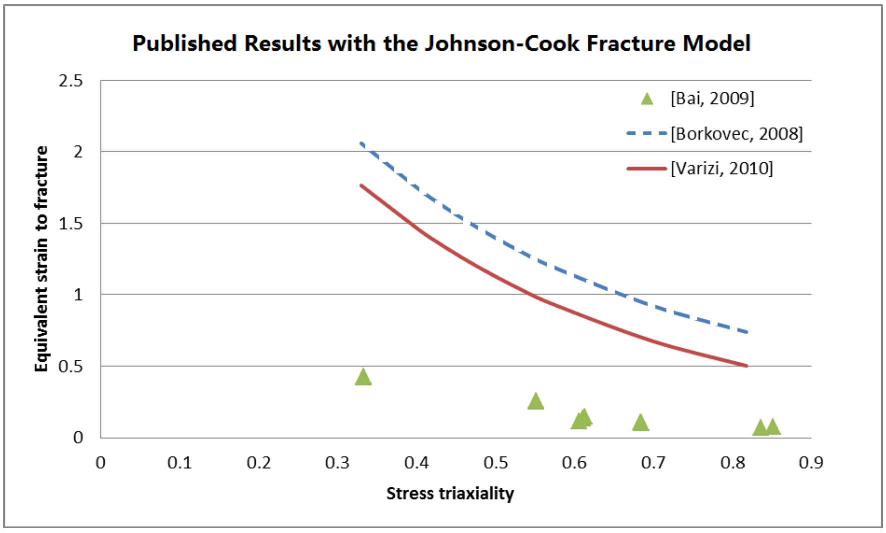

Figure 5.2: Comparison of the published Johnson-Cook fracture curves from Borkovec [2008] and Varizi et al. [2010] with the experimental results from Bai et al. [2009].

The stress triaxiality magnitudes along the conditional link elements were in the range of 0.3 to 0.5 during metal cutting simulation. With the range of stress triaxiality values mentioned earlier, uniaxial tensile tests have to be performed to acquire the Johnson-Cook fracture constant with a different temperature at low strain rates.

Before performing experiments to determine Johnson-Cook fracture constants, uniaxial tensile tests have to be carried out to determine the Johnson-Cook strain hardening component constants and to compare the constants with those acquired by Borkovec [2008] and Jaspers and Dautzenberg [2002].

5.2 Flow-chart for the Calibration and Verification of the Johnson-Cook Constitutive and Fracture Constants

The flow-chart for the calibration and the verification of the whole Johnson-Cook constitutive and fracture constants are shown below.

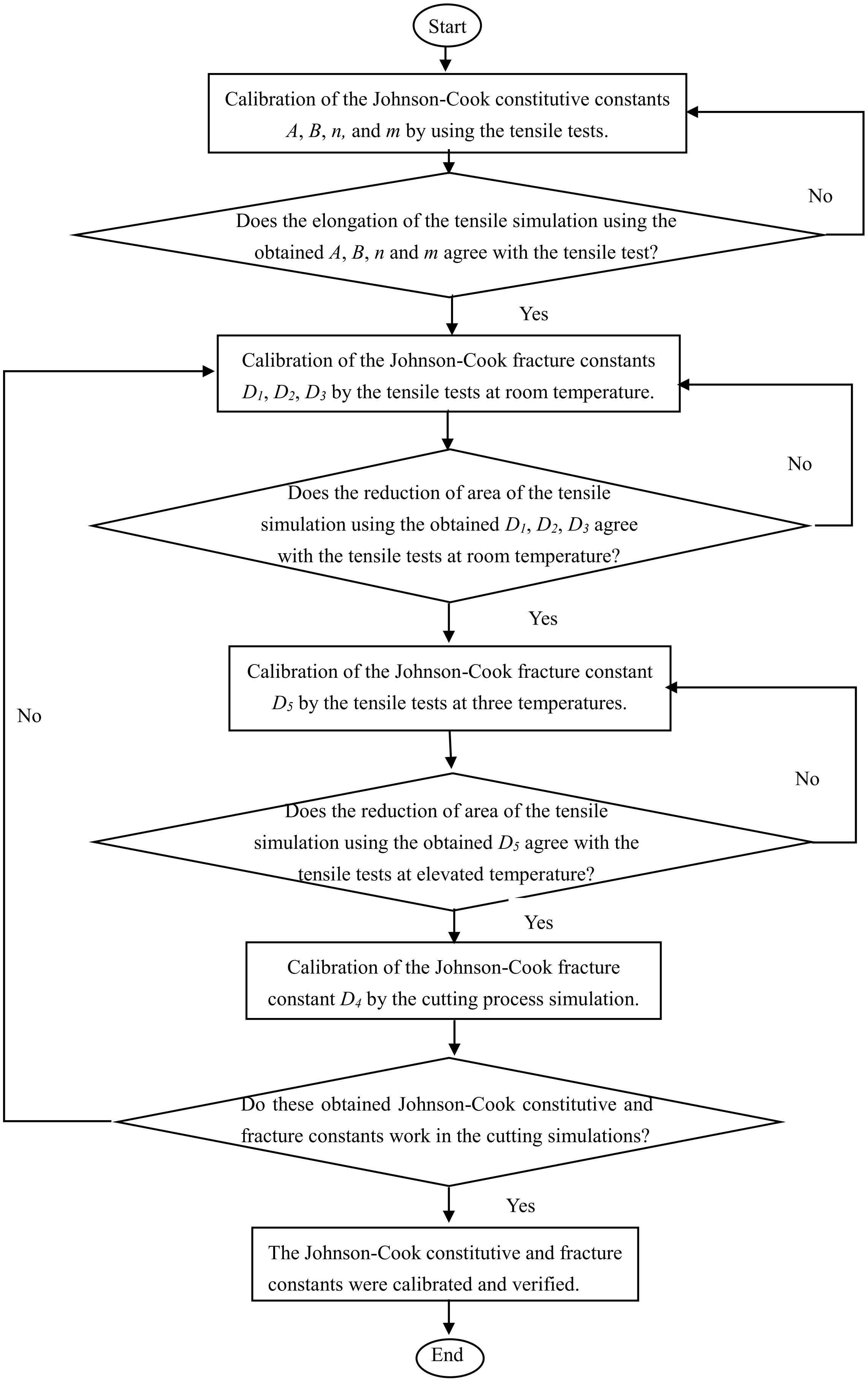
Start
Calibration of the Johnson-Cook constitutive constants A, B, n, and m by using the tensile tests.
Does the elongation of the tensile simulation using the obtained A, B, n and m agree with the tensile test?
No
Yes
Calibration of the Johnson-Cook fracture constants D_1, D_2, D_3 by the tensile tests at room temperature.
Does the reduction of area of the tensile simulation using the obtained D_1, D_2, D_3 agree with the tensile tests at room temperature?
No
Yes
Calibration of the Johnson-Cook fracture constant D_5 by the tensile tests at three temperatures.
Does the reduction of area of the tensile simulation using the obtained D_5 agree with the tensile tests at elevated temperature?
No
Yes
Calibration of the Johnson-Cook fracture constant D_4 by the cutting process simulation.
Do these obtained Johnson-Cook constitutive and fracture constants work in the cutting simulations?
No
Yes
The Johnson-Cook constitutive and fracture constants were calibrated and verified.
End

5.3 Calibration and Verification of the Johnson-Cook Constitutive Constants

The constants of Johnson-Cook constitutive model for the material are unique. These constants can be different for the same materials with different heat treatments. Hence, the constants of the material used in this research should be determined first. The Johnson-Cook constitutive model is shown in Equation (4.1). In the Johnson-Cook constitutive equation, there are three brackets which express the strain effect with *A, B, n*, the strain rate effect with *C*, and the temperature effect with *m*. In this research, calibrated constants of the Johnson-Cook constitutive model are obtained from uniaxial tensile test configurations. To verify the constants of the Johnson-Cook constitutive model, the comparison of the deformation and elongation is made between the simulations and experiments.

5.3.1 Calibration and Verification of the Constants **A, B, n** *of the Johnson-Cook Strain Hardening Component*

The Johnson-Cook hardening term is shown in Equation (5.1), where $\dot{\varepsilon}^* = 1.0$ and $T^* = 0$ of room temperature.

$$\sigma = \mathrm{A} + \mathrm{B}\varepsilon^{n} \tag{5.1}$$

To obtain the constants A, B, and n, stress-strain data are acquired from tension test with the un-notched specimen at room temperature. The equivalent tension stresses are computed by using the Bridgman correction factor as shown in Equation (3.1) [Bridgman, 1952]. The diameter of the central cross section d is computed using

Equation (5.2), where the local strain map of the central point in the specimen acquired from the ARAMIS system is shown in Figure 5.3.

$$\mathrm{d} = \frac{d_0}{2.718^{\frac{\varepsilon_{axial}}{2}}} \tag{5.2}$$

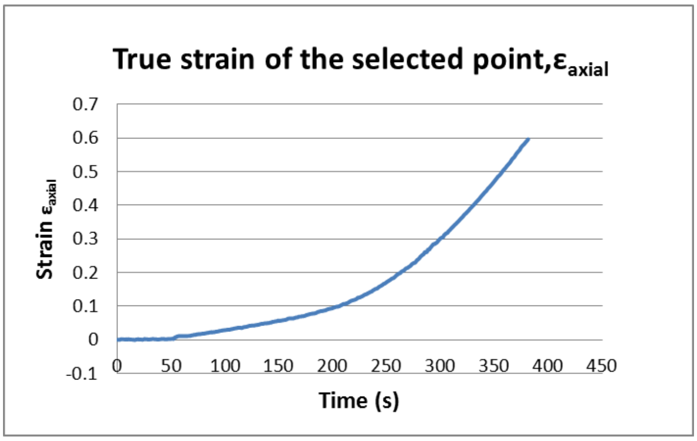

(a)

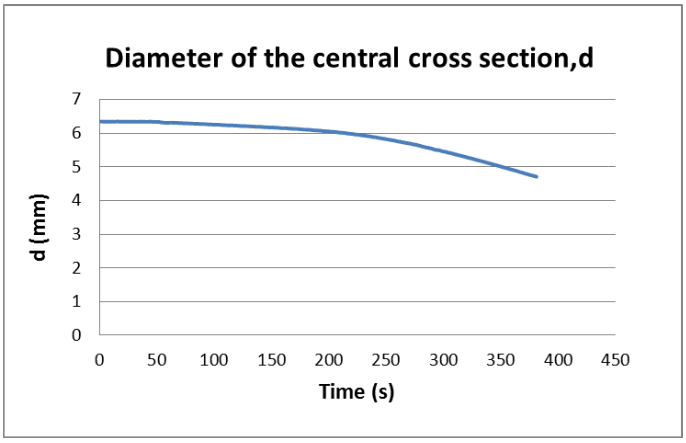

(b)

Figure 5.3: (a) The strain of the central point of the specimen from ARAMIS; (b) *d* calculated from the strain map from (a).

The radius of curvature of the profile of the neck is *R* calculated using Equation (5.3). The length of the chord, 2*b*, is measured as the length of the necking region (Line 1) in the 2D strain map from ARAMIS report. The arrow height, $\mathrm{h} = \frac{(D_0 - d)}{2}$, is calculated from the original diameter of the cross section of the specimen, D_0, and *d* as shown in Figure 5.3. Figure 5.4 shows the data 2*b*, *h*, and *R* during the experiment.

$$R = \frac{b^2+h^2}{2h} \tag{5.3}$$

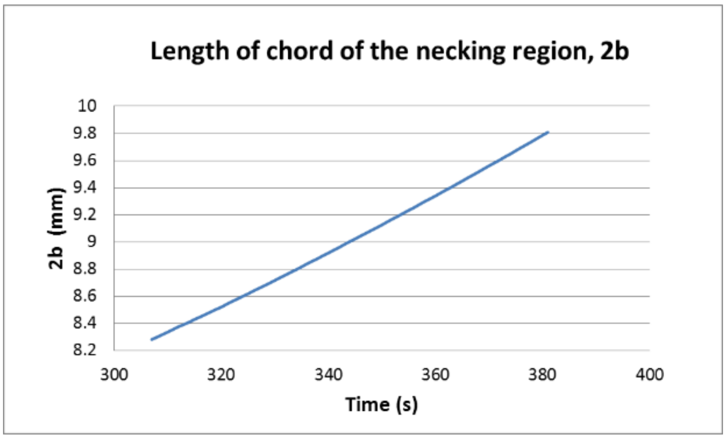

(a)

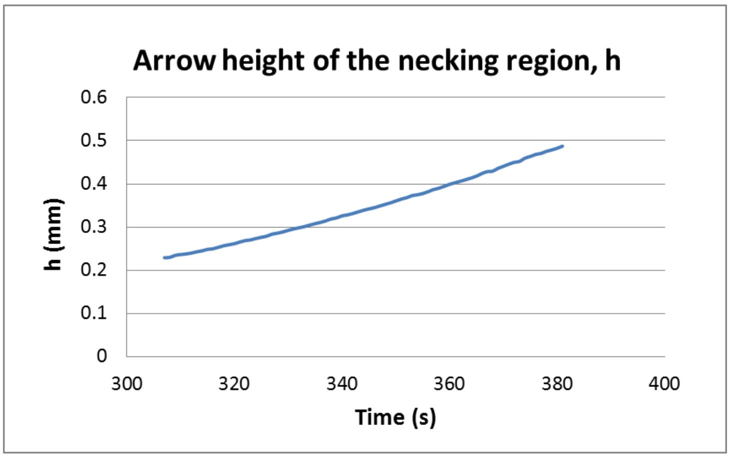

(b)

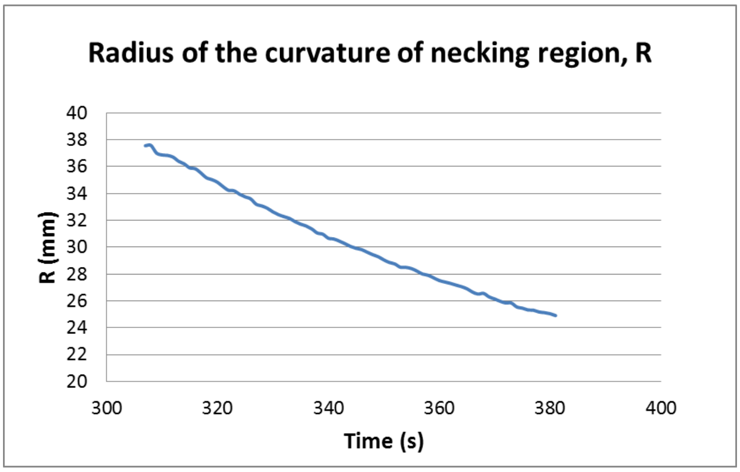

(c)

Figure 5.4: (a) Length of the chord of the necking region 2b; (b) The arrow height of the necking region h; (c) Radius of the curvature of the necking region R.

Then, the true stress, σ_a, and the stress corrected with the Bridgman correction factor [Bridgman, 1952], σ_{effect}, are computed from the ARAMIS report using Equation (3.1), as shown in Figure 5.5, which showed the true stress and the Bridgman corrected effective stress.

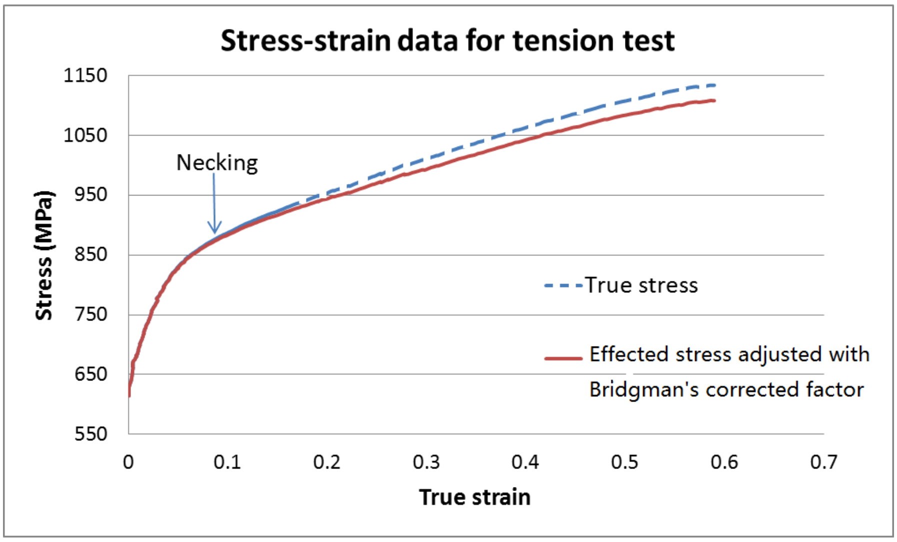

Figure 5.5: Comparison of stress-strain data for the tension test and the data adjusted by the Bridgman correction factor.

Firstly, the constants of Equation (5.1) in the Johnson-Cook constitutive model are computed depending on the stress-strain data with the Bridgman correction factor, as shown in Figure 5.5. *A* is the yield stress; *B* and *n* are obtained depending on the strain hardening curve by using a sum of squares. The comparison of the experimental stress-strain data and the calibrated results of the Johnson-Cook constitutive model are shown in Figure 5.6.

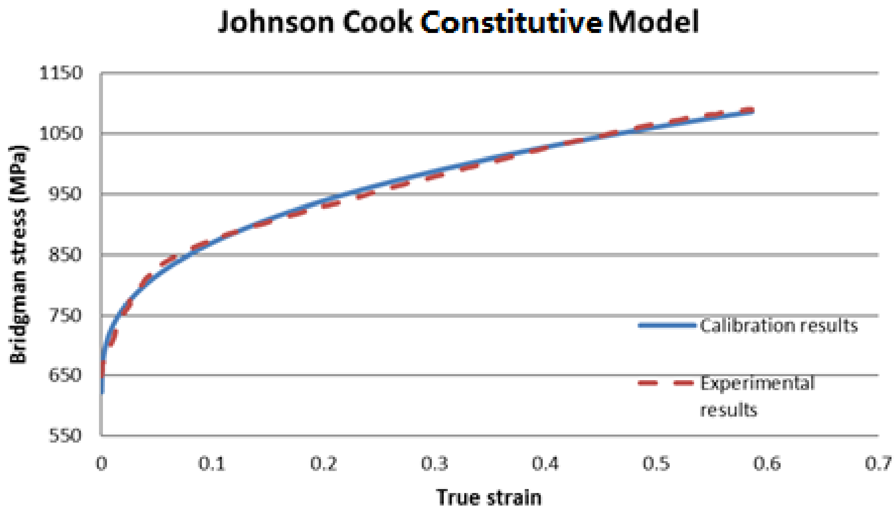

Figure 5.6: Comparison of the experimental data and the calibrated results of the Johnson-Cook constitutive model.

The constants of the Johnson-Cook constitutive model of the material for tension test are shown in Table 5.2.

Table 5.2: Calibrated constants of the Johnson-Cook constitutive model for the strain from tension tests.

A (MPa)	B (MPa)	n (-)
614.2	599.4	0.36

These constants are obtained by using the stress from the tensile tests for $\dot{\varepsilon}^* = 0.000484$, and constants *A*, *B*, and *n* must be adjusted for $\dot{\varepsilon}^* = 1.0$ using Equation (5.4).

$$\kappa = 1 + \mathrm{C}\ln\dot{\varepsilon}^* \tag{5.4}$$

Hence, the stress of the tensile test can be expressed using Equation (5.5).

$$\sigma = \mathrm{A} + \mathrm{B}\varepsilon^{n} = (A_{true} + B_{true}\varepsilon^{n_{true}}) \times \kappa \tag{5.5}$$

where *A, B, n* are the constants obtained from the tensile test, while A_{true}, B_{true}, n_{true} are the actual true constants that were adjusted by using κ value. Hence, the real constants of the Johnson-Cook constitutive model are expressed using Equation (5.6).

$$A_{true} = \frac{A}{\kappa}\ ,\ B_{true} = \frac{B}{\kappa},\ n_{true} = n \tag{5.6}$$

The value of κ is calculated by Equation (5.4), where C=0.0134 from Jaspers [2002], $\dot{\varepsilon}^* = 0.000484$ from tensile test. So κ=0.8977, and A_{true}=684.2 MPa, B_{true}=667.7 MPa, that are calculated by Equation (5.6). Considering the shear stress flow of the material, the average flow stress of the tensile and torsion tests is used. Hence, the calibrated constants are the average constants adjusted by an assumed 10 percent difference by using the tension data. So assuming the adjusted variable is $\lambda = 0.9$, the average constants A_{ave}, B_{ave}, n_{ave} of the Johnson-Cook constitutive model is shown in Equation (5.7).

$$A_{ave} = A_{true} \times \lambda,\ B_{ave} = B_{true},\ n_{ave} = n_{true} + ln\lambda \tag{5.7}$$

Therefore, Table 5.3 shows the final results as the constants of the Johnson-Cook constitutive model for strain hardening.

Table 5.3: Adjusted constants of the Johnson-Cook constitutive model for strain hardening.

A_{ave} (MPa)	B_{ave} (MPa)	n_{ave} (-)
615.8	667.7	0.255

To verify the constants *A*, *B*, *n* in the Johnson-Cook constitutive model, a comparison of a tensile test and its simulation is used. The tensile test used is the test with pre-notch-radius of 9.525 mm specimen at room temperature and low strain rate. Figure 5.7 shows the comparison of the deformation between this experimental geometry by the camera and its computed geometry from strain contours of the simulation. Figure 5.7 shows the deformation of the specimen at the initial stage and the end of the test, respectively. The left parts of Figure 5.7(a) and 5.7(b) are the actual photos of the specimen from the experiment, and the right parts are from the simulation. The gage in red represents the experimental result, and the gage in green represents the computed result. The gage length and the reduction in the cross-sectional area were similar between both simulation and experiment. That result means the simulation agrees with the experimental result, which validates the constants A, B, n in the Johnson-Cook constitutive model.

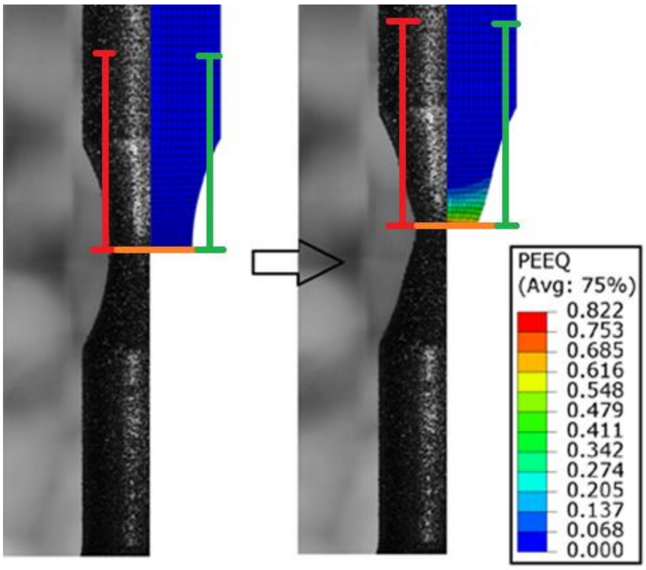

(a) **(b)**

Figure 5.7: Comparison of the elongation between tension tests with a notched radius as 9.525 mm specimen at room temperature and its simulation: (a) initial stage, (b) after fracture.

5.3.2 Calibration and Verification of the Constants m *of the Johnson-Cook Temperature Component*

The third bracket of Equation (3.1) respects the thermal effect on the stress. Assuming σ_0 is the stress with $\dot{\varepsilon}_0 = 1.0\ s^{-1}$ at room temperature $T^* = 0$, the Equation (3.1) could express using Equation (5.8).

$$\sigma = \sigma_0 \times [1 - T^{*m}] \tag{5.8}$$

A thermal softening fraction K_T is defined with Equation (5.9) and (5.10).

$$K_T = \frac{\text{yield stress at elevated temperature}}{\text{yield stress at room temperature}} = \frac{\sigma_y}{\sigma_{y0}} \tag{5.9}$$

$$K_T = 1 - T^{*m} \tag{5.10}$$

To obtain the constant m from Equation (5.10), the yield stress-dimensionless temperature data are considered from tension tests with un-notched specimens at three temperatures. The experimental data are shown in Table 5.4. As expressed in Equation (5.10), constant m is calculated with experimental data in Table 5.4 fitting the "least squares" method by using the solver analysis in Microsoft office Excel, and the value of m was found to be 1.078. The experimental data and the fitting line are shown in Figure 5.8.

Table 5.4: Yield stress and the thermal softening fraction of tension tests.

T^* (-)	σ_y (MPa)	K_T (-)
0	583.38	1
0.0943	533.52	0.915
0.1962	485.30	0.832

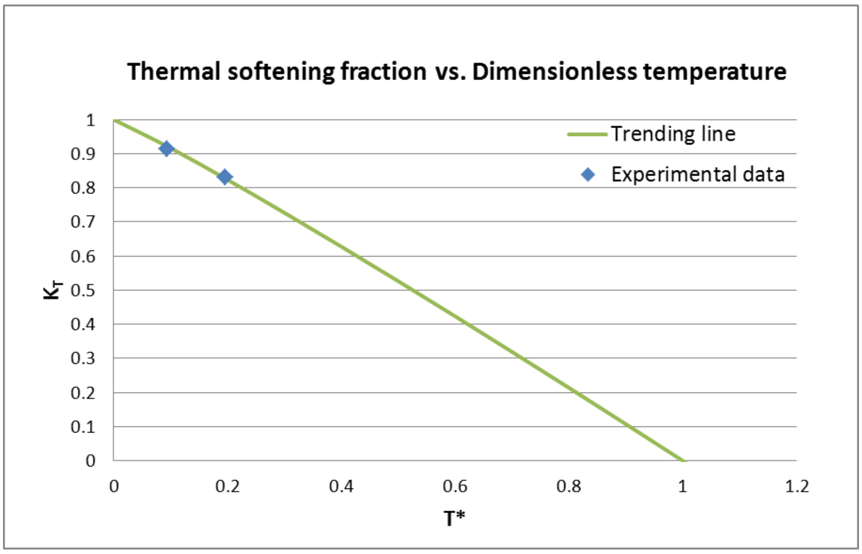

Figure 5.8: Plot of the thermal softening fraction vs. dimensionless temperature.

To verify the constants m in the Johnson-Cook constitutive model, the tension test with un-notched specimens at 150˚C and 285˚C was carried out and compared with the simulation with the exact conditions. Figure 5.9 (a) and (b) show the comparison between experiment and simulated results with tests carried out at 150˚C and 285˚C respectively. The gage length and the reduction in the cross-sectional area were similar to both experiment and simulation. Therefore, the m constant is valid.

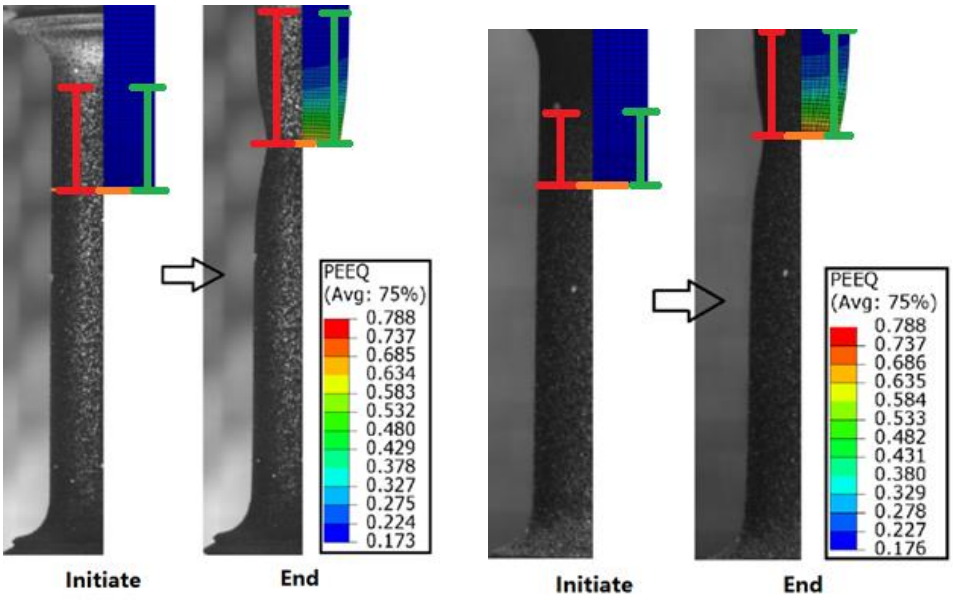

(a) **(b)**

Figure 5.9: Comparison of the elongation between tension tests with un-notched specimens and their simulations: (a) at 150˚C; (b) at 285˚C.

Figure 5.10 shows the experimental plastic behavior of the AISI 1045 steel performed in this research and compared with the plasticity constants acquired by Borkovec [2008] and Jaspers and Dautzenberg [2002]. The experimental plastic behavior was carried out at room temperature and at a low strain rate. The Jaspers and Dautzenberg [2002] constants agreed better with the experimental results when compared to Borkovec’s [2008] constants. Therefore, this result shows that it is valid to apply the Jasper and Dautzenberg [2002] constitutive constant to the current research.

Table 5.5 shows the calibrated constants acquired from the experimental stress-strain curve.

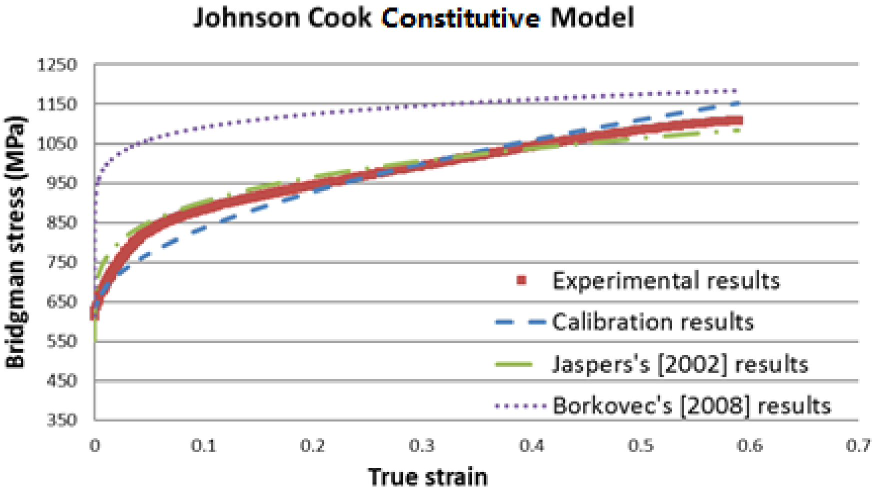

Figure 5.10: Comparison of the Johnson-Cook constitutive curves between the experimental results, the calibrated results and the results from Jaspers and Dautzenberg [2002]and Borkovec [2008].

Table 5.5: Calibrated constants of the Johnson-Cook constitutive models from tension tests.

Constants of the Johnson-Cook constitutive model	A (MPa)	B (MPa)	C (-)	n (-)	m (-)
Calibration results	615.8	667.7	0.0134	0.255	1.078

5.4 Calibration and Verification of the Johnson-Cook Fracture Constants

Since there are three brackets in the Johnson-Cook fracture formula, Equation (4.2), that expresses the stress triaxiality effect with D_1, D_2, D_3, the stress rate effect with D_4, and the temperature effect with D_5, the calibration, and verification of these constants are conducted respectively. To verify the Johnson-Cook fracture constants, the comparison of the deformation and reductions of areas is made between the simulations and experiments carried out under tension configuration.

5.4.1 *Calibration and Verification of the Johnson-Cook Fracture Constants* **D_1, D_2, D_3**

First, the effect of the stress triaxiality is considered. When $\dot{\varepsilon}^* = 1.0$ and $T^* = 0$, the strain at fracture expressed with the Johnson-Cook fracture model is shown in Equation (5.11).

$$\varepsilon^f = D_1 + D_2 \exp D_3 \sigma^* \tag{5.11}$$

where ε^f, as the strain at fracture, is computed from the area of original central cross section of specimen A_0 and the area of central cross section of specimen after fracture A_f, as shown in Equation (5.12).

$$\varepsilon^f = \ln\left(\frac{A_0}{A_f}\right) = 2\ln\left(\frac{d_0}{d_f}\right) \tag{5.12}$$

The diameters of the minimum central cross sections were measured using a microscope. Figure 5.11 showed the measurements of the original size of the specimens from the tension tests with one un-notched and four different notched specimens under room temperature conditions.

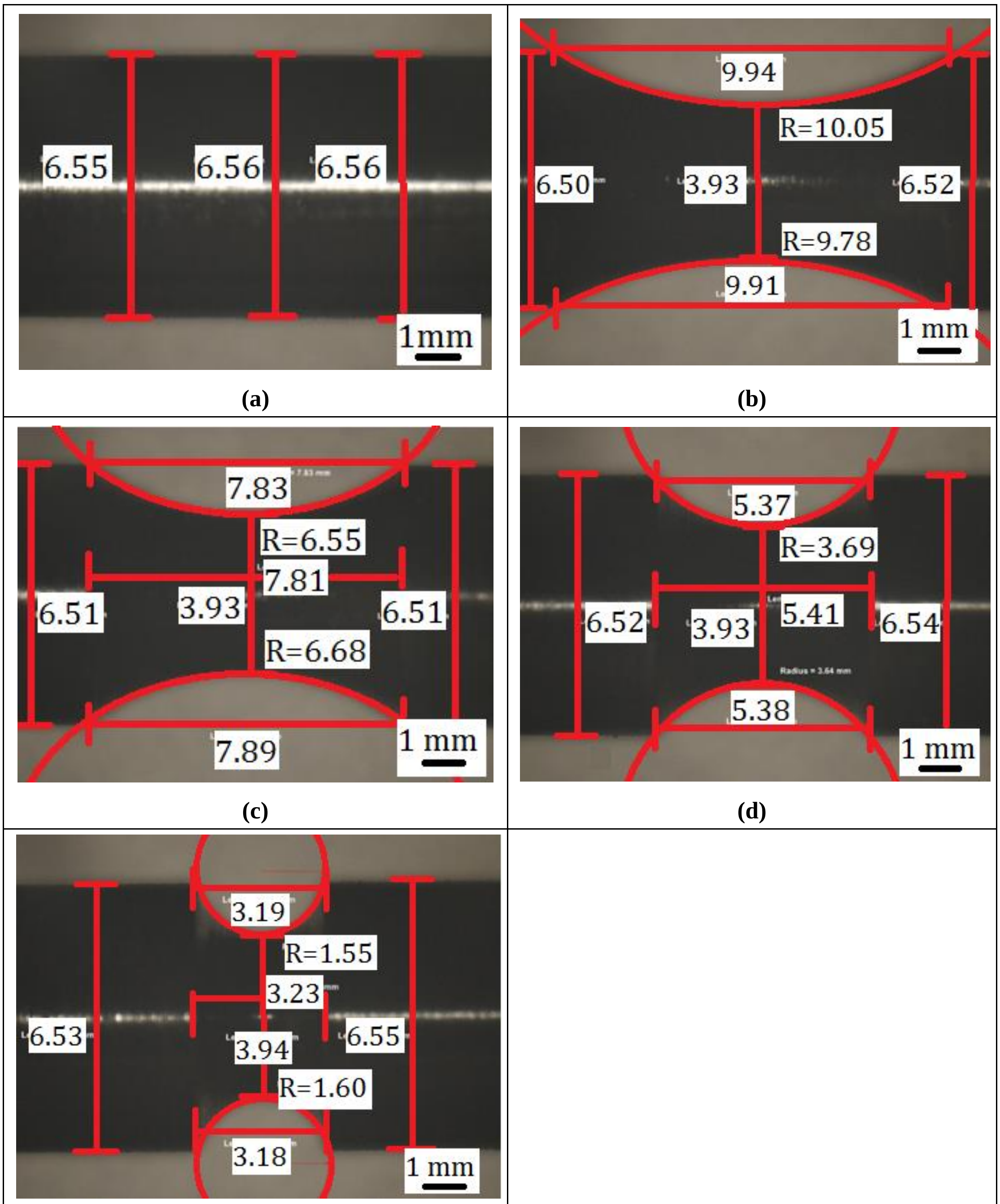

(a)

(b)

(c)

(d)

(e)

Figure 5.11: The measurements of the geometry of the original specimens of all kinds of specimens. (mm) (a) Un-notched specimen; (b) R=9.525(mm) pre-notched specimen; (c) R=6.35(mm) pre-notched specimen; (d) R=3.175(mm) pre-notched specimen; (e) R=1.5875(mm) pre-notched specimen; where R is the radius of the curvature of the notch.

After tensile specimens were fractured, the parts of the specimens are matched back and measured by using a microscope. Figure 5.12 shows the measurements of the geometry of all five kinds of the specimen after tension tests under room temperature.

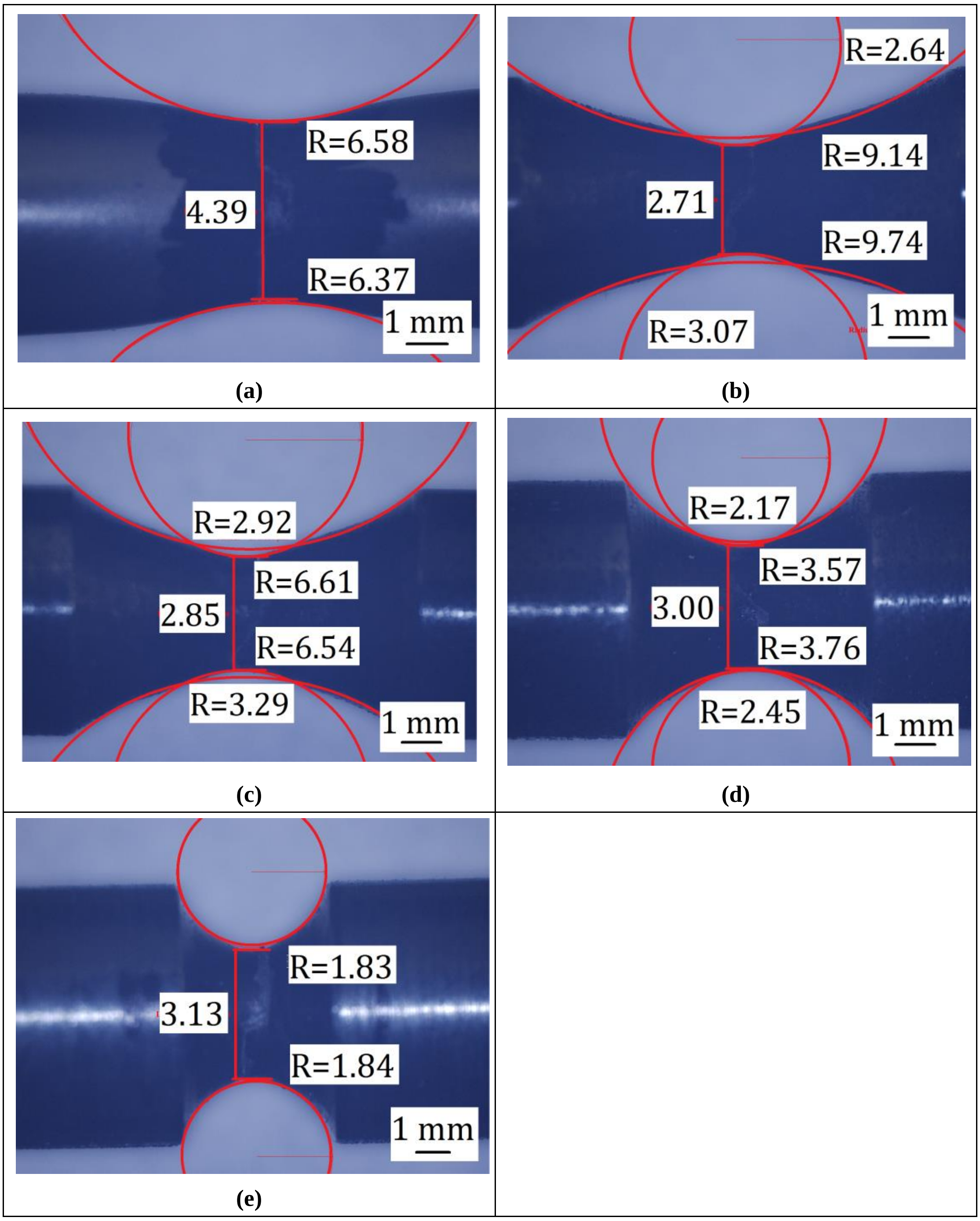

(a) **(b)** **(c)** **(d)** **(e)**

Figure 5.12: The measurements of all kinds of the specimen after fracture. (mm)
(a) Un-notched specimen; (b) R=9.525(mm) pre-notched specimen; (c) R=6.35(mm) pre-notched specimen; (d) R=3.175(mm) pre-notched specimen; (e) R=1.5875(mm) pre-notched specimen; where R is the radius of the curvature of the notch.

To get D_1, D_2, D_3 of the Johnson-Cook failure model, both of the stress triaxialities for the original specimens, η_0, and the specimens fracture after tension tests, η_f, are required. All these stress triaxialities are computed depending on the measurements by using a microscope as shown in Figure 5.13 and 5.14. The experimental data of ε^f, η_0, and η_f are shown in Table 5.6.

Table 5.6: Strain to fracture and the stress triaxiality of all five kinds of tensile specimens. (Dimensions of different types of specimens shown in Table 3.2)

Type of specimen	Strain at fracture, ε^f	Original stress triaxiality, η_0	Fracture Stress triaxiality, η_f
Un-notched	0.69	0.33	0.50
Un-notched	0.66	0.33	0.50
Notched 1 R_0=9.525mm	0.66	0.43	0.41
Notched 2 R_0=6.35mm	0.50	0.47	0.44
Notched 3 R_0=3.175mm	0.45	0.57	0.53
Notched 4 R_0=1.5875mm	0.39	0.82	0.70

Figure 5.13 shows the results of the experimental data used for the Johnson-Cook failure model, and the calibrated curve of the Johnson-Cook failure model fitted the "least squares" method. The calibrated curve was obtained by using the solver analysis in Microsoft office Excel. Table 5.7 shows the D_1, D_2, D_3 values.

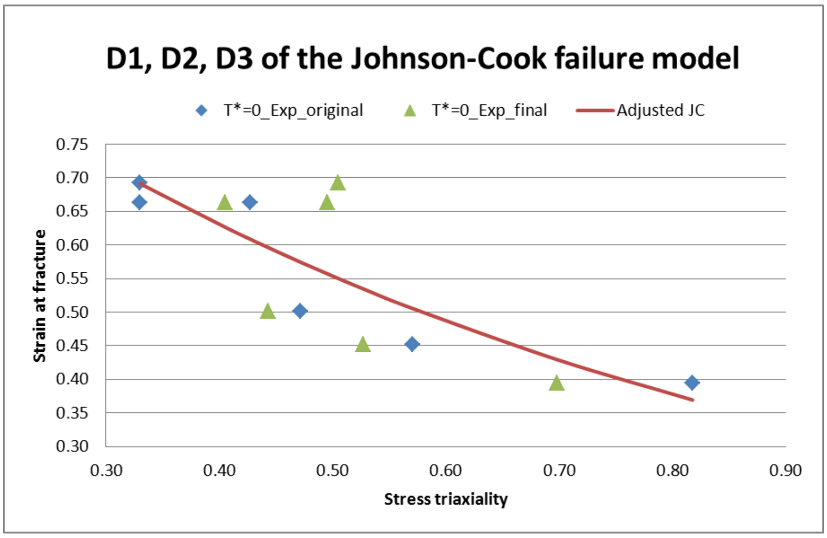

Figure 5.13: Experimental stress triaxiality vs. strain at fracture and the calibrated Johnson-Cook failure model.

Table 5.7: Calibrated D_1, D_2, and D_3 values.

D1	D2	D3
0.04	1.03	-1.39

To verify the constants D_1, D_2, D_3 of the Johnson-Cook failure formula, the tension test with un-notched and four different notched specimens at room temperature and corresponding simulations are used to compare with experimental results. Figure 5.14 shows the comparison between the deformation geometries acquired from experiments and simulations. Figure 5.14 shows the deformations of these specimens after fracture of these tensile processes. The left column of the Figure 5.14 shows the actual photos of the specimen from the experiment, and the right column is from the simulation. Comparing with the length of the radius of the cross section of the fracture surface, the results are almost the same. That means the simulation agrees with the experimental result, which validates the constants D_1, D_2, D_3 in the Johnson-Cook failure model.

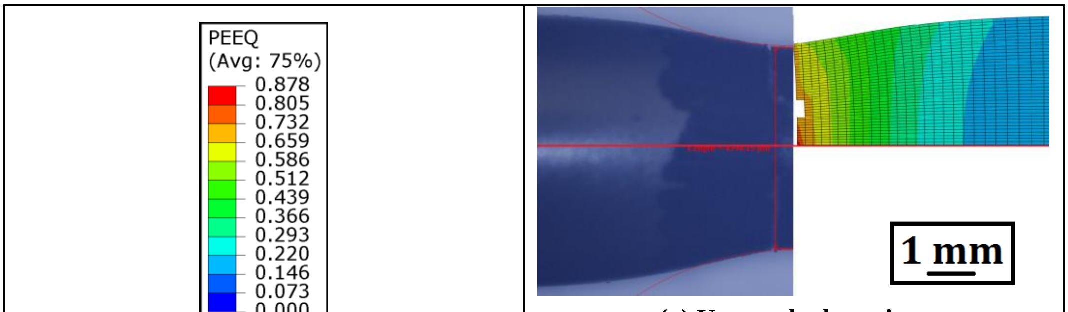

(a) Un-notched specimen

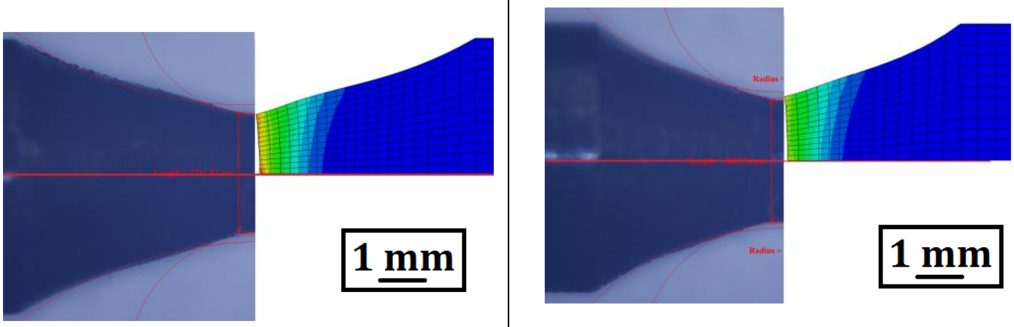

(b) Specimen with notch 1 (*R₀*=9.525mm) **(c) Specimen with notch 2 (*R₀*=6.35mm)**

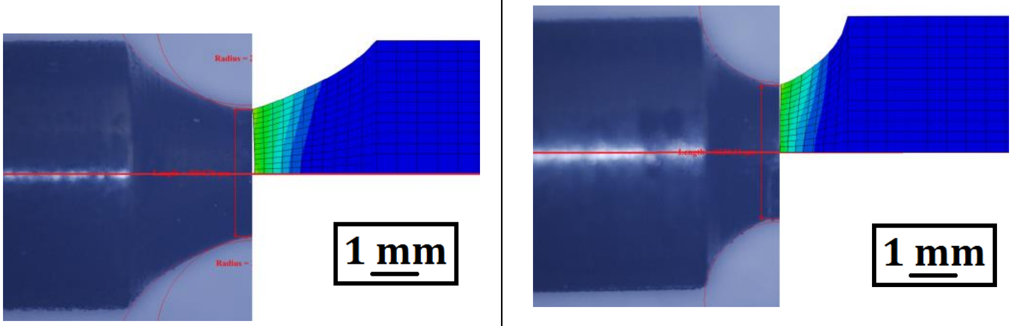

(d) Specimen with notch 3 (*R₀*=3.175mm) **(e) Specimen with notch 4 (*R₀*=1.5875mm)**

Figure 5.14: Comparison of the deformation and the radius of the cross section area between tension tests at room temperature with their simulations.

Additionally, the reduction areas of the tension tests at room temperature and the corresponding simulations are compared, as shown in Table 5.8. RA_e (%) means the reduction areas from the tension tests, and RA_m (%) is the one from the simulations. Errors (%) $= \frac{RA_m - RA_e}{RA_e} \times 100\%$, the errors of the models, are all smaller than $\pm 5\,\%$. That means the models are in good agreement with the tension tests, and the constants D_1, D_2, D_3 of the Johnson-Cook fracture model were valid.

Table 5.8: Comparison of the experimental and modelling reduction of areas of tension tests at 25°C.

Specimen Type	Un-notched	Notched 1 R_0=9.525mm	Notched 2 R_0=6.35mm	Notched 3 R_0=3.175mm	Notched 4 R_0=1.5875mm
RA_e (%)	48.5	48.5	39.4	36.4	32.6
RA_m (%)	47.2	46.5	40.0	37.2	32.1
Errors (%)	-2.7	-4.1	1.5	2.3	-1.6

5.4.2 Calibration and Verification of the Johnson-Cook Fracture Constant D_5

Considering the effect of the temperature on the strain at fracture, we assume a strain at fracture defined at $\dot{\varepsilon}^* = 1.0$ and $\mathrm{T}^* = 0$,$\varepsilon_0^{\mathrm{f}}$, and the used strain rate is also $\dot{\varepsilon}^* = 1.0$. Then the strain at fracture expressed in Johnson-Cook failure model is shown in Equation (5.13)

$$\varepsilon^{\mathrm{f}} = \varepsilon_0^{\mathrm{f}} \times [1 + \mathrm{D}_5 \mathrm{T}^*] \tag{5.13}$$

where T^* is the dimensionless temperature. To get the Johnson-Cook fracture constant D_5, the Equation (5.13) could be changed to Equation (5.14).

$$\mathrm{D}_5 = \frac{\frac{\varepsilon^{\mathrm{f}}}{\varepsilon_0^{\mathrm{f}}} - 1}{\mathrm{T}^*} \tag{5.14}$$

where the ratio is $\frac{\varepsilon^{\mathrm{f}}}{\varepsilon_0^{\mathrm{f}}} = \frac{\text{Fracture strain } at\ T^* \geq 0, \dot{\varepsilon} = 1.0}{\text{Fracture strain } at\ T^* = 0, \dot{\varepsilon} = 1.0}$. The fracture stain from a tension test with a un-notched specimen at room temperature is assumed as ε_0^f. As the temperature increases along the tension test process, T^* in Equation (5.14) is assumed as the average temperature of this process. Hence, the temperature used is expressed as shown in Equation (5.15)

$$T^* = T_{avg}^* = \frac{T_0^* + T_f^*}{2} \tag{5.15}$$

The original temperature, T_0^*, is set prior to the tensile loading surrounding the specimen in an oven. The fracture temperature, T_f^*, are computed using Equation (5.16) changed from Equation (5.10) as shown in the plot of thermal softening fraction vs. dimensionless temperature in Figure 5.8.

$$T_f^* = (1 - K_T)^{-m} \tag{5.16}$$

The experimental data needed in Equation (5.9) and (5.16) to compute T_f^* is in Table 5.9.

Table 5.9: Experimental data used to compute T_f^* and result T_f^*.

No.	Original Temperature, T₀ (C°)	Force, F (N)	Area, A (m^2)	Yield stress, σ_y (MPa)	Thermal softening fraction, K_T (-)	Fracture temperature, T_f^* (-)
1	25	19450.95	15.9	1223.33	1	0
2	25	19780.25	16.315	1212.40	0.991062412	0.0126
3	150	17657.6	16.08	1098.11	0.897639462	0.1207
4	150	18587.65	17.085	1087.95	0.889335871	0.1298
5	285	18930.3	17.075	1108.66	0.906260583	0.1113

The fracture strains from tension tests with un-notched specimens at three temperatures and the ratios of these fracture strains are used as shown in Table 5.10. The result of the No. 2 test is smaller than at original temperature, so this value is ignored and not used for obtaining D_5 value.

Table 5.10: The fracture strains used for obtaining D_5 of the Johnson-Cook failure model from tension test with un-notched specimens at three temperatures.

No.	Original temperature T_0 (C°)	Original temperature T_0^*	Fracture temperature T_f^*	Average temperature T_{avg}^*	Fracture strain ε^f	Ratio $\frac{\varepsilon^f}{\varepsilon_0^f}$
1	25	0	0	0	0.69	1.0455
2	25	0	0.0126	0.0063	0.66	1
3	150	0.0943	0.1207	0.1075	0.74	1.1212
4	150	0.0943	0.1298	0.1120	0.68	1.0303
5	285	0.1962	0.1113	0.1538	0.68	1.0303

The plot of the ratio of fracture strains and the dimensionless temperature is shown in Figure 5.15. The straight line in the plot fits the experimental results with the "least squares" method. The value of the slope of this line is D_5. Hence, $D_5 \approx 0.46$. Compared to the published D_5 value as shown in Table 5.1 (b), this data is smaller and more close to the value by Varizi [2010].

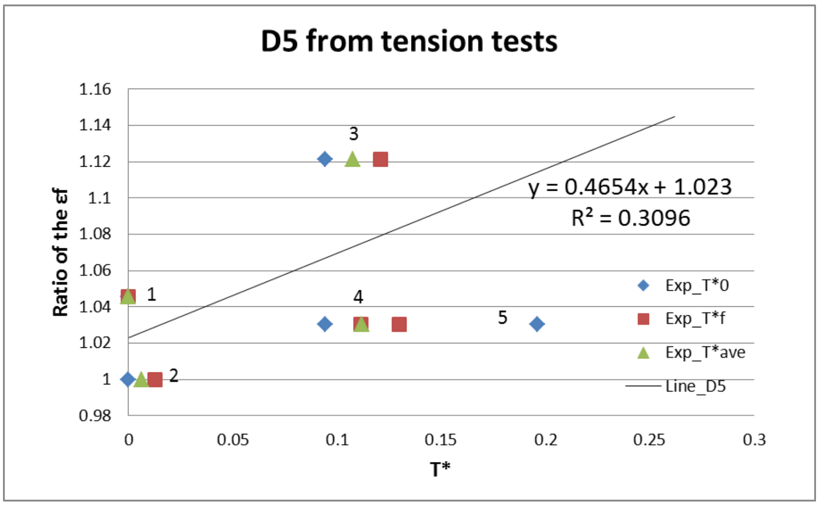

Figure 5.15: Plot of the ratio of fracture strain and dimensionless temperature.

To verify the constant D_5 of the Johnson-Cook failure formula, simulations were coming out at similar conditions with the experimental work with an operating temperature at 150ºC and 285ºC. The percentages of the elongation and the reduction in the area of these experiments were compared. Figure 5.16 and Figure 5.17 show the comparison of the deformation between these experimental geometries by the camera and its computed geometry from strain contours of the simulations, respectively at 150˚C and 285˚C. The length of the radius of the cross section after fracture of the experimental and modelling results are compared and was found to be similar. That finding means the simulation agreed with the experimental result, which validates the Johnson-Cook fracture constants D_5.

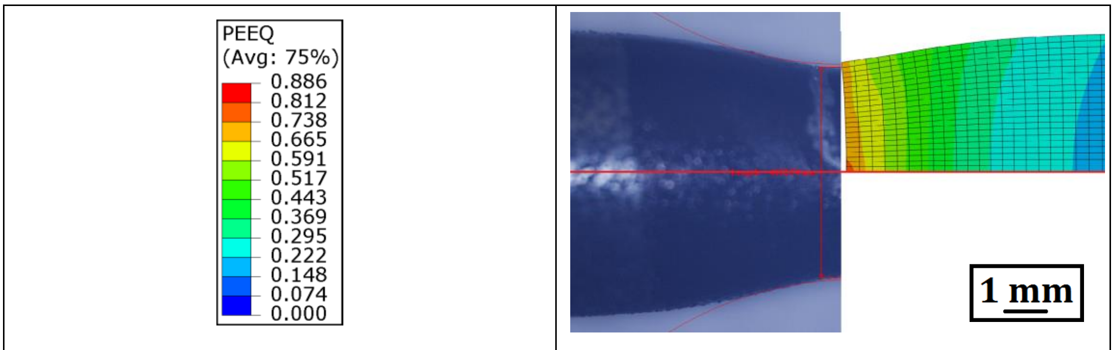

(a) Un-notched specimen

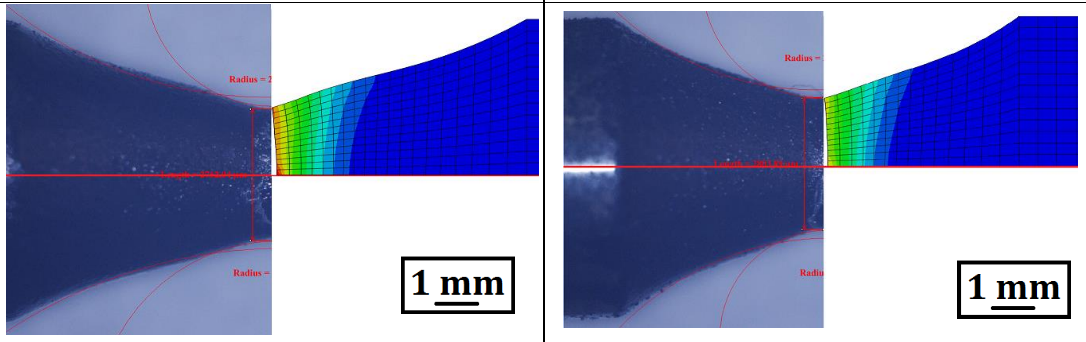

(b) Specimen with notch 1 (R_0=9.525mm) **(c) Specimen with notch 2 (R_0=6.35mm)**

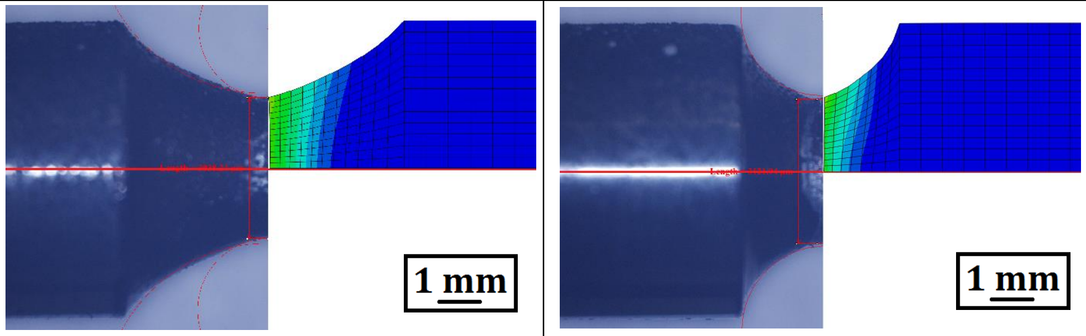

(d) Specimen with notch 3 (R_0=3.175mm) **(e) Specimen with notch 4 (R_0=1.5875mm)**

Figure 5.16: Comparison of the experimental and numerical views of the failure specimens at 150˚C.

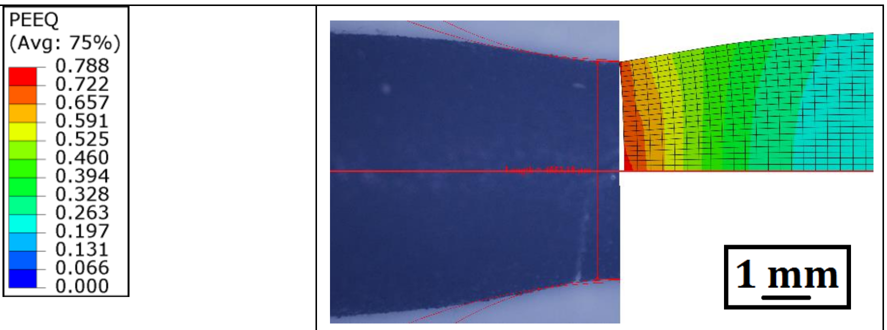

(a) Un-notched specimen

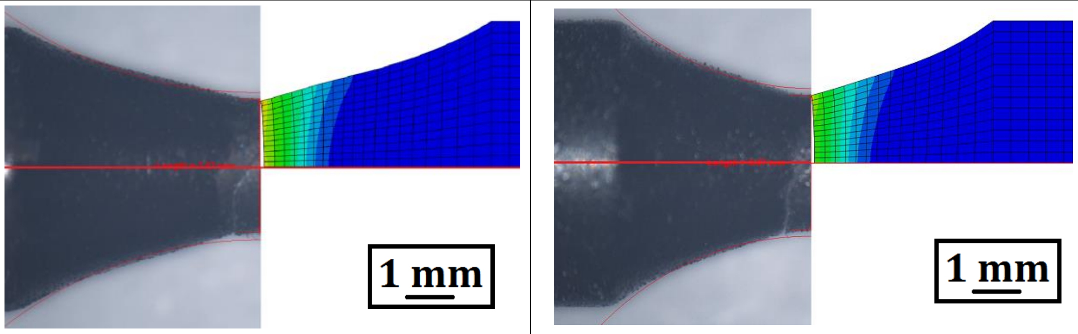

(b) Specimen with notch 1 (R_0=9.525mm)

(c) Specimen with notch 2 (R_0=6.35mm)

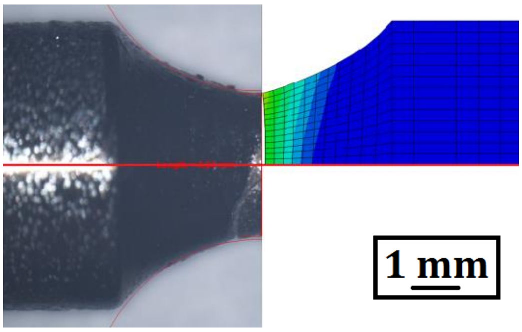

(d) Specimen with notch 3 (R_0=3.175mm)

Figure 5.17: Comparison of the experimental and numerical views of the failure specimens at 285˚C.

To prove the constant D_5 additionally, the reduction area from the tension tests at 150˚C and 285˚C and the corresponding simulations are compared as shown in Table 5.11. The errors between the experimental and modelling results are all in a small scale 2%, that further validate the D_5 constant.

Table 5.11: Comparison of the experimental and modelling reduction of areas.

(a) Temperature=150˚C

Type of the tensile specimen	Un-notched	Notched 1 R_0=9.525mm	Notched 2 R_0=6.35mm	Notched 3 R_0=3.175mm	Notched 4 R_0=1.5875mm
RA_e (%)	49.3	48.9	42.2	38.3	32.0
RA_m (%)	49.1	48.5	42.3	38.2	31.9
Errors (%)	-0.5	-0.8	0.2	-0.4	-0.3

(b) Temperature=285˚C

Type of the tensile specimen	Un-notched	Notched 1 R_0=9.525mm	Notched 2 R_0=6.35mm	Notched 3 R_0=3.175mm
RA_e (%)	49.5	40.4	35.7	33.4
RA_m (%)	49.6	40.1	36.3	33.5
Errors (%)	0.3	-0.7	1.8	0.3

5.4.3 Verification of the Calibrated the Johnson-Cook Fracture Constant D_4

The Johnson–Cook fracture constant D_4 relates to the effect of the strain rate on the fracture property. The D_4 value used here is 0.002 from Borkovec [2008]. A cutting simulation is employed to verify the D_4 value.

5.5 Evaluation of the Johnson-Cook Fracture Constants with Cutting Simulations

To validate the calibrated constants of the Johnson-Cook constitutive and failure models, the cutting process is simulated with three cutting-velocities and three feed-rates, as shown in Table 5.12.

Table 5.12: The cutting conditions used in FE simulations of cutting process.

Cutting velocity (m/min)	150	250	350
Feed rate (mm)	0.1	0.2	0.3

5.5.1 Chip Formation and Stress Contour

Figure 5.18 shows the von Misses stress contour maps around the cutting region at step 125/250 with three feed rates and three cutting velocities: 0.1 mm, 0.2 mm, 0.3 mm and 150 m/min, 250 m/min, 350 m/min. The continuous chips were observed for all the simulations. The shapes of the chips with the same velocity but different feed rates are compared, and the higher the feed rate is, the larger the chip curl radius, which agrees with results published by Reddy [2011].

The crack performance was checked by visual inspection. If the crack tip propagates ahead of the cutting edge, the Johnson-Cook fracture constant underestimated the actual fracture strain. However, when the crack tip is at the same location on the cutting edge, which is a function of time, then the Johnson-Cook fracture constant is accurately modelling the fracture strain as a function of hydrostatic pressure, temperature, and strain rate, which is the case in the results shown in Figure 5.18.

In addition, Figure 5.18 also shows the simulated von Mises stress contours during cutting. Maximum stresses were observed in the workpiece material at the cutting edge region. High stress magnitude was also observed in the primary shear zone and secondary deformation zone, and the high stress also supplies enough energy for the plastic deformations.

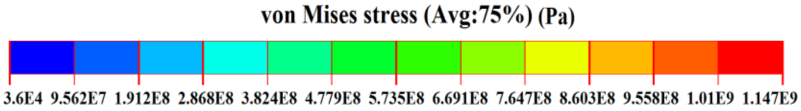

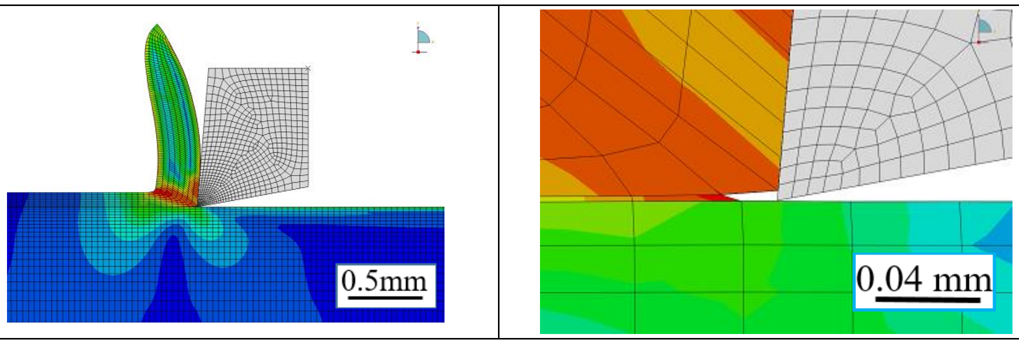

(a)f1 v1

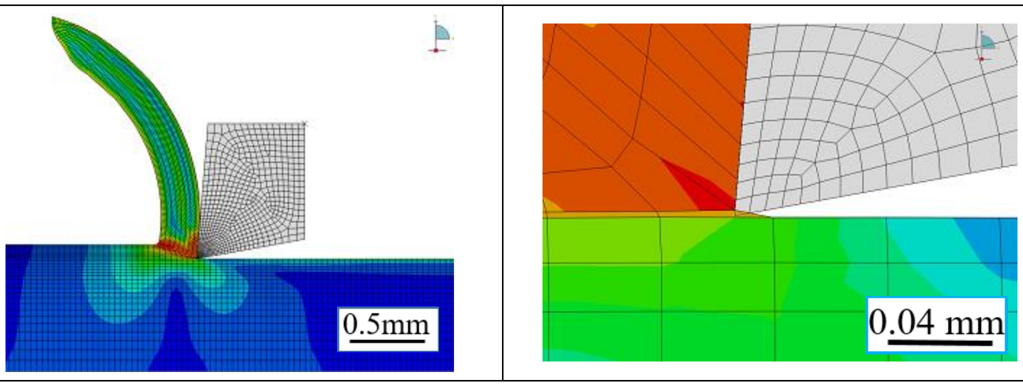

(b)f1 v2

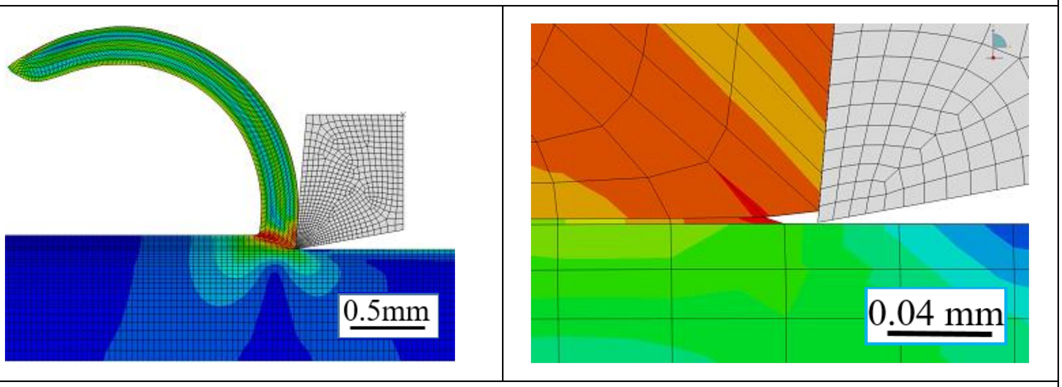

(c)f1 v3

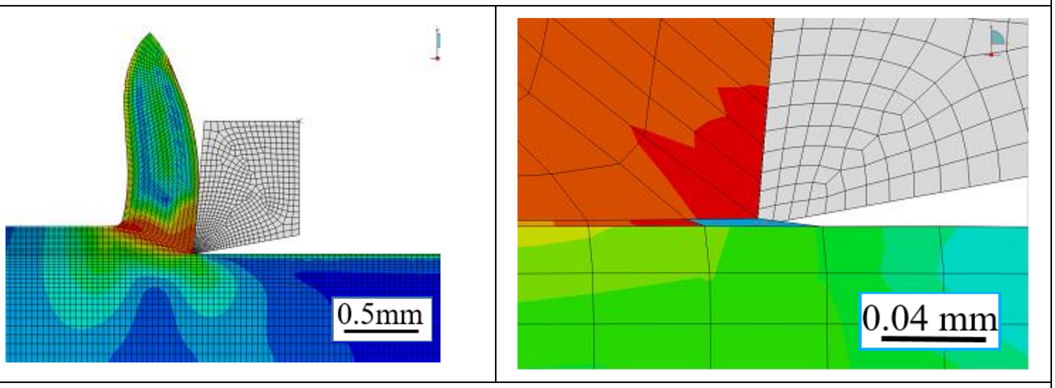

(d)f2 v1

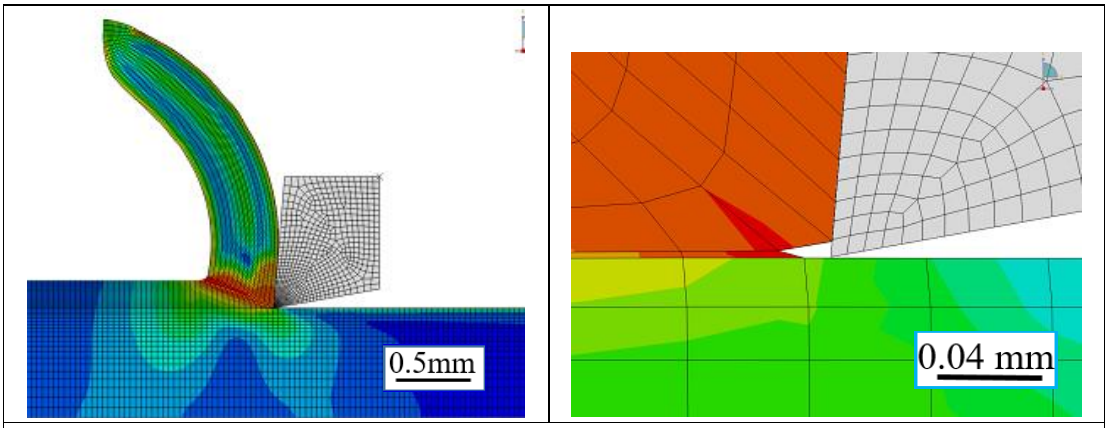

(e)f2 v2

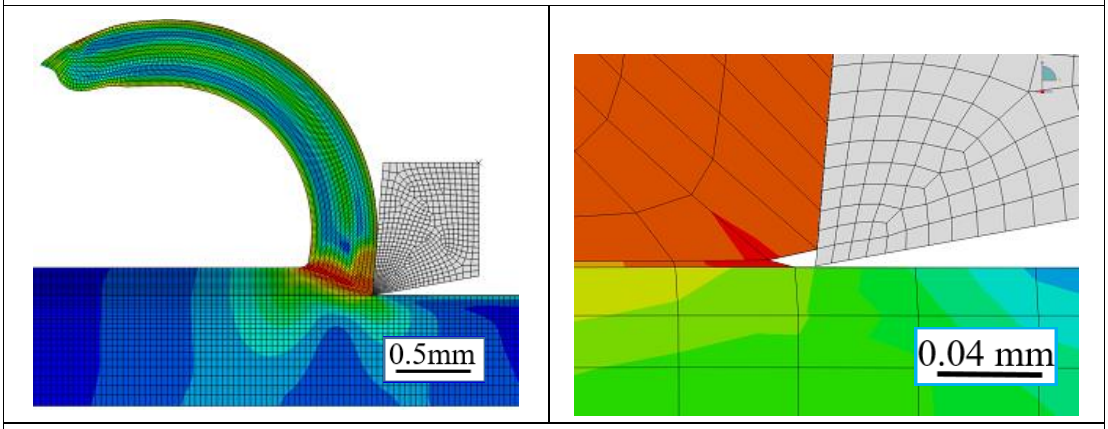

(f)f2 v3

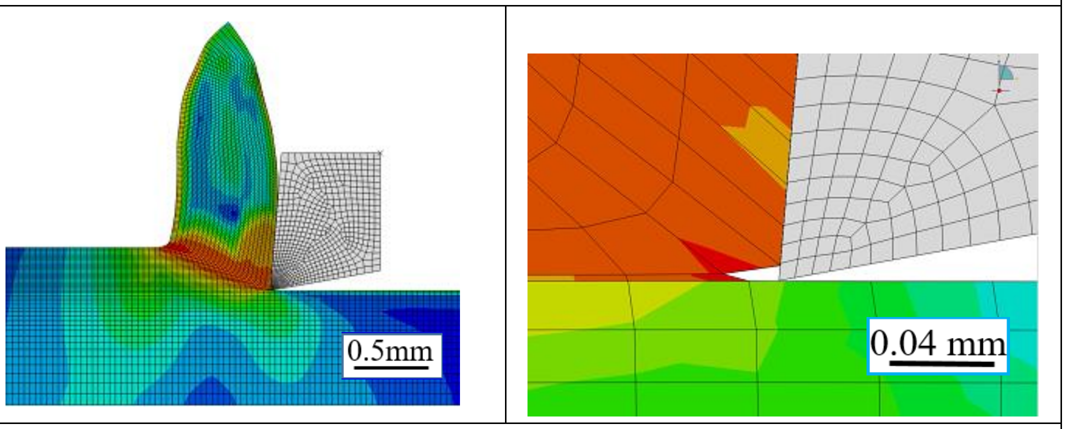

(g)f3 v1

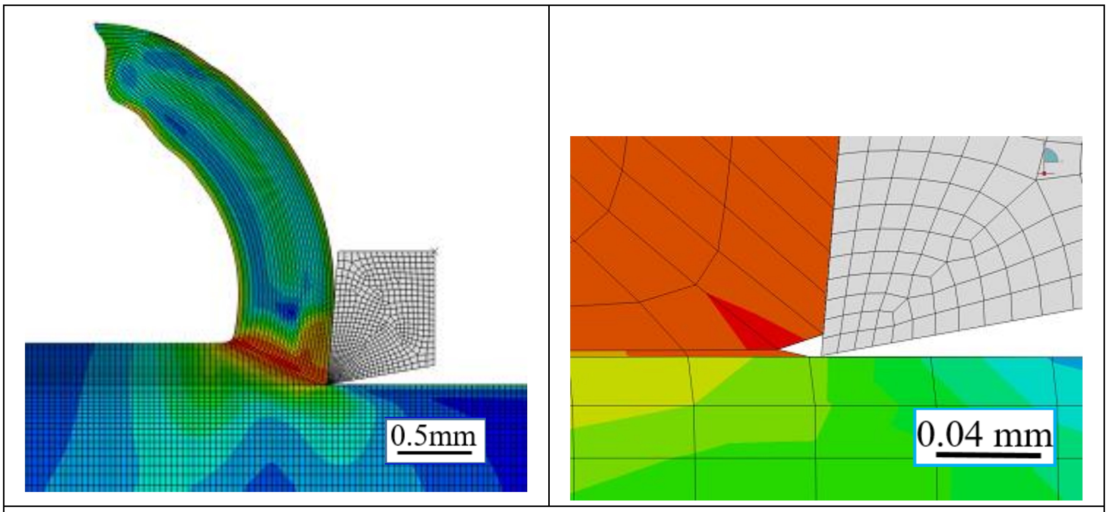

(h)f3 v2

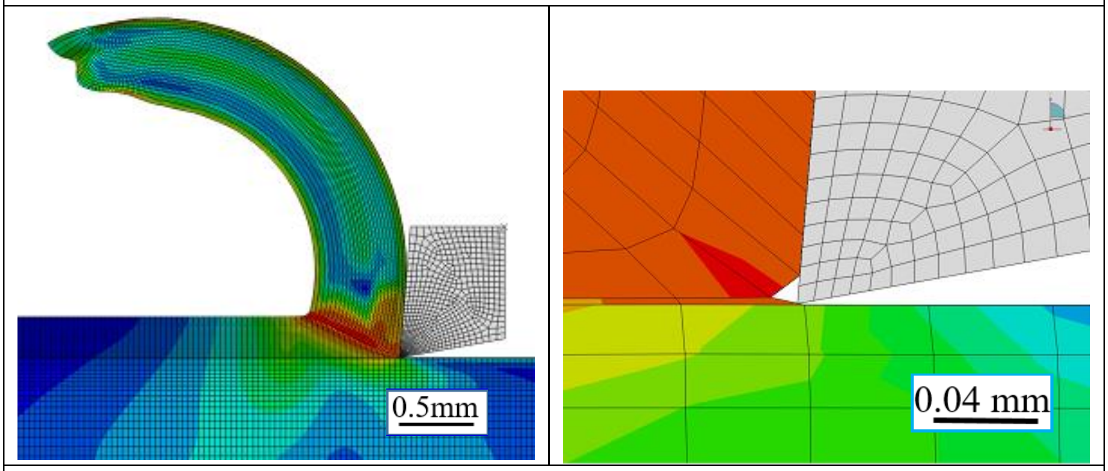

(i)f3 v3

Figure 5.18: von Misses stresses contour maps around the cutting layer of the cutting simulations at step 125/250: f1=0.1mm, f2=0.2mm, f3=0.3mm; v1=150m/min, v2=250m/min, v3=350m/min.

5.5.2 Temperature of the Tool-chip Interface

Figure 5.19 shows the temperature contour plots of all the cutting simulations. As shown in Figure 5.19, at the same feed rate, the temperature of the tool-chip interfaces increases when the cutting speed increases. This finding agreed well with experimental results, as a higher cutting speed offers more energy for heat generation [Dhar, 2007]. Also, at the same cutting speed, the temperature of the area where the tool contacted with the chip also increases as the feed rate increases. This phenomenon is because the volume of material to be removed increased, resulting in higher mechanical energy being converted to heat energy.

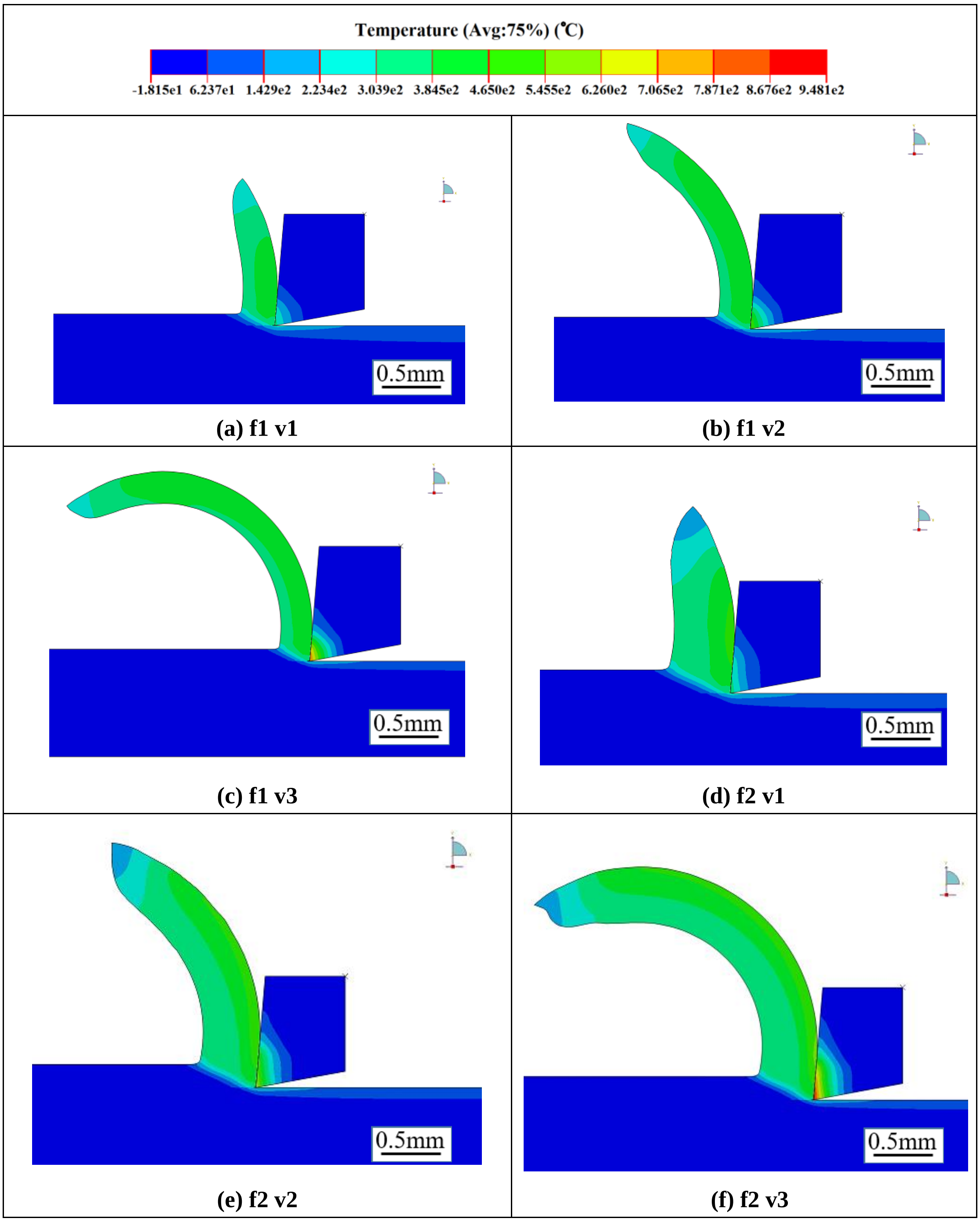

(a) f1 v1 **(b) f1 v2**

(c) f1 v3 **(d) f2 v1**

(e) f2 v2 **(f) f2 v3**

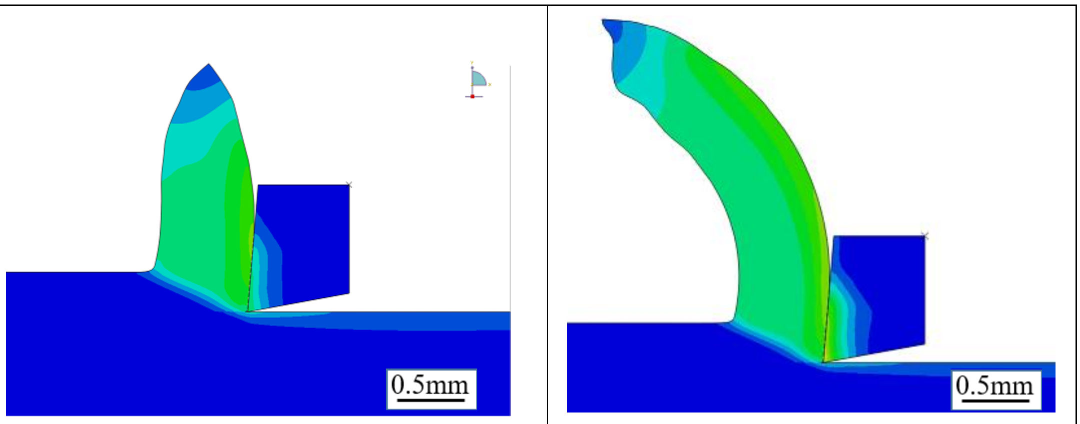

(g) f3 v1 **(h) f3 v2**

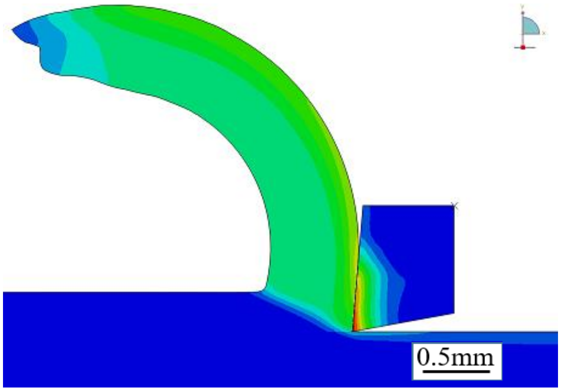

(i) f3 v3

Figure 5.19: Temperature contour maps of the cutting simulations: f1=0.1 mm, f2=0.2 mm, f3=0.3 mm; v1=150 m/min, v2=250 m/min, v3=350 m/min.

Additionally, to compare the temperatures of the tool-chip interface at different feeds and cutting speeds, a path along the tool-chip interface on both the chip surface and tool surface are set. Figure 5.20 shows an example of setting the paths of the tool-chip interface in the work piece in the model with a feed rate of 0.2 mm and a cutting speed of 250 m/min. Figure 5.21 shows the temperatures along the tool-chip interface in the work piece and in the tool with a feed rate of 0.2 mm and a cutting speed of 250 m/min. The temperature in the tool decreases from the cutting edge to the point where the chip separated from the tool along the tool-chip surface while the temperature trend was reversed in the chip. To compare the temperatures in the chip along the tool-chip interface with different feeds and the cutting speeds, the average temperatures are shown in Figure 5.22. The temperature increases as the feed rate increase at the same cutting speed. A similar trend was observed with increasing cutting speed and constant feed rate [Dhar, 2007]. Furthermore, the range shown in the Figure 5.22 is the oscillation of the temperature compared to the average data, and the oscillation increases as the feed rate and the cutting speed increases.

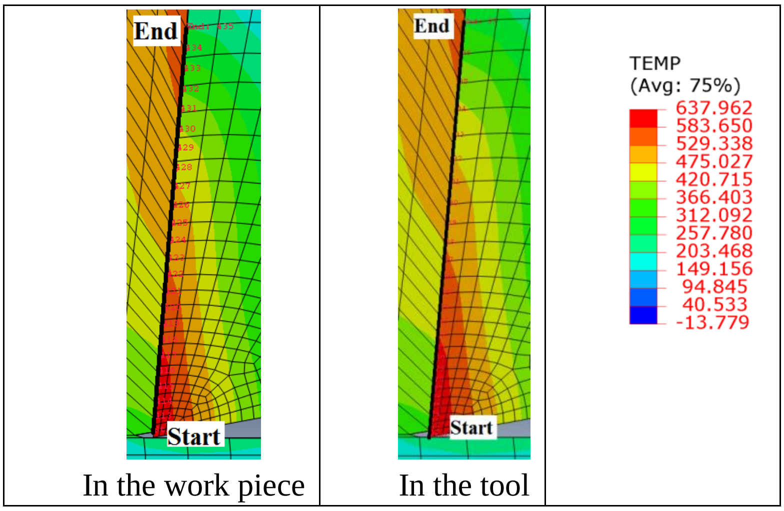

Figure 5.20: Paths used as the tool-chip interface in the work piece and in the tool.

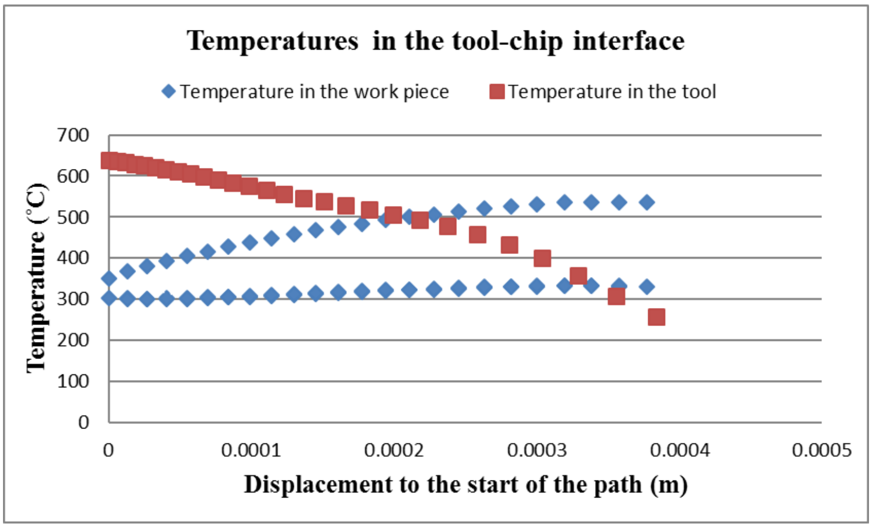

Figure 5.21: Temperatures along the tool-chip interface in the work piece and in the tool.

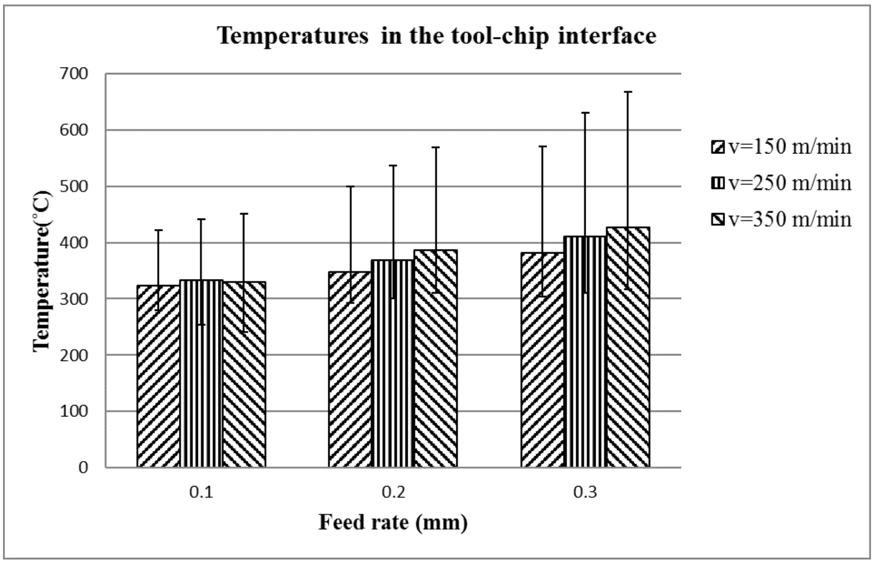

Figure 5.22: Comparison of the temperatures in the tool-chip interface with different feeds and cutting speeds.

5.5.3 Cutting Force

To consider the performance of the cutting simulations at three feed rates and velocities, the average cutting forces are compared. The cutting forces are obtained by adding up the forces of the nodes along the right vertical side of the tool as shown in Figure 5.23, and the results of the average cutting forces are shown in Figure 5.24. To compare with the same feed rate, the cutting forces decrease as the cutting speed increase. Moreover, compared to the same cutting speed, the cutting forces increase with the feed rate increase, as more energy is needed from the cutting forces to the thicker chip deformation. Besides, the range was shown in the Figure 5.24 to indicate that the oscillation of the cutting forces along the cutting progress, and that the oscillation is stronger as the cutting depth increases. The cutting force from a cutting experimental result from Hosseinkhani and Ng [2013] is also compared in Figure 5.24, and the cutting experimental conditions and results are shown in Table 5.13. The error, *E* as shown in Figure 5.24 and Table 5.13, obtained from the comparison of the cutting force between the experimental result and FEM result is 5%.

Table 5.13: The cutting experimental conditions and results.

Cutting speed (m/min)	250
Feed (mm)	0.2
Cutting force (N)	1224.62
Normal to cutting force(N)	450
Thick of the chip (mm)	0.4
Error (%) (Compared with FEM)	5

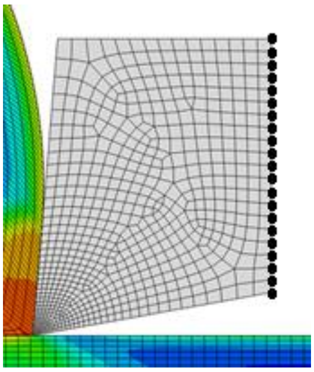

Figure 5.23: The nodes used for obtaining the cutting forces.

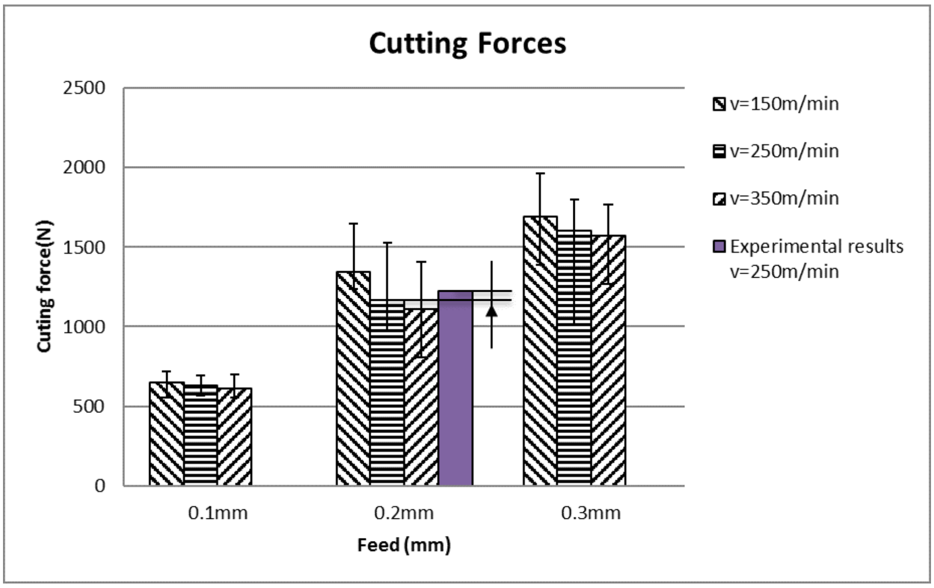

Figure 5.24: Cutting forces of the cutting simulations.

5.5.4 Chip Thickness

Figure 5.25 shows an example of the measurement of the chip thickness from the cutting model with a feed rate of 0.2 mm and a cutting velocity of 250 m/min. Where t_u is the uncut chip thickness equalling the cutting depth, and t_c is the chip thickness perpendicular to the rake face of the tool. All of the chip thicknesses of the cutting models are shown in Table 5.14 and Figure 5.26. The chip thickness decreases as the cutting speed increases, and the chip thickness increases as the feed increases, which two phenomena agree with the reality. Hence, the calibrated material properties are valid.

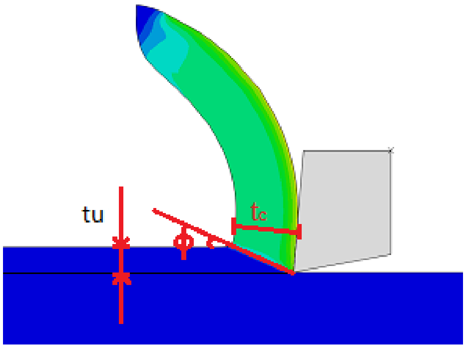

Figure 5.25: Measurement of the chip thickness of the cutting model with feed of 0.2mm, velocity of 250m/min.

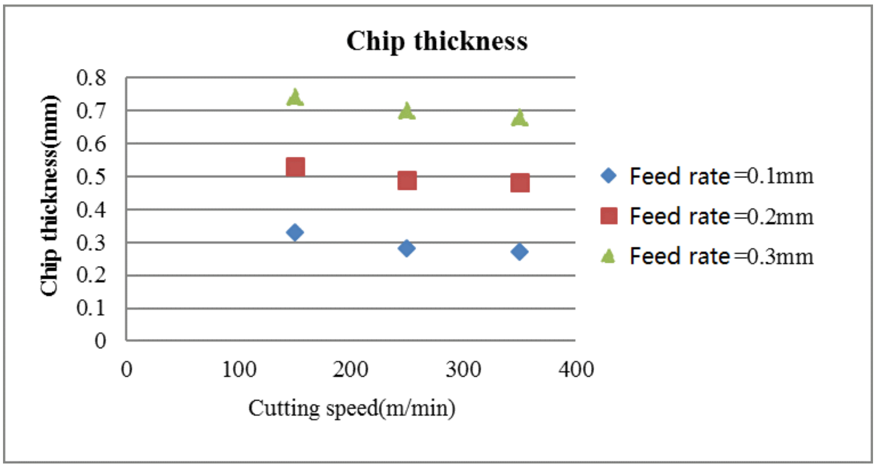

Figure 5.26: Chip thickness with three feeds and cutting speeds from the tension models.

Table 5.14: Chip thickness of all cutting simulations.

Cutting speed (m/min)	Feed rate (mm)	Chip thickness measured from FEM, t_{c_m} (mm)	Shear plane angle measured from FEM, ϕ (deg)	Theoretical chip thickness, t_{c_t} (mm)	Difference, *e* (%)
150	0.1	0.33	18	0.32	4.68
	0.2	0.53	20.8	0.54	-2.18
	0.3	0.74	23.7	0.71	4.70
250	0.1	0.28	20.8	0.27	3.36
	0.2	0.49	23.5	0.48	3.04
	0.3	0.70	24.5	0.68	2.68
350	0.1	0.27	21.8	0.26	4.77
	0.2	0.48	23.4	0.48	0.48
	0.3	0.68	24.5	0.68	-0.26

To further prove that the obtained chip thickness of the cutting model is dependent on the calibrated material properties, the measured chip thickness t_{c_m} is compared with the theoretical chip thickness t_{c_t}, which is computed depending on Merchant's [1945a; 1945b] model using the equations below.

$$\mathrm{r} = \frac{t_o}{t_c} \tag{5.17}$$

$$\tan\phi = \frac{r \times cos\alpha}{1 - r \times sin\alpha} \tag{5.18}$$

$$t_c = t_o \times \left(sin\alpha + \frac{cos\alpha}{tan\phi}\right) \tag{5.19}$$

where r is the chip thickness ratio, t_o is the thickness of the chip prior to chip formation, t_c is the chip thickness after separation, α is the rake angle of the tool, ϕ is the shear plane angle. To obtain the theoretical chip thickness t_{c_t} by using Equation (5.19), ϕ is needed and measured from the equivalent strain contour as shown in Figure 5.18. The results of ϕ, t_{c_t} and the differences (%), which equals $\frac{t_{c\_m} - t_{c\_t}}{t_{c\_t}} \times 100\%$, are in Table 5.14. The differences are in ±5%, which means the chip thickness of the cutting models depending on the calibrated material properties agree well with the analytical model.

5.5.5 Strain to Fracture of the Layer

Figure 5.27 shows the effects of the cutting conditions on the fracture strain induced in the conditional link of the cutting models. All the fracture strain magnitude was obtained at 0.0012 s. As shown in Figure 5.27, the fracture strain of the element in the layer increased with the higher cutting speed. While the fracture strain of the element in the layer also increases with the larger feed rate. This phenomenon was because at higher cutting speeds together with larger feed rates provide more heat energy that was evolved during the chip separation.

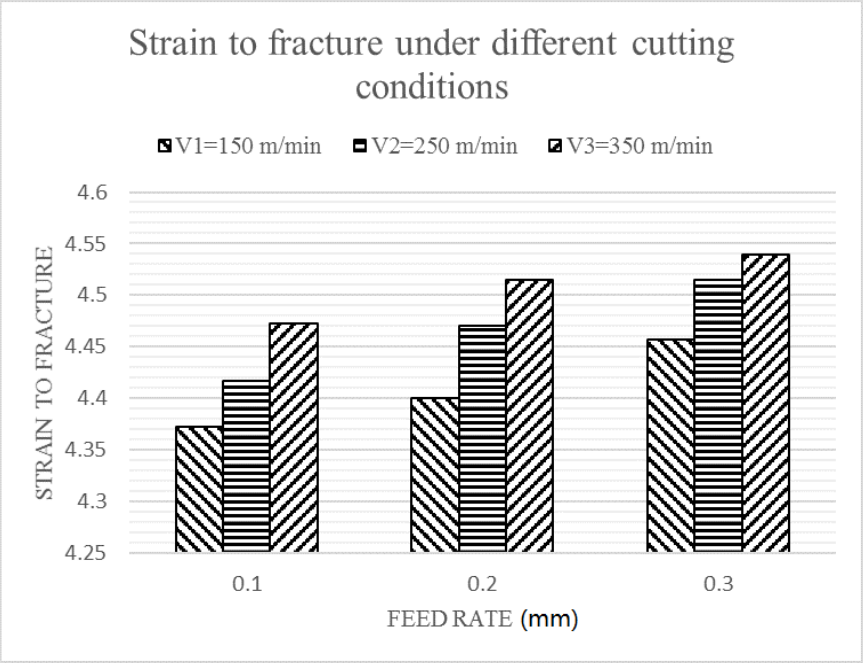

Figure 5.27: The strains to fracture of the layer at time 0.0012s under different cutting conditions.

Figure 5.28 shows the stress triaxiality of the condition link elements in the layers of the cutting simulations at 0.0012 s. The stress triaxiality of the element in the layer is hard to obtain directly from the cutting models, as the element was deleted when it failed as the pressure and von Mises stress of the element are both zero. Hence, the stress triaxiality of the element in the layer assumed equals the sum of the stress triaxialities of the top element and bottom element as shown in Figure 5.29. As shown in Figure 5.28, the stress triaxiality of the element in the layer decreases with higher cutting speed, and it also decreases with the larger feed rate. In other words, the trends of the stress triaxiality of the element in the layer with the cutting speeds and feed rates are reversed to the trends of its strains to fracture. With references to both Figures 5.27 and 5.28, with a higher stress triaxiality ratio, the strain to fracture decreases. This trend was also observed by Johnson and Cook [1985], as detailed in Figure 2.17.

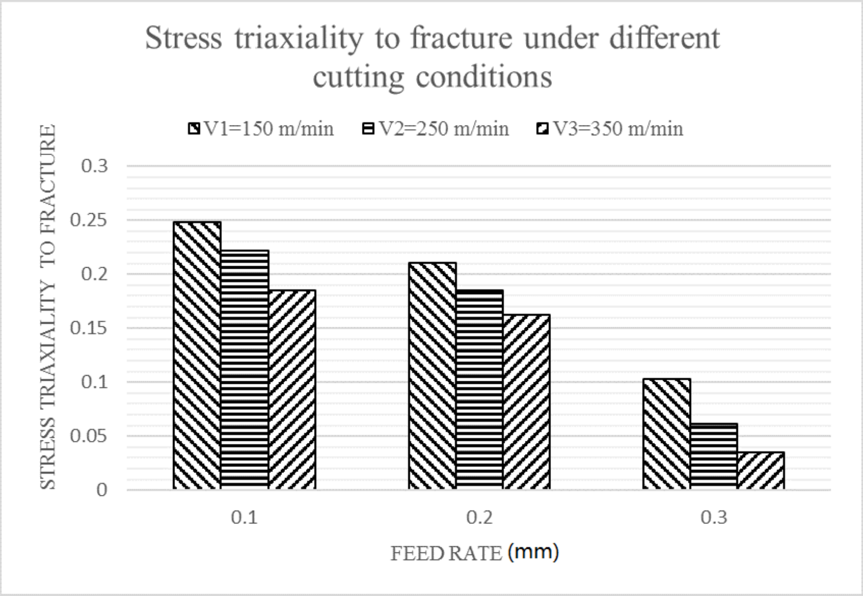

Figure 5.28: The stress triaxiality of the element in the layer of the cutting simulations under different cutting conditions at time 0.0012s.

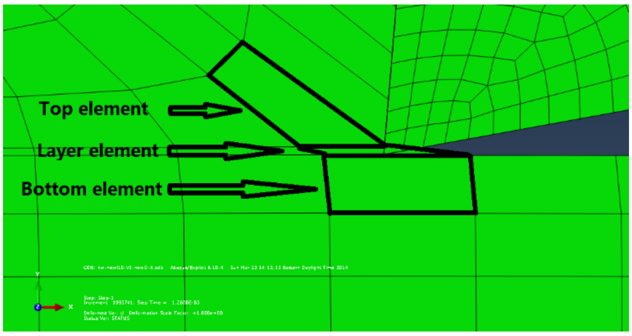

Figure 5.29: The top and bottom elements used for the calculation of the stress triaxiality of the element in the layer.

Figure 5.30 shows the temperatures of the elements of the layers in the cutting simulations under different cutting conditions at the same time 0.0012s. As shown in Figure 5.30, the temperature of the element in the layer increases with the increasing of the cutting speed and feed rate. Comparing with Figure 5.27, the trends of the temperatures of the elements in the layers have similar trends of the strains to fracture of the elements in the layers. Comparing with Figure 5.27, at a higher temperature of the elements in the layer, the strain to fracture also increases. This finding was due to higher ductility with higher temperature. This trend was also observed by Borvik et al. [2001] as shown in Figure 2.13 (b).

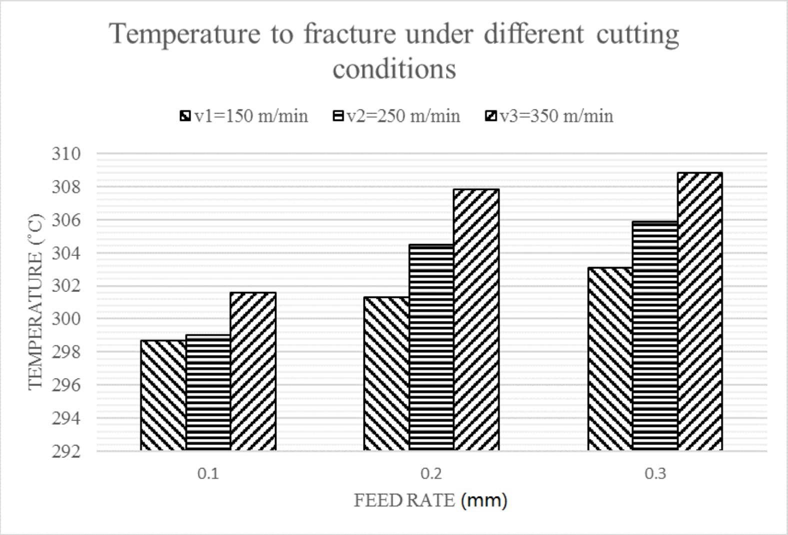

Figure 5.30: The temperatures of the elements in the layers of the cutting simulations under different cutting conditions.

6. Conclusion

In this thesis, the Johnson-Cook constitutive and fracture parameters were calibrated for AISI 1045 steel based on a set of quasi-static tensile tests with smooth and notched round bars at room temperature and elevated temperatures respectively. The results were validated by the FEM simulations of tensile tests and the orthogonal cutting process, and both have good agreement with the corresponding experimental results.

Stress triaxiality is the principal influence factor on the ductile fracture. Depending on three different fracture mechanisms, including the shear decohesion, the void growth and the combination of the shear decohesion and void growth, the range of stress triaxiality was divided into three branches respectively. However, the Johnson-Cook fracture model is a monotonic function that is only valid in a narrow range of stress triaxiality with void growth fracture mechanisms. Hence, it may decrease the accuracy of the Johnson-Cook fracture parameters if more other tests are considered, such as torsion tests and compression tests. The conclusion is that the tensile tests with smooth and notched round bars are good enough to calibrate the Johnson-Cook fracture parameters.

In the metal cutting process, two fracture mechanisms occur in the fracture elements: shear decohesion and void growth. As the Johnson-Cook fracture model is only used to predict the onset of fracture, the fracture evolution with these two fracture mechanisms is necessarily used in the FEM simulations of cutting.

Compared to the literature calibrations of the Johnson-Cook fracture parameters for AISI 1045 steel, the calibration in this thesis does not require high strain rate experimental results acquired from Split-Hopkinson bar tests.

7. Future Works

Future works extended from this thesis include the following:

1. To verify the obtained Johnson-Cook fracture parameters for AISI 1045 steel in FE simulations of metal cutting with other cutting conditions, such as the cutting with a negative or zero rake angle or with high cutting velocity.

2. To explore this calibration method for Johnson-Cook fracture parameters for other materials. Furthermore, to implement the fracture parameters of different components based on this simple calibration method into the heterogeneous FE cutting model.

BIBLIOGRAPHY

[ABAQUS, 2003] Hibbit, H.D., Karlsson, B.I., & Sorrensen (2003). ABAQUS Online Documentation: Version 6.4-1, *ABAQUS Inc*.

[Anderson, 2005] Anderson, T. L., & Anderson, T. (2005). *Fracture mechanics: fundamentals and applications*: CRC press. ISBN: 978-1-4200-5821-5

[Argon, 1975] Argon, A., Im, J., & Safoglu, R. (1975). Cavity formation from inclusions in ductile fracture. *Metallurgical Transactions A, 6*(4), 825-837.

[Arias, 2008] Arias, A., Rodríguez-Martínez, J. A., & Rusinek, A. (2008). Numerical simulations of impact behaviour of thin steel plates subjected to cylindrical, conical and hemispherical non-deformable projectiles. *Engineering Fracture Mechanics, 75*(6), 1635-1656.

[Autenrieth, 2009] Autenrieth, H., Schulze, V., Herzig, N., & Meyer, L. W. (2009). Ductile failure model for the description of AISI 1045 behavior under different loading conditions. *Mechanics of Time-Dependent Materials, 13*(3), 215-231.

[Børvik, 2005] Børvik, T., Hopperstad, O., Dey, S., Pizzinato, E., Langseth, M., & Albertini, C. (2005). Strength and ductility of Weldox 460 E steel at high strain rates, elevated temperatures and various stress triaxialities. *Engineering Fracture Mechanics, 72*(7), 1071-1087.

[Børvik, 2001] Børvik, T., Hopperstad, O. S., Berstad, T., & Langseth, M. (2001). A computational model of viscoplasticity and ductile damage for impact and penetration. *European Journal of Mechanics - A/Solids, 20*(5), 685-712. doi:http://dx.doi.org/10.1016/S0997-7538(01)01157-3

[Bai, 2009] Bai, Y., Teng, X., & Wierzbicki, T. (2009). On the application of stress triaxiality formula for plane strain fracture testing. *Journal of Engineering Materials and Technology, 131*(2), 021002.

[Bai, 2008] Bai, Y., & Wierzbicki, T. (2008). A new model of metal plasticity and fracture with pressure and Lode dependence. *International Journal of Plasticity, 24*(6), 1071-1096.

[Bao, 2003] Bao, Y. (2003). *Prediction of ductile track formation in uncracked bodies.* Ph.D. thesis, Massachusetts Institute of Technology.

[Bao, 2004a] Bao, Y., & Wierzbicki, T. (2004a). A comparative study on various ductile crack formation criteria. *Journal of Engineering Materials and Technology, 126*(3), 314-324.

[Bao, 2004b] Bao, Y., & Wierzbicki, T. (2004b). On fracture locus in the equivalent strain and stress triaxiality space. *International Journal of Mechanical Sciences, 46*(1), 81-98.

[Bao, 2005] Bao, Y., & Wierzbicki, T. (2005). On the cut-off value of negative triaxiality for fracture. *Engineering Fracture Mechanics, 72*(7), 1049-1069.

[Bil, 2004] Bil, H., Kılıç, S. E., & Tekkaya, A. E. (2004). A comparison of orthogonal cutting data from experiments with three different finite element models. *International Journal of Machine Tools and Manufacture, 44*(9), 933-944.

[Borkovec, 2008] Borkovec, J. (2008). Computer simulation of material separation process. Ph.D. thesis, Brno: Brno University of Technology, Institute of Solid Mechanics, Mechatronics and Biomechanics.

[Bridgman, 1952] Bridgman, P. W. (1952). *Studies in large plastic flow and fracture* (Vol. 177): McGraw-Hill New York.

[Callister, 2007] Callister, W. D., & Rethwisch, D. G. (2007). *Materials science and engineering: an introduction* (Vol. 7): Wiley New York.

[Ceretti, 1996] Ceretti, E., Fallböhmer, P., Wu, W., & Altan, T. (1996). Application of 2D FEM to chip formation in orthogonal cutting. *Journal of Materials Processing Technology, 59*(1), 169-180.

[Cockcroft, 1968] Cockcroft, M., & Latham, D. (1968). Ductility and the workability of metals. *Journal of Institute of Metals, 96*(1), 33-39.

[Cottrell, 2012] Cottrell, A. (2012). *Theoretical aspects of fracture.* Paper presented at the ICF0, Swampscott-MA (USA) 1959.

[Davidson, 1968] Davidson, T., & Ansell, G. (1968). The structure sensitivity of the effects of pressure upon the ductility of Fe-C materials. *ASM TRANS QUART, 61*(2), 242-254.

[Dhar, 2007] Dhar, N.R., Ahmed, M.T. Islam, S. (2007). An experimental investigation on effect of minimum quantity lubrication in machining AISI 1040 steel. *International Journal of Machine Tools & Manufacture,* (47),748-753.

[Duan, 2009] Duan, C., Dou, T., Cai, Y., & Li, Y. (2009). Finite element simulation and experiment of chip formation process during high speed machining of AISI 1045 hardened steel. *International Journal of Recent Trends in Engineering, 1*(5), 46-50.

[Dzugan, 2013] Dzugan, J., Prantl, A., Spaniel, M., Konopik, P., Ruzicka, J., & Kuzelka, J. (2013). Identification of ductile damage parameters for pressure vessel steel. *SMiRT—22, 18*, 30.

[Hancock, 1976] Hancock, J., & Mackenzie, A. (1976). On the mechanisms of ductile failure in high-strength steels subjected to multi-axial stress-states. *Journal of the Mechanics and Physics of Solids, 24*(2), 147-160.

[Henry, 1997] Henry, B., & Luxmoore, A. (1997). The stress triaxiality constraint and the Q-value as a ductile fracture parameter. *Engineering Fracture Mechanics, 57*(4), 375-390.

[Hortig, 2007] Hortig, C., & Svendsen, B. (2007). Simulation of chip formation during high-speed cutting. *Journal of Materials Processing Technology, 186*(1), 66-76.

[Hosseinkhani, 2013] Hosseinkhani, K., & Ng, E. (2013). Analysis of the Cutting Mechanics Under the Influence of Worn Tool Geometry. *Procedia CIRP, 8*, 117-122. doi:http://dx.doi.org/10.1016/j.procir.2013.06.075

[Huang, 1996] Huang, J., & Black, J. (1996). An evaluation of chip separation criteria for the FEM simulation of machining. *Journal of Manufacturing Science and Engineering, 118*(4), 545-554.

[Iwata, 1984] Iwata, K., Osakada, K., & Terasaka, Y. (1984). Process modelling of orthogonal cutting by the rigid-plastic finite element method. *Journal of Engineering Materials and Technology, 106*(2), 132-138.

[Jaspers, 2002] Jaspers, S., & Dautzenberg, J. (2002). Material behaviour in conditions similar to metal cutting: flow stress in the primary shear zone. *Journal of Materials Processing Technology, 122*(2), 322-330.

[Johnson, 1989] Johnson, G., & Holmquist, T. (1989). Test data and computational strength and fracture model constants for 23 materials subjected to large strains, high strain rates, and high temperatures. *Los Alamos National Laboratory, Los Alamos, NM, Report No. LA-11463-MS.*

[Johnson, 1983] Johnson, G. R., & Cook, W. H. (1983). *A constitutive model and data for metals subjected to large strains, high strain rates and high temperatures.* Paper presented at the Proceedings of the 7th International Symposium on Ballistics,541-547.

[Johnson, 1985] Johnson, G. R., & Cook, W. H. (1985). Fracture characteristics of three metals subjected to various strains, strain rates, temperatures and pressures. *Engineering Fracture Mechanics, 21*(1), 31-48.

[Kalhori, 2001] Kalhori, V. (2001). Modelling and simulation of mechanical cutting. Ph.D. these*, Lulea University of Technology*.

[Kao, 1990] Kao, A., Kuhn, H., Richmond, O., & Spitzig, W. (1990). Tensile fracture and fractographic analysis of 1045 spheroidized steel under hydrostatic pressure. *Journal of Materials Research, 5*(01), 83-91.

[Klamecki, 1973] Klamecki, B. E. (1973). *Incipient Chip Formation in Metal Cutting--a Three-dimension Finite Element Analysis.* Ph.D. thesis, University of Illinois at Urbana-Champaign.

[Komvopoulos, 1991] Komvopoulos, K., & Erpenbeck, S. (1991). Finite element modelling of orthogonal metal cutting. *Journal of Manufacturing Science and Engineering, 113*(3), 253-267.

[Rosa, 2001] La Rosa, G., Mirone, G., & Risitano, A. (2001). Effect of stress triaxiality corrected plastic flow on ductile damage evolution in the framework of continuum damage mechanics. *Engineering Fracture Mechanics, 68*(4), 417-434.

[Roy, 1981] Le Roy, G., Embury, J., Edwards, G., & Ashby, M. (1981). A model of ductile fracture based on the nucleation and growth of voids. *Acta Metallurgica, 29*(8), 1509-1522.

[Lemaitre, 1992] Lemaitre, J. (1992). A short course in damage mechanics: Springer-Verlag, New York. ISBN: 978-3-642-18255-6.

[Li, 2002] Li, K., Gao, X.-L., & Sutherland, J. (2002). Finite element simulation of the orthogonal metal cutting process for qualitative understanding of the effects of crater wear on the chip formation process. *Journal of Materials Processing Technology, 127*(3), 309-324.

[Lin, 1992] Lin, Z., & Lin, S. (1992). A coupled finite element model of thermo-elastic-plastic large deformation for orthogonal cutting. *Journal of Engineering Materials and Technology, 114*(2), 218-226.

[Liu, 2000] Liu, C., & Guo, Y. (2000). Finite element analysis of the effect of sequential cuts and tool–chip friction on residual stresses in a machined layer. *International Journal of Mechanical Sciences, 42*(6), 1069-1086.

[Liu, 1968] Liu, C., & Gurland, J. (1968). The fracture behavior of spheroidized carbon steels. *Transactions of American Society for Metals, 61*, 156-167.

[Liu, 2014] Liu, J., Bai, Y., & Xu, C. (2014). Evaluation of ductile fracture models in finite element simulation of metal cutting processes. *Journal of Manufacturing Science and Engineering, 136*(1), 011010.

[Majzoobi, 2011] Majzoobi, G., & Dehgolan, F. R. (2011). Determination of the constants of damage models. *Procedia Engineering, 10*, 764-773.

[Mamalis, 2001] Mamalis, A., Horvath, M., Branis, A., & Manolakos, D. (2001). Finite element simulation of chip formation in orthogonal metal cutting. *Journal of Materials Processing Technology, 110*(1), 19-27.

[McClintock, 1968] McClintock, F. A. (1968). A criterion for ductile fracture by the growth of holes. *Journal of Applied Mechanics, 35*(2), 363-371.

[Merchant, 1945a] Merchant, M. E. (1945a). Mechanics of the Metal Cutting Process. I. Orthogonal Cutting and a Type 2 Chip. *Journal of Applied Physics, 16*(5), 267-275. doi:doi:http://dx.doi.org/10.1063/1.1707586

[Merchant, 1945b] Merchant, M. E. (1945b). Mechanics of the Metal Cutting Process. II. Plasticity Conditions in Orthogonal Cutting. *Journal of Applied Physics, 16*(6), 318-324. doi:doi:http://dx.doi.org/10.1063/1.1707596

[Ralls, 1976] Ralls, K., Courtney, T. H., & Wulff, J. (1976). *Introduction to materials science and engineering*: John Wiley & Sons, Inc. ISBN: 978-0-471-70665-6

[Reddy, 2011] Reddy M.R., Ravikumar, P., Rao, G.K.M (2011). Effect of feed rate on the generation of surface roughness in turning. *International Journal of Engineering Science and Technology*, 3 (11), 8099-8105

[Rice, 1969] Rice, J. R., & Tracey, D. M. (1969). On the ductile enlargement of voids in triaxial stress fields. *Journal of the Mechanics and Physics of Solids, 17*(3), 201-217.

[Shet, 2000] Shet, C., & Deng, X. (2000). Finite element analysis of the orthogonal metal cutting process. *Journal of Materials Processing Technology, 105*(1), 95-109.

[Soo, 2007] Soo, S., & Aspinwall, D. (2007). Developments in modelling of metal cutting processes. *Proceedings of the Institution of Mechanical Engineers, Part L: Journal of Materials Design and Applications, 221*(4), 197-211.

[Strenkowski, 1985] Strenkowski, J. S., & Carroll, J. (1985). A finite element model of orthogonal metal cutting. *Journal of Manufacturing Science and Engineering, 107*(4), 349-354.

[Sun, 1991] Sun, J., Deng, Z.-J., & Tu, M.-J. (1991). Effect of stress triaxiality levels in crack tip regions on the characteristics of void growth and fracture criteria. *Engineering Fracture Mechanics, 39*(6), 1051-1060.

[Teng, 2006] Teng, X., & Wierzbicki, T. (2006). Evaluation of six fracture models in high velocity perforation. *Engineering Fracture Mechanics, 73*(12), 1653-1678.

[Thomason, 1998] Thomason, P. (1998). A view of ductile-fracture modelling. *Fatigue & Fracture of Engineering Materials & Structures, 21*(9), 1105-1122.

[Usta, 1999] Usta, M. (1999). *Finite element analysis of orthogonal metal cutting operations*. Ph.D. Thesis, Mechanical Engineering Department of Middle East Technical University, Ankara, Turkey.

[Usui, 1982] Usui, E., & Shirakashi, T. (1982). Mechanics of machining—from descriptive to predictive theory. *On the Art of Cutting Metals—75 Years Later, 7*, 13-35.

[Vaziri, 2010] Vaziri, M., Salimi, M., & Mashayekhi, M. (2010). A new calibration method for ductile fracture models as chip separation criteria in machining. *Simulation Modelling Practice and Theory, 18*(9), 1286-1296.

[Wierzbicki, 2005] Wierzbicki, T., Bao, Y., Lee, Y.-W., & Bai, Y. (2005). Calibration and evaluation of seven fracture models. *International Journal of Mechanical Sciences, 47*(4–5), 719-743. doi:http://dx.doi.org/10.1016/j.ijmecsci.2005.03.003

[Wierzbicki, 1998] Wierzbicki, T., & Werner, H. (1998). 'Cockroft and Latham Revisited. *Impact & Crashworthiness Laboratory Report*(16).

[Wilkins, 1978] Wilkins, M. L. (1978). Mechanics of penetration and perforation. *International Journal of Engineering Science, 16*(11), 793-807.

[Xie, 1998] Xie, J., Bayoumi, A., & Zbib, H. (1998). FEA modelling and simulation of shear localized chip formation in metal cutting. *International Journal of Machine Tools and Manufacture, 38*(9), 1067-1087

[Zhang, 1999] Zhang, L. (1999). On the separation criteria in the simulation of orthogonal metal cutting using the finite element method. Journal of Materials Processing Technology, 89, 273-278.

APPENDIX A

The grips of the tensile tests used as the fixture were designed at McMaster University by Dr. Mike Bruhis, as shown in Figure A1. The stainless steel was chosen as the materials of the grips to reduce the wear during the high temperature tests.

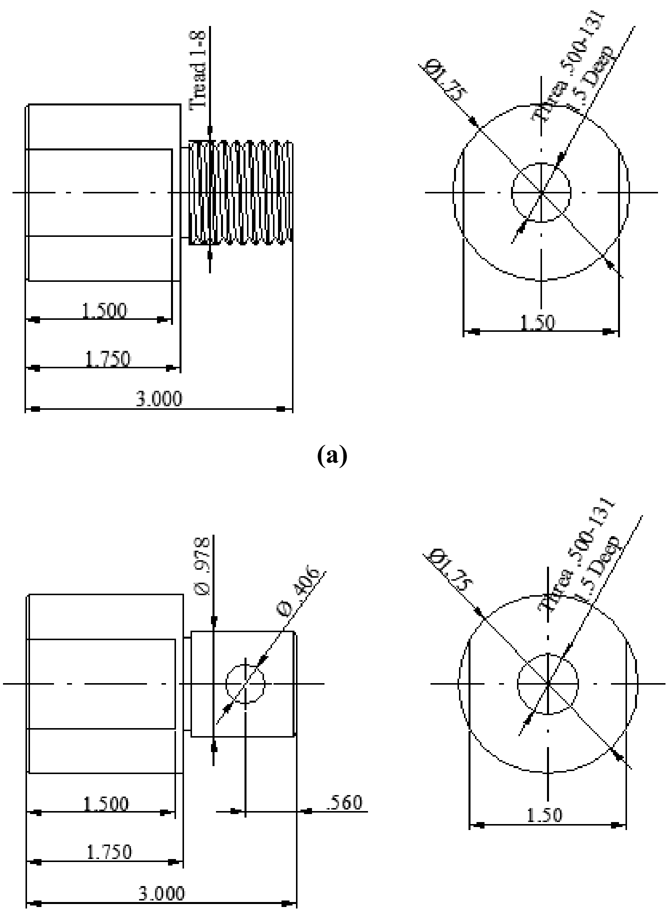

(a)

(b)

Figure A1: (a) Dimensions of the upper grip; (b) Dimensions of the bottom grip.